Proceedings of the 18th ICMRM

17th – 21st of August 2025

at the

University of Würzburg

Germany

Platinum sponsor

BRUKER

Gold sponsors

青檬艾柯 LIMECHO

pure devices

resonint

Silver sponsors

NORAS MRI PRODUCTS

phase VISION

RAPID Biomedical

Bronze sponsor

magritek

Donors

We thank the Wittenstein foundation for their generous support of the Paul Callaghan Young Investigator Competition.

We thank the ct.qmat cluster of excellence for their support of the invited speakers' program.

We thank the Groupement AMPERE for their support of the conference organization.

BRUKER

NMR

Reduced Helium Consumption

Bruker innovations advance research while reducing helium consumption.

Ascend Evo 1.0 GHz reduces helium consumption by 3-fold with a hold-time of 130 days

HelioSmart Recovery collects helium boil-off and has a typical recovery rate of 80-85%

For more information please visit www.bruker.com

Innovation with Integrity

Welcome

Welcome to the 18th International Conference on Magnetic Resonance Microscopy (ICMRM), from August 17th to 21st, 2025. We are delighted to organize the conference in 2025 at the University of Würzburg, Germany. Founded in 1402 the university is the oldest university in Bavaria and number four all over Germany and hence has a long tradition of academic science and education.

The aim of the ICMRM series is to promote the most recent advances in the development of spatially resolved magnetic resonance methods and their applications. It started in 1991 in Heidelberg, Germany and was continued as a biannual meeting (originally called "Heidelberg Conferences") with its last meeting in 2023 held in Singapore.

In 1995 the Division of Spatially Resolved Magnetic Resonance (SRMR) was founded as a sub-division of Groupement AMPERE during the 3rd ICMRM held at Würzburg. Under the auspices of this community all further ICMRM conference have been organized. Almost to the day 30 years after the conference was last organized at the University of Würzburg in 1995, the 18th ICMRM will therefore also celebrate the anniversary of SRMR at the very place of its formation.

It is a pity students and scientists from some areas cannot join us for this year's ICMRM due to the current geopolitical situation manifesting in wars or protectionist and anti-science stances of governments.

Nevertheless, we are very happy to have more than 130 participants from a total of 19 different countries. The conference will see almost 70 talks and over 30 posters on all fields of MR imaging and for the first time a full dedicated session on the emerging field of magnetic particle imaging. Out of 13 submissions to the Paul Callaghan Young Investigator Award five are invited to present in the finals for the award. Lynn Gladden from the University of Cambridge receives this year's Erwin Hahn Lecturer Award for her lifetime achievement on MR and her lecture will open the finals. The conference starts with a series of educational lectures and the first day is marked by a special plenary lecture celebrating the anniversary of SRMR.

We wish to all of you an exciting, inspiring, and entertaining ICMRM 2025!

Volker Behr and Peter Jakob

Chairs of ICMRM 2025

Committees

Chairs of ICMRM 2025 at the University of Würzburg:

Volker Behr
Peter Jakob

Executive Committee of SRMR:

Chair:	Luisa Ciobanu, France
Vice-Chair:	Ben Newling, Canada
Treasurer:	Andy Sederman, United Kingdom
Secretary General:	Volker Behr, Germany
Vice Secretary General:	Sarah Codd, United States
Past chair:	Melanie Britton, United Kingdom
Next conference chairs:	Daniel Topgaard, Sweden
	Diana Bernin, Sweden
Advisors:	Bernhard Blümich, Germany
	Eiichi Fukushima, United States
	Igor Koptyug, Russia
	Henk van As, Netherlands
	Lizhi Xiao, China

Division Committee of SRMR:

Bruce Balcom (CA), Stephen Beyea (CA), Louis Bouchard (US), Martin Bruschewski (DE), Hilary Fabich (US), Einar Fridjonsson (AU), Petrik Galvosas (NZ), Gillian Goward (CA), Gisela Guthausen (DE), Meghan Halse (GB), Shaoying Huang (SG), Michael Johns (AU), Miki Komlosh (US), Katsumi Kose (JP), Huabing Liu (CN), Thomas Oerther (DE), Andreas Pohlmeier (DE), Dimitrios Sakellariou (BE), Joseph Seymour (US), Bernhard Siow (GB), Siegfried Stapf (DE), Ray Tang (US), Camilla Terenzi (NL), Velencia Witherspoon (US), Dan Xiao (CA), Zheng Xu (CN), Wenwei Yu (JP)

Scientific Committee:

The Scientific Committee includes all members of the Executive Committee and the Division Committee.

Programme at a glance

Sunday

10:30	Arrivals and registration
13:00	Educational Session
16:45	Plenary Session: 30 years of SRMR
19:00	Opening Reception

Programme at a glance

Monday

8:45	Opening
9:00	Flow & Diffusion
11:15	Mobile & Low Field
13:00	Lunch
14:00	Biomedical Imaging
16:00	Posters (odd numbers)

Tuesday

8:45	Hardware
11:00	Porous Media & Low Field
12:45	Lunch Executive Meeting
14:00	Magentic Particle Imaging & Spectroscopy
16:00	Posters (even numbers)

Programme at a glance

Wednesday

8:45	Erwin Hahn Lecture 2025 & Young Investigator Finals
10:50	Young Investigator Finals & Erwin Hahn Lecture 2023
12:50	Lunch Division Meeting
13:50	Free Afternoon
17:30	Conference Banquet

Thursday

8:45	Plants
11:00	Engineering & Solid-State
12:30	Lunch
13:30	General Assembly Meeting
14:15	Microscopy & Cellular
15:30	Closing

Sunday, Aug. 17th

TIME	EVENT
10:30	**Arrivals and registration**
	Educational Session: Building scientific apparatus **Chair:** Bernhard Blümich, RWTH Aachen University, Germany
13:00	Optimizing signal-to-noise for portable low field MRI systems ***Andrew Webb***, *Leiden University Medical Center, Netherlands*
14:00	**Break**
14:15	How to build a new imaging modality … and make it work ***Patrick Vogel***, *University of Würzburg, Germany*
15:15	**Break**
15:30	Portable MRI scanner: Magnet designs, gradient coils, and open-source resources ***Shaoying Huang***, *Singapore University of Technology and Design, Singapore*
16:30	**Break**
	Plenary Session: 30 years of SRMR **Chair:** Igor Koptyug, International Tomography Center, Russia
16:45	The 1990s ***Axel Haase***, *Technical University of Munich, Germany*
17:15	The 2000s ***Bernhard Blümich***, *RWTH Aachen University, Germany*
17:45	The 2010s ***Sarah Codd***, *Montana State University, United States*
18:15	The 2020s ***Luisa Ciobanu***, *NeuroSpin, CEA-Saclay, France*
18:45	**Break**
19:00	**Opening Reception**

Monday, Aug. 18th

TIME	EVENT
08:45	**Opening**
	Scientific Session 1: Flow & Diffusion **Chair:** Joseph Seymour, Montana State University, United States
09:00	Careful Comparison of MRI and Computer Simulations of Bubbly, Particle-Laden Flows *Christopher Boyce, Columbia University, United States*
09:30	MRI measurement of fluid mechanical properties in granular flow *Kristine John, University of Rostock, Germany*
09:45	Spectrally Resolved Turbulent Flow in Porous Structures Using Modulated Gradient Diffusion NMR *Daniel Clarke, Lund University, Sweden*
10:00	Rapid Flow Characterization Measurements Using a Modified CPMG Measurement with Incremented Echo Times, Phase Cycling and Filtering *Sebastian Richard, University of New Brunswick, Canada*
10:15	Ex-Vivo Diffusion Tensor Characterization of Peri-Fibrotic Myocardial Regions In Myocardial Infarction *Ali Nahardani, University Hospital Bonn, Germany*
10:30	Microstructural Assessment of Oral Squamous Cell Carcinoma Using Time-Dependent Diffusion MRI *Jamila Guichelaar, University Medical Center Utrecht, Netherlands*
10:45	**Break**
	Scientific Session 2: Mobile & Low Field **Chair:** Andrew Webb, Leiden University Medical Center, Netherlands
11:15	Halbach 2.0 – Creating homogenous fields with finite size magnets *Peter Blümler, University Mainz, Germany*
11:30	A New Approach for Shimming Halbach Ring Magnets: Magnetically Soft Materials *Andrew McDowell, NuevoMR, United States*
11:45	Adaptive magnetic field mapping to accelerate the B_0 shimming process in a low- field MRI using Gaussian process regression *Marcel Ochsendorf, Fraunhofer MEVIS, Germany*

12:00	A Self-Supervised Inversion Framework for Low-Field 2D NMR Relaxation Spectra with Embedded Fluid-Specific Physical Priors *Gang Luo, China University of Petroleum – Beijing, China*
12:15	A Frequency Selective Surface (FSS) Shield for Portable Low-Field MRI *Junqi Yang, Chiba University, Japan*
12:30	Low Field Magnetic Resonance in Harsh Environments *Michael Johns, University of Western Australia, Australia*
12:45	MagTetris+: A rapid simulator for magnetic field and force calculation for ferromagnetic materials and permanent magnets *Jing Han Heng, Singapore University of Technology and Design, Singapore*
13:00	**Lunch**
	Scientific Session 3: Biomedical Imaging **Chair:** Peter Basser, NIH, United States
14:00	Magnetic Resonance Fingerprinting: Promise and Challenges *Nicole Seiberlich, University of Michigan, United States*
14:30	Magnetic resonance fingerprinting enables high-resolution joint morphometry and relaxometry of the inner ear *Jannik Stebani, Fraunhofer Institute for Integrated Circuits, Germany*
14:45	Deep Learning-Based Algorithm for Reconstructing Diffusion Tensor Distribution Imaging Parameters *Jiayin Zhou, Beijing University of Posts and Telecommunications, China*
15:00	From the central and peripheral nervous system to cardiac conduction: biomagnetic field detection using rotary excitation *Petra Albertova, University Hospital Würzburg, Germany*
15:15	Post-Traumatic Osteoarthritis Following a Sub-Critical Impact by µMRI *Yang Xia, Oakland University, United States*
15:30	Noninvasive Measurement of Fascia Thickness in Porcine Models for Investigating Myofascial Pain Using Single- Sided NMR *Jenna Necaise, Tulane University, United States*
15:45	**Break**
16:00	**Poster Session 1** (odd numbers)

Tuesday, Aug. 19th

TIME	EVENT
	Scientific Session 4: Hardware **Chair:** Shaoying Huang, Singapore University of Technology and Design, Singapore
08:45	Redefining NMR: Portable, Dead-Time–Free, and Chip-Powered *Jens Anders, University of Stuttgart, Germany*
09:15	MRI using straight wires as spatial encoding coils *Igor Serša, Jožef Stefan Institute, Slovenia*
09:30	Compact NMR tool for underground soil contaminants monitoring *Sihui Luo, China University of Petroleum – Beijing, China*
09:45	Contact-free MRI and MRS on self-standing droplets *Diana Bernin, Chalmers University of Technology, Sweden*
10:00	Helium-3 magnetometers for high fields *Peter Blümler, University Mainz, Germany*
10:15	Nano- and microscale NMR microscopy using NV-centers in diamond *Dominik Bucher, Technical University of Munich, Germany*
10:30	**Break**
	Scientific Session 5: Porous Media & Low Field **Chair:** Camilla Terenzi, Wageningen University & Research, Netherlands
11:00	Topology Optimization Method for Nuclear Magnetic Resonance Logging tool Magnetic and Soft magnetic Design *Zhen Qiao, China University of Petroleum – Beijing, China*
11:15	Fluid quantitative evaluation method of two-dimensional NMR logging *Li Chenglin, China University of Geosciences Beijing, China*
11:30	Velocity Measurement in Porous Media Using Steady-State Free Precession *Mohammad Sadegh Zamiri, University of New Brunswick, Canada*
11:45	Magnetic Resonance Studies of Adsorption Phenomena *Michael Johns, University of Western Australia, Australia*

12:00	Phase separation of miscible fluids in mesoporous media monitored by q space microscopy and relaxometry *Siegfried Stapf, TU Ilmenau, Germany*
12:15	pH controlled modification of metal oxide surfaces in mine tailings measured by low field ^{1}H NMR relaxometry *Einar Fridjonsson, University of Western Australia, Australia*
12:30	Magnetic Resonance and Magnetic Resonance Imaging with a Variable Field Cryogen Free Superconducting Magnet *Bruce Balcom, University of New Brunswick, Canada*
12:45	**Lunch / Executive Meeting**
	Scientific Session 6: Magnetic Particle Imaging & Spectrocopy **Chair:** Volkmar Schulz, RWTH Aachen University, Germany
14:00	Relaxation-Based Color Magnetic Particle Imaging for Functional Imaging *Emine Saritas, Bilkent University, Türkiye*
14:30	Spatial regularization in 2D multi-color magnetic particle imaging *Franziska Schrank, RWTH Aachen University, Germany*
14:45	Spatial Receive Sensitivity Assessment using MPI Transfer Function Measurements *Florian Thieben, Hamburg University of Technology, Germany*
15:00	Next-Generation Single-Sided MPI Scanner – Towards Clinical Applications *Alexey Tonyushkin, Oakland University, United States*
15:15	3D temperature mapping with MPI and MRI *Nuno Joao Silva, Universidade de Aveiro, Portugal*
15:30	Mulitmodal imaging of flow dynamics in a realistic aneurysm phantom *Teresa Reichl, University of Würzburg, Germany*
15:45	**Break**
16:00	**Poster Session 2** (even numbers)

Wednesday, Aug. 20th

TIME	EVENT
	Awards Session 1: Erwin Hahn Lecture 2025 & Paul Callaghan Young Investigator Award Finals **Chair:** Luisa Ciobanu, NeuroSpin, CEA-Saclay, France
08:45	Spatially-Resolved Magnetic Resonance: More Than Just a Camera ***Lynn Gladden***, *University of Cambridge, United Kingdom* *Erwin Hahn Lecturer 2025*
09:30	Flexible Radio Frequency Pulse Optimization using Deep Learning Methods ***Tristhal Parasram***, *University of Windsor, Canada* *PCYIA Finalist 2025*
09:55	Key MRV Sequence Parameters for Turbulence Quantification in Fluid Flow: Resolution and Higher-Order Gradient Moments ***Swantje Romig***, *University of Rostock, Germany* *PCYIA Finalist 2025*
10:20	**Break**
	Awards Session 2: Paul Callaghan Young Investigator Award Finals & Erwin Hahn Lecture 2023 **Chair:** Ben Newling, University of New Brunswick, Canada
10:50	Studying restricted diffusion with more accessible gradient amplitudes ***Alfredo Ordinola***, *Linköping University, Sweden* *PCYIA Finalist 2025*
11:15	Magnetic Resonance Imaging and numerical modelling of vibrated bubbling gas-solid fluidized beds ***Melis Özdemir***, *Hamburg University of Technology, Germany* *PCYIA Finalist 2025*
11:40	Functional Brain Imaging and Targeted Lesion Studies Using Manganese-Enhanced MRI and Focused Ultrasound in Non-Conventional Model Species ***Pierre Estienne***, *NeuroSpin, CEA-Saclay, France* *PCYIA Finalist 2025*
12:05	Fascinated by NMR, MRI and … plants: about 50 years curiosity driven intact plant and plant materials applications with some relevant spin-off ***Henk van As***, *Wageningen University & Research, Netherlands* *Erwin Hahn Lecturer 2023*
12:50	**Lunch / Division Meeting**
13:50	**Free Afternoon**
17:30	Conference Banquet

Thursday, Aug. 21st

TIME	EVENT
	Scientific Session 7: Plants **Chair:** Henk van As, Wageningen University & Research, Netherlands
08:45	MRI in Plant Research: Unlocking the Hidden Life of Seeds *Ljudmilla Borisjuk, IPK Gatersleben, Germany*
09:15	Establishing Ground Rules for Sensor-like Application of NMR Relaxometry for the Study of Water and Dry Matter Dynamics in Living Plants *Antonia Wörtche, Forschungszentrum Jülich, Germany*
09:30	MRI of hydraulic failure in plants by means of a mobile, low field imager: can low spatial resolution be compensated by means of MRI relaxometry? *Carel Windt, Forschungszentrum Jülich, Germany*
09:45	Plants: A new application field for Chemical Exchange Saturation Transfer (CEST) *Simon Mayer, University of Würzburg, Germany*
10:00	MRI mapping of structural anisotropy in plant-based protein extrudates *Sam Kuijpers, Wageningen University & Research, Netherlands*
10:15	Low field biological J-coupling spectroscopy *Gonzalo Rodriguez, MPI for Multidisciplinary Sciences, Germany*
10:30	**Break**
	Scientific Session 8: Engineering & Solid-State **Chair:** Michael Johns, University of Western Australia, Australia
11:00	Imaging a sample spinning at 30 kHz and more: A new horizon for solid-state MRI *Vincent Sarou-Kanian, CNRS CEMHTI, France*
11:15	Crystal Structure, Particle Size, and Ionic Conductivity of Solid-State Electrolytes Studied By Diffusion and Relaxation NMR *Sarah Mailhiot, Bruker Biospin, Germany*
11:30	Boosting resolution and sensitivity for operando studies of catalytic processes *Igor V. Koptyug, International Tomography Center, Russia*
11:45	Large scale MRI for imaging of processes *Stefan Benders, Hamburg University of Technology, Germany*

12:00	Radiofrequency Receive Coil Arrays for Large-Bore Vertical 3T MRI in Process Engineering *Muhammad Adrian, Hamburg University of Technology, Germany*
12:15	Magnetic Resonance Imaging of Structured Packings: Overcoming Spatial, Signal, and Geometric Challenges *Hannah Rennebaum, Hamburg University of Technology, Germany*
12:30	**Lunch**
13:30	**General Assembly Meeting**
	Scientific Session 9: Microscopy & Cellular **Chair:** Dan Xiao, University of Windsor, Canada
14:15	Deep Learning–Based Compressed Sensing Reconstruction for High-Resolution MRI of Human Embryos *Kazuma Iwazaki, University of Tsukuba, Japan*
14:30	Dynamic Magnetic Resonance Sampling Pattern Guided by Deep Reconstruction *Zaimin Zhu, Beijing University of Posts and Telecommunications, China*
14:45	Optical Widefield Nuclear Magnetic Resonance Microscopy *Julia Draeger, Technical University Munich, Germany*
15:00	Ultra-high field MRI and spatially resolved spectroscopy of organoids at 28.2 T *Julia Krug, Wageningen University & Research, Netherlands*
15:15	Refocused Acquisition of Chemical Exchange Transferred Excitation: Use of Phase in Exchange MRI *Peter Jakob, University of Würzburg, Germany*
15:30	**Closing**

Book of Abstracts of the 18th ICMRM

17th – 21st of August 2025

at the

University of Würzburg

Germany

Book of Abstracts

Book of Abstracts

ICMRM '25

Educational Session

Optimizing signal-to-noise for portable low field MRI systems

A.G.Webb, C.Najac, B.Lena, R. van der Broek
C.J.Gorter MRI Center, Department of Radiology, Leiden University Medical Center, Leiden, The Netherlands

Introduction: The recent growing interest in portable point-of-care (POC) MRI (1-4) has been driven by the concept of increasing the accessibility of a traditionally extremely expensive imaging modality. POC low-field systems increase access to MRI by enabling it to be used in situations in which it has not previously been possible: examples include the intensive care unit and emergency room in the developed world, and sites in lower and middle income countries (LMICs) which lack the finance and/or infrastructure for conventional MRI systems (5-9). The two major technical challenges of POC MRI are much lower signal-to-noise ratio (SNR) and much higher magnet field (B0) inhomogeneity compared to conventional clinical systems. This talk will consider the intrinsic SNR, and how RF coil and MR sequence design can be used to optimize image quality

RF Coil design.

Unlike the situation at conventional clinical field strengths, coil loss dominates for portable low field systems. This means that low-loss coil design is critical for obtaining the highest SNR. Litz wire can be used to obtain Q values >500. However, high Q also comes with challenges. The coil bandwidth may be less than the imaging bandwidth and the ring-down time can cause quite severe pulse shape distortions. In addition, construction of receive array coils becomes extremely challenging due to the very high inter-coil coupling in the absence of body loading.

MR sequence design.

The field dependence of dipole-dipole interactions means that the T_1 values of tissue are substantially shorter than at clinical field strengths, with the T_2 values remaining very similar. This has the advantage of allowing more rapid pulsing, but the disadvantage that tissue contrast between, for example, white matter and gray matter is reduced. Since it is essentially liquid, the cerebrospinal fluid has very long T_1 and T_2 values, making sequences such as fluid attenuated inversion recovery (FLAIR) very time consuming. The specific absorption ratio (SAR) is not a concern for portable systems, and so long train turbo spin echo (TSE) sequences can be run, with the echo train length (ETL) only limited by the available gradient strength. Given all of these considerations, sequence design is a multi-factorial process, which continues to evolve: Figure 1 shows current results from our 46 mT system with different clinically-relevant contrasts.

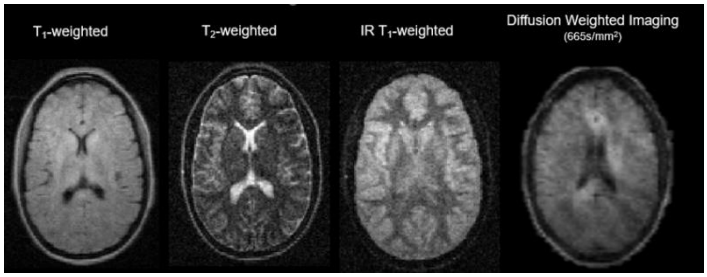

Figure 1. Images acquired on a healthy volunteer on a portable 46 mT scanner. Spatial resolution 1.5 x 1.5 x 5 mm, diffusion 2.5 x 2.5 x 6 mm. Imaging times: 4 mins, 10 mins, 10 mons and 16 mins, respectively.

References: [1] Liu YL et al.. Nat Commun 2021;12(1).[2] Yang L et al. IEEE T Bio-Med Eng 2022;69(11):3415-3426. [3] O'Reilly T et al. Magn Reson Med 2021;85(1):495-505.[4] Cooley CZ et al.Nat Biomed Eng 2021;5(3):229-239.[5] Salameh N et al. MAGMA 2023;36(3):329-333. [6] Arnold TC et al. J Magn Reson Imaging 2023;57(1):25-44.[7] Samardzija A et al. Annu Rev Biomed Eng 2024;26(1):67-91.[8] Kimberly WT et al. Nat Rev Bioeng 2023;1(9):617-630. [9] Wald LL et al. Magn Reson Imaging 2019.

How to build a new imaging modality … and make it work

P. Vogel[1,2]
[1]Experimental Physics V (Biophysics), University of Würzburg, Germany
[2]phase VISION GmbH, Rimpar, Germany

Abstract: Magnetic Particle Imaging (MPI) is an emerging tomographic imaging modality that offers high sensitivity, high temporal resolution, and quantitative capabilities without ionizing radiation. Since its first demonstration in 2005, MPI has evolved into a versatile platform for imaging magnetic nanoparticle distributions in vivo, with growing relevance for preclinical imaging, diagnostics, and theranostics [1,2].

This talk aims to provide a comprehensive overview of MPI tailored for physicists interested in the intersection of magnetism, instrumentation, and biomedical applications.

Beginning by demystifying the physical principles underlying MPI, including the nonlinear magnetization response of superparamagnetic nanoparticles and the generation of spatial encoding fields. A comparative look at different scanner geometries – such as field-free point (FFP) and field-free line (FFL) configurations – will shed light on how spatial resolution and acquisition speed can be optimized.

On the hardware side, several key components are required for building an MPI system, including gradient and drive-field coils, receive chains, and analog-digital converter.

After digitization, there are multiple strategies for image reconstruction, nanoparticle characterization, and calibration techniques that enable accurate and quantitative imaging.

Emphasis will also be placed on the fingerprinting of nanoparticles and how these can be used to distinguish between particle types, states, or functionalization.

Finally, the talk will highlight recent advances and promising near-future applications of MPI, such as real-time vascular imaging, cell tracking, hyperthermia applications, and functional imaging.

Fig. 1: From the idea behind Magnetic Particle Imaging to the application in the clinical environment.

Whether you're a physicist curious about novel imaging technologies or a researcher considering MPI for your own applications, this session will equip you with the fundamental understanding and practical perspective needed to engage with this rapidly evolving field.

References: [1] A. Davida, B. Basari, J.Appl.Phys. 136:220701 (2024). [2] C. Billings et al, Int.J.Mol.Sci. 22:7651 (2021).

Portable MRI scanner: Magnet designs, gradient coils, and open-source resources

Shaoying HUANG
Singapore University of Technology and Design

Magnetic resonance imaging (MRI) is an important imaging modality for diagnostic and therapeutic purposes. It offers the best soft tissue contrast without ionizing radiation. However, due to the high cost and/or immobility, it is only available in the radiology department in a hospital and to less than 30% of the world population. A conventional MRI cannot be taken to a patient. Portable MRI is compact with light weight and a small footprint, and is low cost. Its compactness makes MRI available to the bedside of a patient, and to the sites, e.g., in an ambulance and a medical tent for disaster rescues. The low cost makes MRI more available to the under-developed counties and regions.

With the advancements of 3D printing technology and when personal computers become more affordable and powerful for signal acquisition and image processing, building one MRI scanner in the lab or by oneself as a hobby becomes possible. The talk will provide a detailed introduction on the design and building of permanent magnet array and gradient coils for portable MRI scanners, and the open-source resources.

Book of Abstracts

ICMRM '25

Plenary Session

30 Years of SRMR

30 years of SRMR: The 1990s

Prof. Dr. Axel Haase

Technical University of Munich

The 1990s are widely regarded as one of the most formative and diverse decades in the evolution of Magnetic Resonance Imaging (MRI). This era brought landmark advances across clinical, preclinical, and non-biological domains. Key developments included the introduction of high-field MRI systems (≥ 3 T), the emergence of functional MRI using the BOLD contrast mechanism, the advent of diffusion-weighted and diffusion tensor imaging (DWI/DTI), and the rise of parallel imaging methods such as SMASH and SENSE. Sequence innovations like MP-RAGE, the first real-time cardiac imaging in mice, and portable systems like the NMR-MOUSE further expanded the scope of MRI into previously uncharted territories.

In parallel to all these exciting advances in MRI a new series of conferences, the ICMRM, was initiated in 1991 at Heidelberg and its society, the Division of Spatially Resolved Magnetic Resonance, was founded in 1995 during the meeting in Würzburg.

Of course, any historical account of this period reflects the lens of the observer. Depending on one's background, certain milestones may seem more defining than others. And speaking with a wink: those who were actively contributing to MRI during this decade—including the author—may carry a particularly personal bias in selecting what mattered most. Still, there is broad agreement that the 1990s shaped the field in ways that continue to define modern MRI practice and research.

Remembering ICMRM 2001 - 2009

B. Blümich
Institut für Technische und Makromolekulare Chemie
RWTH Aachen University, Aachen, Germany

The first International Conference on Magnetic Resonance Microscopy (ICMRM) was an endeavor initiated by Winfried Kuhn and Bernhard Blümich, enthused by the many opportunities which pulsed gradient fields in magnetic resonance provide. Both were engaged in Magnetic Resonance Imaging beyond biomedical applications with an interest in materials and plant science [1,2]. It took place in Heidelberg in 1991, the same year that Paul Callaghan's seminal book "Principles of Nuclear Magnetic Resonance Microscopy" was published [3]. Paul Lauterbur gave the opening lecture and Raymond Andrew the after-dinner talk [4]. The success of the conference encouraged the organizers to have the 2nd ICMRM two years later. Then Sir Peter Mansfield gave the opening lecture. At this meeting it was agreed to form Division of Spatially Resolved Magnetic Resonance within the AMPERE Society, and Raymond Andrew subsequently worked out the by-laws. The third ICMRM in Würzburg commemorating the 100th anniversary of the discovery of X-rays by Wilhelm Conrad Röntgen in Würzburg was the first ICMRM organized by the new AMPERE Division.

The year before the first ICMRM, the first International Conference on Magnetic Resonance in Porous Media was organized at the University of Bologna. The second one followed in 1993, the same year the 2nd ICMRM took place. As both meetings were of interest to largely the same community, they were subsequently aligned to take place biannually in alternating years. One major topic at the MRPM was relaxometry with stray-field NMR sensors for well-logging. This stimulated the interest in mobile low-field NMR for materials testing so that in 2001 a Colloqium on Mobile Magnetic Resonance (CMMR) was organized by RWTH Aachen University in Bacherach. The CMMR was subsequently repeated every year with the number of attendees growing form initially about 20 to about 80 in 2006. To alleviate the burden of organizing it, it was eventually made part of the ICMRM and MRPM beginning with the 2007 ICMRM in Aachen. Both conferences feature mobile NMR session still today.

Hot conference topics of the first decade of the current millennium were two-dimensional Laplace NMR, mobile stray-field NMR instrumentation, methodology for well-logging and depth profiling including applications to cultural heritage, fast MRI for studying the dynamics of transient processes, and more [6]. Among others were Paul Callaghan and Eiichi Fukushima were regular contributors. The progress in field of magnetic resonance microscopy over the years is summarized in four edited books based on ICMRM conferences [4–7]. Selected conference highlights of the period from 2001 to 2010 will be reviewed and recalled with photos.

References

[1] B. Blümich, H.W. Spiess, NMR Imaging of Materials, Angewandte Chemie 100 (1988) 1460–1461; B. Blümich, NMR Imaging of Materials, Clarendon Press, Oxford, 2000.
[2] W. Kuhn, NMR Microscopy – Fundamentals, Limits and Possible Applications, Angewandte Chemie Int. Eng. 29 (1990) 1–19.
[3] P.T. Callaghan, Principles of Nuclear Magnetic Resonance Microscopy, Clarendon Press, Oxford, 1991.
[4] B. Blümich, W. Kuhn, eds., Magnetic Resonance Microscopy – Methods and Applications in Materials Science, VCH, Weinheim, 1992.
[5] P. Blümler, B. Blümich, R. Botto, E. Fukushima, eds., Spatially Resolved Magnetic Resonance – Methods, Materials, Medicine, Biology, Rheology, Geology, Ecology, Hardware, Wiley-VCH, Weinheim, 1998.
[6] S.L. Codd, J.D. Seymour, eds., Magnetic Resonance Microscopy – Spatially Resolved NMR Techniques and Applications, Wiley-VCH, Weinheim, 2009.
[7] S. Haber-Pohlmeier, B. Blümich, L. Ciubanu, eds., Magnetic Resonance Microscopy – Instrumentation and Applications in Engineering, Life Science, and Energy Research, Wiley-VCH, Weinheim, 2022.

ICMRM in the 2010's

S. L. Codd[1],
[1]Montana State University, Bozeman, USA

We'll start the 2010's off in 2009 with a trip down memory lane to geysers, moose, and a wonderful week of science on the edge of Yellowstone Park in Montana, USA. We gathered throughout this decade as a community in Beijing, Cambridge (UK), Munich, Halifax and Paris. The 2010's were a time of loss for our community with the passing of Sir Paul Callaghan, but also a time of great advances by the young investigators in our community. We honored his leadership by giving his name to the Young Investigator sessions. This decade will be covered by revisiting the some of the Young Investigators you heard from at those meetings from the Montana State University lab and collaborators and by remembering the places in which we gathered, and those we gathered with.

The 2020s in MRI: Precision, Integration, and Open Science

Luisa Ciobanu

Neurospin, CEA-Saclay, France

In the past few years, MRI has undergone rapid development — from the expansion of ultra-high-field (UHF) systems to new ways of combining MR with other techniques. In this talk, I will highlight recent advances in UHF MRI, including enabling technologies such as advanced RF coils, parallel transmission, and improved shimming methods. I will show how combining MR with approaches like two-photon microscopy and calcium imaging helps us better understand the origins and limits of the MR signal. I will also briefly mention how AI-based methods are being explored to enhance image acquisition and reconstruction, along with ongoing efforts in standardization and data sharing that aim to support more reproducible and collaborative research.

Book of Abstracts

ICMRM '25

Scientific Session 1

Flow & Diffusion

Careful Comparison of MRI and Computer Simulations of Bubbly, Particle-Laden Flows

C.M. Boyce
Columbia University, New York, NY, USA

Introduction: MRI has long been used to characterize bubble motion in multiphase flows as well as fluid and particle velocity in particle-laden flows. These measurements can be used to validate or find areas for improvement in computational fluid dynamics (CFD) models. However, the post-processing of CFD data for accurate comparison with MRI measurements is often non-trivial due to complexities of MRI measurements. Here, we discuss development and utilization of MRI techniques to measure a range of bubbly, particle-laden flows as well as use of MRI simulations to identify the best ways to compare MRI measurements with CFD simulations.

Methods: A range of MRI pulse sequences, from single-point imaging to echo planar imaging are used to characterize multiphase flows [1]. Multi-band EPI is introduced to take rapid images of 3D bubble structures [2]. Measurements are conducted in both pre-clinical and full-body MRI scanners. Particle and gas flow are modeled using computational fluid dynamics – discrete element method (CFD-DEM) simulations [3]. MRI simulations are conducted with in-house codes as well as JEMRIS software [4]. Oil inside particles are used to measure particle flow and ^{19}F nuclei inside SF_6 gas is used to measure gas flow [5]. Flow is measured inside fluidized beds [5–7], bubble streams in dense suspensions [2] and analog lava flows (**Fig. 1**) [8].

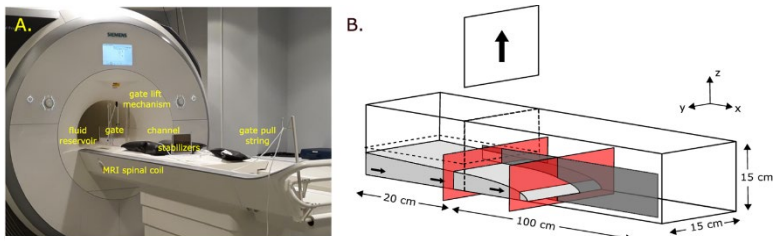

Fig. 1 Experimental setup for MRI of lava analog flows.

Results and Discussion: MRI measurements of fluidized beds show that particle and gas velocities are fastest directly in the line of bubbles, and slowest to the sides of bubbles [5,7]. Simulations of fluidized beds simulated as passing through an MRI pulse sequence reveal the most accurate ways to process particle positions and velocities for comparison with MRI simulations [9,10]. Fully 3D measurement of bubble streams in dense suspensions reveal highly non-axisymmetric bubble shapes, particularly surrounding bubble coalescence [2]. MRI velocimetry of lava analog flows can be used to develop new rheological models for magma [8].

Conclusions: MRI can characterize structural and flow features of bubbly, particle-laden flows. MRI simulations applied to output of CFD simulations reveal the most accurate ways to postprocess CFD data for comparison with simulations. MRI pulse sequences can be tailored to meet the specific resolution requirements of a particular flow system.

References: [1] E. Lev and C. M. Boyce, *iScience* (2020). [2] A. Bordbar, W. Zia, J. Birnbaum, J. Omidi, R. F. Lee, E. Lev, and C. M. Boyce, *Chemical Engineering Journal* (2024). [3] Y. Tsuji, T. Kawaguchi, and T. Tanaka, *Powder Technology* (1993). [4] T. Stöcker, K. Vahedipour, D. Pflugfelder, and N. J. Shah, *Magnetic Resonance in Medicine* (2010). [5] C. M. Boyce, N. P. Rice, A. Ozel, J. F. Davidson, A. J. Sederman, L. F. Gladden, S. Sundaresan, J. S. Dennis, and D. J. Holland, *Phys. Rev. Fluids* (2016). [6] A. Penn, A. Padash, M. Lehnert, K. P. Pruessmann, C. R. Müller, and C. M. Boyce, *Phys. Rev. Fluids* (2020). [7] A. Penn, T. Tsuji, D. O. Brunner, C. M. Boyce, K. P. Pruessmann, and C. R. Müller, *Science Advances* (2017). [8] J. Birnbaum, W. Zia, A. Bordbar, R. F. Lee, C. M. Boyce, and E. Lev, *Journal of Geophysical Research: Solid Earth* (2023). [9] C. M. Boyce, D. J. Holland, S. A. Scott, and J. S. Dennis, *Ind. Eng. Chem. Res.* (2013). [10] A. Bordbar, S. Benders, W. Zia, A. Penn, and C. M. Boyce, *Ind. Eng. Chem. Res.* (2023).

MRI measurement of fluid mechanical properties in granular flow

K. John[a], V. Klempau[a], Sanyogita[b], A. Khan[b], P.R. Nott[b], S. Grundmann[a], M. Bruschewski[a]
[a]Institute for Fluid Mechanics, University of Rostock, Rostock, Germany
[b]Department of Chemical Engineering, Indian Institute of Science, Bangalore, India

Introduction: The transport and processing of granular materials pose longstanding industrial challenges due to their complex mechanical behavior. While numerous studies have explored the kinematics of granular flow and suspensions, these investigations are mainly limited to transparent boundaries or free surfaces. The interior flow remains poorly understood, largely due to the opacity of granular media to light. Non-invasive imaging techniques like X-ray CT and MRI [1-4] have been employed to probe these flows, but previous studies often suffered from limited field of view or insufficient spatial resolution.
This study aims to advance the use of MRI for capturing 2D and 3D spatially resolved flow fields of granular media in both canonical (e.g., Couette cell) and complex geometries (e.g., flow around obstacles and in screw feeders). These configurations have seen limited investigation, and we anticipate that MRI will yield new insights into the mechanics of granular materials and enable rigorous testing of continuum models, particularly regarding the coupling between density and velocity fields. The data may also contribute to the development of models for cohesive granular media, which remain poorly understood.

Methods:
Experiments are conducted at the MRI Flow Lab at the University of Rostock, a DFG-funded core facility equipped with a 3T whole-body MRI system (Magnetom Trio, Siemens). The lab has previously validated high-accuracy flow imaging methods using gradient-recalled echo (GRE)[5] and single-point imaging (SPI)[6], focusing on minimizing displacement artifacts and higher-order gradient moment effects, which are key sources of error in velocity-encoded MRI.
One of the main challenges in MRI of granular flows is the short T2* relaxation time of natural granular materials such as oilseeds. Although spin echo (SE) sequences are commonly used in granular media studies, their long encoding times and higher-order gradient artifacts limit their accuracy for fluid mechanics. This study, therefore, employs GRE and SPI sequences and optimizes experimental design to match their requirements.

Results and Conclusion: The project is currently in the commissioning phase, focusing on validating both the imaging sequences and the custom-designed granular media. A significant innovation is the development of gel-water beads coated with a polymer shell that supports GRE imaging without requiring ultra-short echo times. In addition to much longer T2*, these particles offer better-controlled experimental boundary conditions than natural granular materials, which typically have variable geometry and uncontrolled surface properties. Manufacturing these particles was challenging since over 10,000 such particles are needed for meaningful granular flow experiments. The successful fabrication of this MRI-optimized granular material marks a key milestone.
Initial experiments are being carried out in a large-scale Couette setup containing approximately 30,000 particles, previously studied using optical methods and numerical simulations. These MRI measurements provide spatially resolved velocity data, paving the way for a deeper understanding of granular flow mechanics in realistic conditions.

References: [1] Losert, Phys. Rev. Lett. (2000). [2] Meuth, Nature (2000) [3] Baker, Nat. Commun. (2018). [4] Clarke, Particuology (2023). [5] Romig, Magn. Reson. Imag. (2025). [5] Bruschewski, Magn. Reson. Med. (2019).

Spectrally Resolved Turbulent Flow in Porous Structures Using Modulated Gradient Diffusion NMR

D. Clarke[1], *D. Topgaard*[1]
[1]Division of Physical Chemistry, Lund University, Lund, Sweden

Introduction: Turbulent flow is relevant to fields such as meteorology, medicine, and chemical engineering. Turbulence has been quantified using pulsed field gradient NMR over the last 35 years. Despite widespread use, these measurements lack specificity, returning only the mean squared fluctuating velocity. Analogous to restricted diffusion, modulated gradient methods [1] have been proposed to measure the turbulent energy spectrum [2] thereby gaining more information on the microscale characteristics of the flow.

Methods: We simulated the NMR signal from computational fluid dynamics simulations. We consider two cases: (1) direct numerical simulation (DNS) of homogeneous turbulence [3] that resolves eddies at all scales. (2) large eddy simulation (LES) of a periodic Schwarz Diamond network [4]. Trajectories (Fig. 1) were generated from the velocity fields for use in the NMR simulations. The modulated gradients were designed using the workflow in [5].

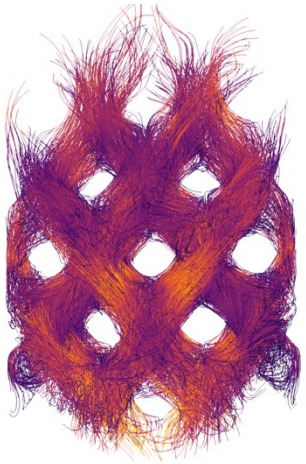

Fig. 1: Trajectories for turbulent flow in a Schwarz Diamond network used to simulate modulated gradient NMR experiments.

Results and Discussion: The diffusion spectrum tensor for the homogeneous DNS obtained using simulated NMR was in excellent agreement with the ground truth. Because NMR operates in a Lagrangian frame (following nuclei along their trajectories), the power-law scaling of the diffusion spectrum is -2 and not -5/3 observed by optical and probe techniques. Simulated experiments on the LES were in poor agreement with the ground truth because the assumption of a Gaussian phase distribution was not satisfied. Instead, the phase follows a Laplace distribution (Fig. 2), illustrating the need for an appropriate theoretical formulation, or gradient waveforms that can produce a Gaussian phase distribution.

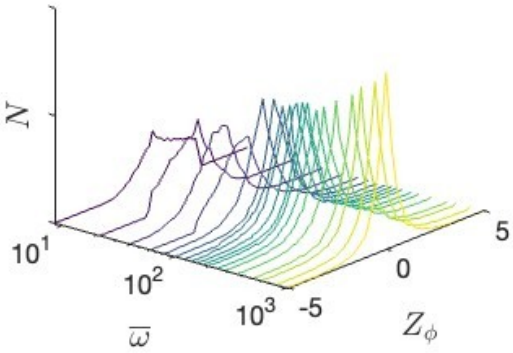

Fig. 2: Distribution of phase for simulated modulated gradient NMR experiments showing a Laplace distribution.

Conclusions: Modulated gradient diffusion NMR can accurately measure the turbulent diffusion spectrum provided that the assumption of a Gaussian phase distribution is met. This method allows for more detailed study of turbulence features such as isotropy, energy cascading, and dissipation in various systems. Experiment design for microimaging and preclinical systems is the subject of ongoing work.

References: [1] Callaghan & Stepišnik, J. Magn. Reson. (1995). [2] Dillinger, et al., Magn. Reson. Med. (2022).
[3] Biferale, et al., TURB-Lagr Database (2024). [4] Clarke, et al., Chem. Eng. J. (Submitted)
[5] Jiang, et al., Magn. Reson. (2023).

Rapid Flow Characterization Measurements Using a Modified CPMG Measurement with Incremented Echo Times, Phase Cycling and Filtering

S. J. Richard, B. Newling and B. J. Balcom
MRI Centre, University of New Brunswick, Fredericton, Canada

Introduction: We present a low-field magnetic resonance (MR) rheology technique for characterizing pipe flows with a simple, low-cost setup [1-3]. By analyzing the phase and magnitude of a series of single spin echoes acquired at varying τ, we extract the average velocity and flow behavior index to reconstruct the flow velocity profile. A modular benchtop system built around ceramic magnets and a pitched magnet sensor design enables flexible operation, including controlled pre-polarization length for slow-polarizing fluids like aqueous solutions. Recent advances include an echo-train acquisition scheme [4] that gathers N echoes per CPMG sequence, reducing experiment time by a factor of 1/N. Phase cycling and filtering improve signal quality by suppressing unwanted coherence pathways.

Methods: Analysis of spin echo phase and magnitude as a function of τ in a constant gradient enables reconstruction of the velocity profile (Fig. 1). An echo-train acquisition scheme with incrementally adjusted τ, combined with 4-step phase cycling and filtering, allows rapid data collection while minimizing coherence pathway artifacts and preserving optimal pulse spacing.

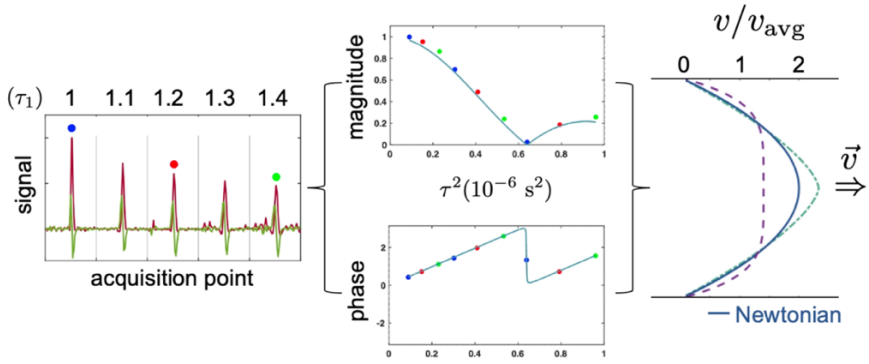

Fig. 1: In a magnetic field gradient, a modified CPMG echo train with variable τ yields flow-sensitive echoes. Phase and magnitude data are fit to a signal model to extract average velocity (v_{avg}) and flow behavior index (n), which define the velocity profile.

Results and Discussion: Validation experiments conducted with Newtonian and shear-thinning fluids confirmed the effectiveness of the methodology. Additionally, the approach reliably distinguishes between laminar and turbulent regimes with high sensitivity. The faster echo-train acquisition scheme produced results consistent with the original method of individual spin echo acquisitions. Our 4-step phase cycling strategy, combined with incremented pulse spacings, enabled acquisition of N = 3 echoes per train in our benchtop apparatus. Incorporating an optional filtering strategy to further mitigate off-resonance effects suggests the approach can be extended to at least N = 5, while also improving echo signal normalization without any requirement to stop the flow.

Conclusion: We developed a simple, low-cost MR method and apparatus for rheological measurements of pipe flow using spin echoes at varying τ. With incremented pulse spacings, phase cycling and optional filtering, we achieve the same flow-sensitive echo response in less time. The modular hardware is easily adapted for industrial use. We anticipate extending this work to a new online viscosity (rheology) measurement, providing a less disruptive alternative to conventional methods and addressing industry need for improved real-time rheological monitoring

References: [1] Guo et al, Phys. Fluids. (2022). [2] Richard et al, Phys. Fluids. (2023). [3] Richard et al. Phys. Fluids. (2024), [4] Richard et al, J. Magn. Reson. (submitted)

Ex-Vivo Diffusion Tensor Characterization of Peri-Fibrotic Myocardial Regions In Myocardial Infarction

Ali Nahardani[1], Rao Dai[1], Miriam Schiffer[2,3], Bernd K Fleischmann[2], Wilhelm Roell[3], Verena Hoerr[1]
[1] *Department of Internal Medicine II, University Hospital Bonn, Bonn, Germany*
[2] *Institute of Physiology I, Medical Faculty, University of Bonn, Bonn, Germany.*
[3] *Department of Cardiac Surgery, University Hospital Bonn, Bonn, Germany.*

Introduction:

Diffusion tensor imaging (DTI) is a powerful MRI technique for studying tissue microstructure, though its use in the cardiovascular system poses technical challenges [1]. Recently, ex vivo cardiac DTI has become a key tool for examining how cardiomyopathies affect heart structure. This study investigates changes in diffusion properties and macrostructure of the peri-infarct areas during chronic myocardial infarction (MI), with DTI findings supported by histology.

Methods:

3D multishell Stejskal–Tanner DTI was performed on an ex vivo heart with myocardial infarction at an 11.7 T Bruker scanner using a transceive cryoprobe and two reference power settings to reduce excitation field inhomogeneity. Imaging parameters included three b-values (0, 1500, 3000 s/mm²) and the spatial resolution of 200 µm³. The diffusion data were reconstructed as described in [2]. Mean, axial, and radial diffusivity maps (MD, AD, and RD, respectively), fractional anisotropy (FA), and restricted diffusion index (RDI) were calculated. To assess fibrosis, samples were fixed in formalin afterwards, frozen, sectioned (10 µm slices, 100 µm intervals), and stained with Sirius Red and Fast Green (SR/FG). Tractography-based fiber orientations were finally reconstructed and compared with histological images.

Results and Discussion:

MD, AD, and RD were significantly higher in peri-infarct tissue than in remote myocardium ($P < 0.05$), suggesting that MRI and the collagen deposition disrupts tissue integrity and enhances water diffusion. FA was also elevated in peri-infarct regions, reflecting higher anisotropy from dense collagen alignment. RDI was higher in peri-infarct areas, consistent with increased extracellular collagen seen in histology. Tractography and SR/FG staining confirmed transverse fiber orientations and collagen alignment along mesocardial sheetlets in peri-fibrotic zones (Fig. 1).

Conclusion:

Diffusion metrics and histological findings converge to provide a coherent depiction of chronic post-infarction remodeling with elevated MD, AD, RD, and RDI in peri-infarct regions. Tractography and SR/FG staining matched with fiber orientations, highlighting DTI's effectiveness in capturing fibrosis, cell loss, and fiber reorganization in chronic MI.

References:

[1] Dall'Armellina, E., et al, *J. Cardiovasc. Magn. Reson.* **27**, 101109 (2025).
[2] Yeh, F. C., Wedeen, V. J., Tseng, W. Y., *IEEE Trans. Med. Imaging* **29**, 1626–1635 (2010).

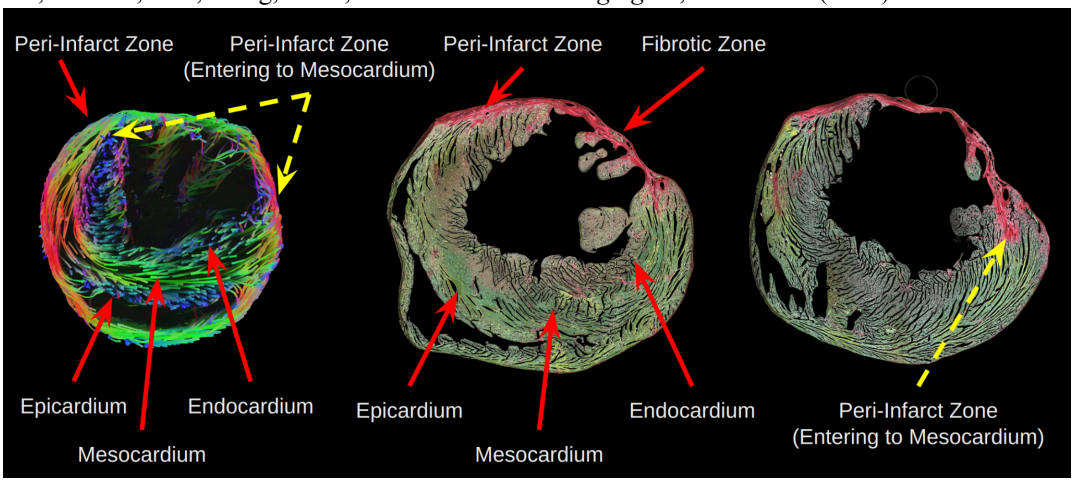

Fig 1. Representative image showing the peri-infarct zone's fiber tracking correlation with the SR/FG histology

Microstructural Assessment of Oral Squamous Cell Carcinoma Using Time-Dependent Diffusion MRI

C.J. Guichelaar[1], M.M. Jokivuolle[2], R. van de Woude[1], H.J.G. Smits[1], G.E. Breimer[1], A. van der Toorn[1], K.H. Madsen[3], H. Lundell[3], F. Mahmood[2], M.E.P. Philippens[1]

[1]University Medical Center Utrecht, Utrecht, the Netherlands, [2]Odense University Hospital, Odense, Denmark, [3]Danish Research Centre for Magnetic Resonance, Hvidovre, Denmark

Introduction: Although diffusion-weighted (DW) MRI and its derived metric, the apparent diffusion coefficient (ADC), are widely used for tumour assessment[1], ADC provides limited insight into specific microstructural features such as cell density (CD)[2]. Time-dependent diffusion contrast (TDDC) was previously introduced to characterise tumour microstructure[3]. This study tested the hypothesis that TDDC is a more specific measure of CD than ADC in oral squamous cell carcinoma (OSCC).

Methods: *Ex vivo* DW-MRI was performed on ten fresh OSCC specimens using a 3 T MRI (Ingenia 3 T, Philips HealthCare, The Netherlands) with three diffusion sequences: two pulsed gradient waveforms (pWF_{short}, pWF_{long}) and one oscillating (oWF) waveform, with effective diffusion times of 26, 46, and 16 ms. Two TDDC maps were generated by subtracting normalised DW-MRI signals with the same b-value: $TDDC_o$ (pWF_{long} – oWF) and $TDDC_p$ (pWF_{long} – pWF_{short}). After MRI, specimens were formalin-fixed, sectioned parallel to MRI slices, paraffin-embedded, and stained with haematoxylin and eosin (HE). Tumours were manually delineated on the HE-stained slices, and a cell detection algorithm generated CD maps. Within the tumour delineation, voxel-wise and ROI-based correlation analyses were conducted on TDDC, ADC, and CD maps (Figure 1).

Results and Discussion: In the voxel-wise analysis, $TDDC_o$ demonstrated a stronger correlation with CD than $TDDC_p$ ($TDDC_o$: ρ_s= 0.23 [-0.03, 0.42], $TDDC_p$: ρ_s= 0.06 [-0.08, 0.31], ADC: ρ_s= -0.04 [-0.57, 0.27]), likely due to higher SNR in $TDDC_o$. Stronger correlations between CD and both TDDC maps were observed in the ROI-based analysis ($TDDC_o$: ρ_s= 0.58, $TDDC_p$: ρ_s= 0.79), while ADC showed a weaker inverse correlation with CD (ρ_s= -0.47), further highlighting the potential advantage of TDDC for characterising tumour microstructure. Future studies should focus on a larger sample size and quantify histological features such as stromal content and tumour-infiltrating lymphocytes to refine our understanding of TDDC's relationship with tumour microstructure.

Conclusion: The findings support the hypothesis that TDDC is a more specific measure of CD than ADC and show promise for improved characterisation of tumour microstructure in OSCC.

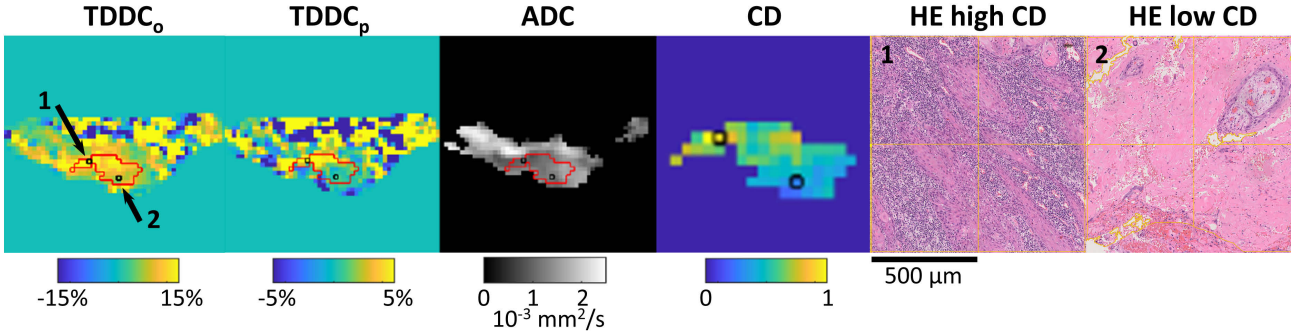

Fig. 1: Visualisation of the TDDC maps, ADC map, zoomed-in CD map and two magnified sections of the HE-slice from voxel 1 and 2 (black arrows). A positive percentage in the TDDC maps corresponds to more restricted diffusion. The tumour delineation is visualised in red on the TDDC and ADC maps. Voxel 1 (high TDDC, high CD) showed tumour cells with lymphocyte infiltration, while voxel 2 (low TDDC, low CD) contained mainly keratin structures.

References: [1] Koh, AJR Am J Roentgenol (2007). [2] Bourne, Diagnostics (2016). [3] Jokivuolle, Med Phys (2025).

Book of Abstracts

ICMRM '25

Scientific Session 2

Mobile & Low Field

Halbach 2.0 – Creating homogenous fields with finite size magnets

Ingo Rehberg[1] and Peter Blümler[2]

1) Experimental Physics, University of Bayreuth, 95440 Bayreuth, Germany
2) Institute of Physics, University of Mainz, 55128 Mainz, Germany

Homogenous magnetic fields can be created by suitable arrangements of permanent magnets, with Halbach rings being a well-established approach [1,2]. These rings are most effective when composed of very long (theoretically infinite) magnetic rods, modeled as line dipoles.

However, the classical Halbach concept is inherently limited when dealing with finite-sized permanent magnets. To overcome this, three-dimensional configurations of such magnets have been explored. In [3], optimal designs for both single and stacked rings of point dipoles are presented, achieving superior field strength and homogeneity compared to the original Halbach design and previous numerical approximations [4].

The key innovation is the so-called *focused configuration*, achieved by tilting the dipoles out of the plane of the ring. This design enables highly homogeneous fields that are shifted out of the magnet plane—an essential feature for single-sided magnetic resonance applications [5].

Furthermore, rotating these tilted rings relative to one another further enhances field homogeneity, albeit at the expense of a uniform field direction. However, such configurations remain suitable for NMR, as the field vector rotates only within the transverse plane of the rings, while the axial direction remains stable and can be used for rf excitation.

The theoretical predictions are validated through experimental realizations of various magnet arrangements using cuboid magnets (see Fig. 1).

The results demonstrate that these novel configurations effectively overcome the limitations of finite-sized magnets in Halbach arrays, providing enhanced field strength and homogeneity. This makes them particularly well-suited for applications in mobile magnetic resonance.

All configurations can be explored, analyzed, and exported for 3D printing via a dedicated Python GUI [6].

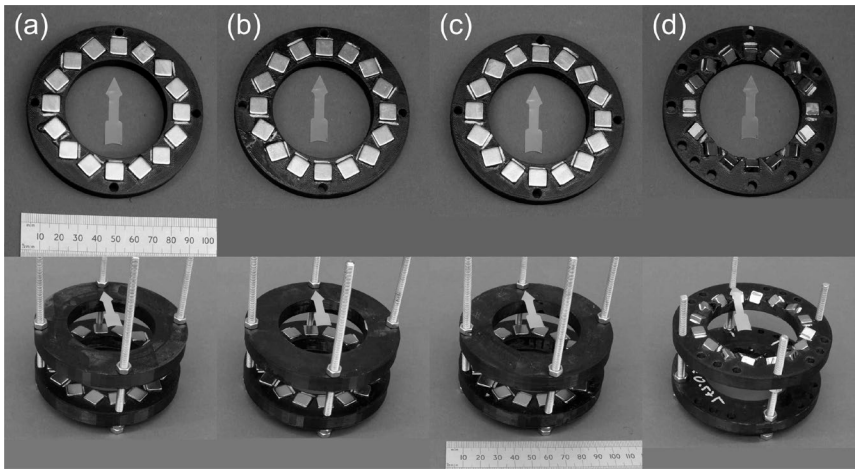

Fig. 1: Top row single rings, bottom row stacked version. (a) classical Halbach, (b) according to [4], (c,d) focused configuration (c) with focal length, f=0 , and (d) f = -0.576.

References:

1. K. Halbach, Nuclear Instruments and Methods **169**, 1 (1980).
2. P. Blümler, H. Soltner,. Appl. Magn. Reson. **54**, 1701 (2023).
3. I. Rehberg, P. Blümler, https://arxiv.org/abs/2502.18262 (2025).
4. S. Tewari, T. O'Reilly, and A. Webb, Journal of Magnetic Resonance 324, 106923 (2021).
5. P. Blümler, F. Casanova, in Mobile NMR and MRI: Developments and Applications, The Royal Society of Chemistry (2015).
6. I. Rehberg, P. Blümler, https://zenodo.org/records/15064360 (2025).

A New Approach for Shimming Halbach Ring Magnets: Magnetically Soft Materials

Andrew F. McDowell[1], J. Beau W. Webber[2]
[1]NuevoMR, LLC, Albuquerque, USA, [2]Lab-Tools, Ltd, Ramsgate, UK

Introduction: The Halbach Ring Magnet design is attractive due to its mathematical sophistication, compact size, and expected high homogeneity. Also, significant resources exist to aid those wishing to build their own [1]. However, the homogeneity achieved is often less than hoped for and may undermine applications requiring better field quality. We have adapted our methods for using magnetically soft materials for passive shimming [2] to the Halbach Ring Magnet geometry. Magnetically soft materials are more precise and accurate than hard materials and are generally easier to manipulate. By using these passive materials, we seek to achieve field improvements previously requiring thorough material characterization and careful mechanical adjustment of permanent magnet blocks.

Methods: Magnetically soft materials become magnetized in the direction of B_0 once placed in the magnet. Hence, the use of soft materials for the ring magnet configuration requires a rethinking of the geometrical properties of the shim fields. Following a method inspired by the work of Anderson [3], we show that the unipolar material can produce the familiar harmonic fields of either sign. We demonstrate that a compact shim structure defined by a small number (64) of localized regions of constant magnetic moment density is capable of producing harmonic fields through the fourth order, or more.

Results and discussion: We have used 3D printed shims to correct a lab-made 0.3T Mandhalas-style magnet and a 0.5T ring magnet built from arc-segments. We have also applied both 3D printing and 2D magnetic ink printing to correct a much more homogeneous 1.4T magnet. Figure 1 shows two examples in the form of before/after field maps.

Commercially available soft magnetic materials such as ink for jet printing or filament for 3D printing are consistent enough to allow for shimming to succeed. In addition, the available printers and software are well-suited to rapid, nearly automatic production of inexpensive shims. The lack of steel in a Halbach Ring Magnet allows theoretically simple calculation of the expected shim fields with adequate accuracy for developing useful shim designs.

Conclusion: The ability to use well-engineered consumer printers (both 3D and 2D) for shim production removes practical barriers for considering complex designs. We show that the magnetic ink and filament materials, together with their printing processes, are accurate enough to realize the calculated design at a useful precision. We discuss the remaining limitations for achieving very high homogeneity, including the lack of magnetic strength in the ink shims and the need to develop custom software for controlling the 3D printer. Magnetically soft materials provide an effective and efficient path to higher homogeneity Halbach Ring Magnets.

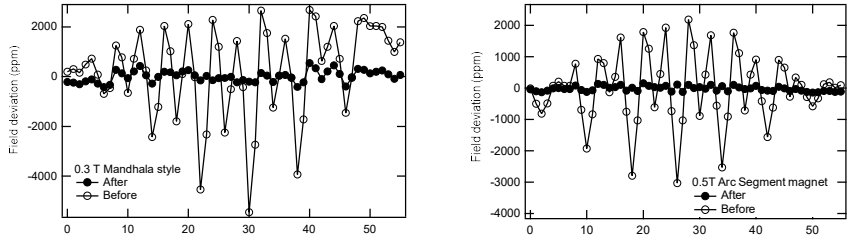

Fig. 1: Before/After 10mm spherical field maps of two Halbach Ring Magnets.

References:
[1] Blümler, Conc. Mag. Reson. (2004).
[2] McDowell, App. Magn. Reson. (2023).
[3] Anderson, Rev. Sci. Inst. (1961).

Adaptive magnetic field mapping to accelerate the B_0 shimming process in a low-field MRI using Gaussian process regression

M. Ochsendorf[1,2], *K. Lavronenko*[1,2], *V. Schulz*[1,2]
[1]Fraunhofer Institute for Digital Medicine MEVIS, Bremen, Germany
[2]RWTH Aachen University, LfB Institute, Aachen, Germany

Introduction: The homogeneity of the static magnetic field B_0 is a decisive factor for image quality in magnetic resonance imaging (MRI) [1]. This is especially true in low-field MRI systems, such as those based on permanent magnet arrays around 50 mT, where field inhomogeneities are pronounced and difficult to correct. A key challenge in these systems is the efficient acquisition of the B_0 field map required for the shimming process [2,3]. Conventional techniques typically rely on dense 3D grid measurements, which are time-intensive and often impractical, particularly for iterative or interactive shimming procedures [4]. To address this, we present a real-time adaptive magnetic field mapping approach that selectively samples regions of high inhomogeneity or model uncertainty. This significantly reduces measurement time without compromising accuracy.

Methods: A cost-effective modular measuring system based on a converted 3D gantry has been developed. Despite its rudimentary mechanics, it allows precise sub-millimeter 3D scans using IMU sensor-based calibration procedures to correct mechanical tolerances. A bounding-box model ensured collision-free operation in constrained geometries. The adaptive measurement algorithm initializes with a coarse-resolution survey scan, based on which a probabilistic modeling of the magnetic field is performed using Gaussian Process Regression (GRP) [5]. It is based on its ability to provide a continuous field distribution and a spatially resolved, quantitative uncertainty estimate. Based on the posterior variance, new measurement points are added in regions of maximum model uncertainty in each iteration. The measurement process is continued in closed loop operation, until the uncertainty predicted by the model in the volume is below a predefined value [6].

Results: In addition to the simulation data, the OSII 30 cm Halbach magnet was measured to evaluate the adaptive measurement strategy [3]. A reference scan with 10 mm point spacing over a Volume of 200 mm length and 200 mm diameter yielded 7k points and required a total scan time of 36 hours. The adaptive GPR-based method required only about 1k points of specially selected measurement points (Fig. 1), resulting in an 85 % reduction in time. This resulted in an MSE of 15.4 uT and an MAE of less than 92.6 uT, leading to an overall inhomogeneity loss of 348 ppm compared to the reference. This is acceptable as the overall homogeneity of the field in the reference is 36k ppm.

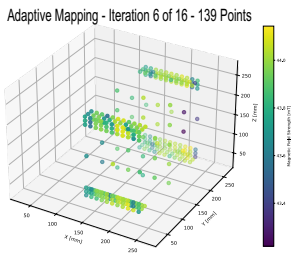

Fig. 1: Initial survey measurement in the center with 100 points. After the 6th of 16 iterations, 395 were added, mostly placed on the shell of the magnet volume.

Conclusion: The presented method for real-time adaptive magnetic field mapping using GPR demonstrates a reduction in the measurement effort for interactive user B_0 shimming applications in low-field MRI systems. The number of required measurement points can be significantly reduced in intermediate shimming steps, thus significantly reducing the iteration time.

References:
[1] de Graaf et al., Anal. Biochem (2017), [2] Wenzel et al., Front. Phys., (2021), [3] O'Reilly et al., J. Magn. Reson (2019), [4] Stockmann et al., IEEE Trans. Med. Imaging, (2018), [5] Solin et al., Magnetic field interpolation with GPR, IEEE Trans. Robotics, (2018), [6] Arunkumar et al., Adaptive sampling for GPs with mobile sensors, IROS, (2011)

A Self-Supervised Inversion Framework for Low-Field 2D NMR Relaxation Spectra with Embedded Fluid-Specific Physical Priors

Gang Luo, Sihui Luo, Lizhi Xiao, Guangzhi Liao, Rongbo Shao
China University of Petroleum, Beijing, China

Introduction

Low-field nuclear magnetic resonance (NMR) is a key technique in downhole logging for non-invasive characterization of fluid composition. Two-dimensional spectra (T_1-T_2, D-T_2) enhance sensitivity to fluid differentiation and reservoir evaluation [1]. However, limited acquisition time and tool mobility in low-field environments often lead to sparsely sampled, noisy data, making the inverse Laplace transform highly ill-posed. Conventional regularized methods struggle to provide stable, high-resolution spectra, especially in systems with overlapping relaxation components. These challenges highlight the need for inversion frameworks that embed fluid-specific physical priors and leverage data-driven approaches to improve stability and interpretability under sparse acquisition conditions.

Methods

This study introduces a self-supervised deep learning framework for 2D NMR relaxation spectrum inversion (Fig.1), integrating physical priors of fluid relaxation behavior. The model is composed of three modules: (1) a multi-scale convolutional encoder with positional encoding for hierarchical feature extraction; (2) a self-attention mechanism to enhance recognition of long-delay and weak signals; and (3) a physics-informed module that embeds a multi-exponential decay forward model, enabling spectrum-to-echo reconstruction as part of a self-supervised loss. Additionally, fluid-relaxation priors [2] (e.g., for bound water and hydrocarbons) are introduced as spectral priors, guiding the network toward physically consistent outputs.

Results and discussion

Experiments show that the method achieves stable, high-fidelity spectrum reconstruction under sparse and low-SNR conditions, with enhanced peak localization and reduced artifacts compared to traditional methods. The integration of physical relaxation priors further improves interpretability and robustness in realistic measurement situation.

Conclusion

This work presents a novel self-supervised inversion framework for 2D low-field NMR data, integrating fluid-specific physical priors to enhance spectral resolution, stability, and interpretability. The approach is particularly effective in complex environments and holds strong potential for extension to multi-dimensional relaxation analysis and complex reservoir evaluation.

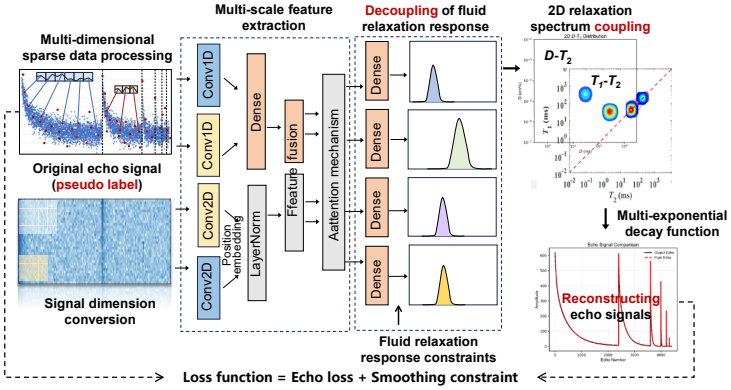

Fig. 1: A Self-Supervised Inversion Framework for 2D NMR Relaxation Spectra with Embedded Fluid Response Coupling.

References:

[1] Lizhi Xiao. Practical NMR for Oil and Gas Exploration. Royal Society of Chemistry, (2023).
[2] Yi-Qiao Song, Ravinath Kausik. NMR application in unconventional shale reservoirs – A new porousmedia research frontier. Progress in Nuclear Magnetic Resonance Spectroscopy. (2019).

A Frequency Selective Surface (FSS) Shield for Portable Low-Field MRI

Junqi YANG[1], Meena RAJENDRAN[2], Shaoying HUANG[2], Wenwei YU[1]

[1]Chiba University, Chiba, Japan, [2]Singapore University of Technology and Design, Singapore

Introduction: Portable low-field MRI systems suffer by low signal-to-noise ratio. It require effective RF shielding to suppress environmental noise while preserving coil sensitivity. Traditional copper shields offer strong noise attenuation[1] but often reduce B_1 field strength when placed near the coil[2]. To overcome this trade-off, we propose a wire-mesh Frequency Selective Surface (FSS) that does both shielding and sensitivity conservation for solenoid coils.

Methods: Three shielding configurations—no shield, solid copper shield, and FSS shield (Fig. a)—were simulated and fabricated, all impedance-matched to 50 Ω. Bench measurements (B_1 sensitivity, noise suppression) and imaging tests with phantoms and fruit samples were conducted using a 100 mT unshielded MRI system.

Result: As the Fig. b shows that the FSS shield suppressed over 90% of external noise while maintaining higher coil sensitivity than the copper shield. Imaging tests showed ~30% higher SNR than the copper case and nearly 10× improvement over the unshielded configuration (Fig. c).

Conclusion: The proposed FSS shield enables efficient noise suppression in portable, unshielded MRI systems without compromising coil sensitivity. This compact design provides a practical shielding solution for low-field MRI in challenging environments. Evaluation of the proposed wire-mesh Frequency Selective Surface (FSS) shield for noise suppression in low-field MRI.

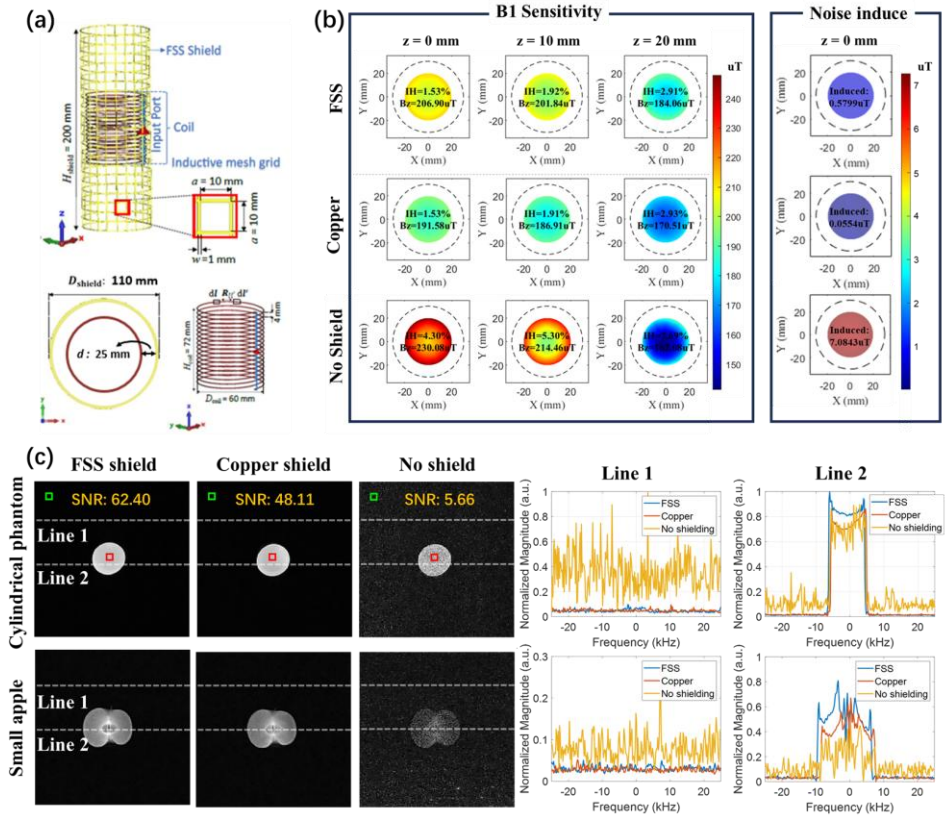

Fig: (a) FSS geometry: a solenoid coil (diameter 60 mm, pitch 4 mm) enclosed in an FSS mesh shield with 10 mm pitch and 1 mm wire width. (b) Simulated B_1 sensitivity maps and induced noise distributions for FSS, copper, and no shielding configurations. At various imaging depths (z = 0, 10, 20 mm). (c) Imaging results for cylindrical phantom and fruit sample (small apple).

References: [1] de Vos B, et al., Journal of Magnetic Resonance, 2024, 362: 107669. [2] Ochi H, et al. Electronics and Communications in Japan, 1994, 77(1): 37-45.

Low-field Magnetic Resonance in Harsh Environments

M.L. Johns[1], K.T. O'Neill, E.O. Fridjonsson
School of Engineering, University of Western Australia, Perth, WA, Australia

Low-field nuclear magnetic resonance (NMR) is now a well-established measurement utilised in laboratory and logging environments for characterisation of porous media. NMR enables determination of porosity, fluid volumes and a qualitative estimation of permeability in complex geological environments. Considerable technological advances in the design of NMR instruments has already enabled complex measurements to be performed in a range of challenging environments, such as oil and gas reservoirs and Antarctic sea ice. This work examines extending NMR towards three applications with challenging operating and measurement conditions: (i) designing an NMR logging-while-drilling (LWD) tool to operate in hard rock iron ore mining, (ii) performing accurate quantitative characterisation in iron ore, and (iii) characterising water in space exploration.

NMR LWD is now an everyday service in the oil and gas industry, enabling real-time formation evaluation. Mineral exploration drilling is highly unfavourable to LWD due to the 'high' shocks and vibrations experienced. Designing an NMR LWD tool for such environments requires a detailed understanding of the impact of tool motion on NMR measurements during logging. This involves conducting electromagnetic simulations which quantify the magnetic fields generated by a logging tool, and subsequently introducing motion profiles within the relevant spin dynamic calculations [1]. Such simulations can then be used to optimise the design of the tool to be robust to tool motion. The critical design considerations are reducing the radial magnetic field gradient as well as the echo spacing in order to reduce the degree of signal attenuation due to motion.

NMR measurements of water within iron ore samples is complicated by the presence of high internal magnetic field gradients due to magnetic susceptibility differences at the ore–water interface. Advanced 2D relaxometry measurements can be used to quantify key material properties. We utilise Decay due to internal fields Carr-Purcell Meiboom-Gill (DDIF-CPMG) measurements to quantify 2D l_s-T_2 (where l_s is the pore length scale) which is subsequently used to quantify the surface relaxivity of samples. Multi-echo measurements (consecutive CPMG measurements at variable echo spacing) can then be used to determine T_2–g_{eff} (where g_{eff} is the effective internal gradients). A new method, called the multi-regime model, is used to model the diffusive NMR signal attenuation in internal gradients [2]. The multi-regime model is a key step in accurately segregating surface relaxation and diffusive relaxation in high susceptibility materials. This is crucial in accurately estimating properties such as pore size distributions and permeability in these iron ore samples.

Finally, we consider the application of NMR towards extra-terrestrial materials in consideration of using NMR for space exploration. This is achieved by conducting laboratory NMR measurements on Lunar and Martian regolith simulants [3]. DDIF-CPMG measurements are used to quantify the pore-size distributions. These measurements are translated to particle size distributions (using a simple pore-to-particle model) and validated against laser particle size analysis measurements. Multi-echo measurements are used to quantify water volumes as both clay-bound and inter-particle water. The NMR measured moisture content showed reasonably good agreement to corresponding gravimetric measurements used for validation. Finally, we discuss the implications of the current measurements for space exploration and the use of NMR to monitor plant growth in these simulants.

References: [1] K.T. O'Neill, Jnl Mag. Res., 337, 107167 (2022) [2] K.T. O'Neill, Geophys. Jnl Int., 232, 3, 2017 (2023) [3] K.T. O'Neill, ICARUS, 339, 115544 (2023).

MagTetris+: A rapid simulator for magnetic field and force calculation for ferromagnetic materials and permanent magnets

Jing Han Heng[1], Junqi Yang[2], Wenwei Yu[2], Shao Ying Huang[1]
[1]Singapore University of Technology and Design, Singapore, [2]Chiba University, Chiba, Japan

Introduction: Ferromagnetic materials play a significant role in many applications due to their strong magnetic responses under an external magnetic field, such as shimming permanent magnet arrays in NMR and MRI. However, rapid and accurate simulations of ferromagnetic materials remain challenging due to nonlinear hysteresis[1] and interactions of magnetization domains[2] which are the regions with uniform magnetization. Conventional numerical methods such as Finite Element Method (FEM) are computationally intensive and time-consuming[3,4], thus creating a growing need for rapid simulations of high accuracy using low computational resources and time.

Method: MagTetris+ extends the magnet-only simulator MagTetris[5] to calculate magnetic field (**B**) and force of systems comprising both ferromagnetic materials and magnets. Magnetization (**M**) of a single-magnetization domain object is determined using Curie-Weiss Law[6], incorporating the contributions from an external magnetic field ($\mathbf{H_{Ext}}$), self-demagnetization and hysteresis. Mangetocrystalline anisotrophy field[7] is approximated using the angle between $\mathbf{H_{Ext}}$ and **M** rather than using the object's easy axes traditionally[7]. MagTetris+ discretizes a large ferromagnetic object into multiple domains and ensures stable and quick convergence of their interactions with a damping factor which prevents oscillation or divergence of **M**.

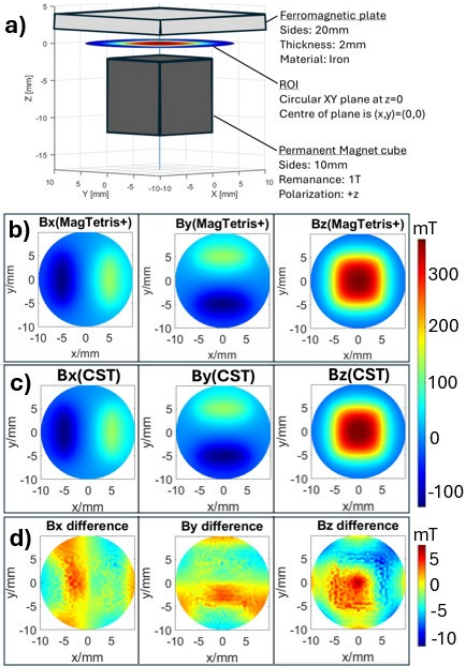

Fig. 1

Results and Discussion: MagTetris+ is benchmarked against CST magnetostatic solver (with sufficient meshes) [8] on the same setup (Fig.1(a)): a large ferromagnetic plate subjected to $\mathbf{H_{Ext}}$ generated by a permanent magnet. Fig.1(b)&(c) displays their **B**s on the region of interest (ROI) and Fig.1(d) shows their difference maps. As shown, the calculated **B** by MagTetris+ is visually and quantitatively consistent with CST, proving high accuracy. To complete the simulation, CST took 40 minutes and 50GB of peak memory consumption while MagTetris+ only requires 0.1 seconds and 0.5GB. Thus, MagTetris+ possess speedup of 2400x and is 100x more memory-efficient against CST.

Conclusion: MagTetris+ is a simulator for ferromagnetic materials and magnets which circumvent the computational bottlenecks of FEM mesh-based solvers. The computation time and resource requirements are significantly reduced, which facilitate integration with optimization algorithms and real-time design workflows. MagTetris+ offers a practical alternative to FEM-based tools with high computational efficiency and accuracy, thus accelerating research and development in various ferromagnetic applications such as passive shimming and iron yoke design for NMR and MRI.

References: [1] Zheng, Elsevier. (2025) [2] Zeng, Elsevier. (2023) [3] Yan, Pier. (2015) [4] Dular, IEEE. (2024) [5] Liang, JMR. (2023) [6] Mugiraneza, Nature. (2022) [7] Kim, ACM. (2018) [8] www.3ds.com/products/simulia/cst-studio-suite

Book of Abstracts

ICMRM '25

Scientific Session 3

Biomedical Imaging

Magnetic Resonance Fingerprinting: Promise and Challenges

Nicole Seiberlich
University of Michigan, Ann Arbor, MI, USA

Magnetic Resonance Fingerprinting (MRF) is an approach for efficiently and simultaneously measuring multiple tissue properties. By tuning acquisition parameters and applying specialized reconstruction approaches, MRF can be deployed to assess T1, T2, PDFF, T1r, and/or T2* in organs including the brain, heart, liver, and prostate. While this powerful technique has been demonstrated in a variety of research settings, it has not yet been translated for clinical use. This presentation will introduce the concept of MRF and its potential for tissue characterization, as well as the challenges faced by MRF which currently limit its clinical adoption.

Magnetic resonance fingerprinting enables high-resolution joint morphometry and relaxometry of the inner ear

J. Stebani[1,2], P. Dawood[1], P. Albertova[1,3], K. Rak[4], P. M. Jakob[1], M. Blaimer[2], M. Gram[1,3]

[1]Experimental Physics 5, University of Würzburg, Würzburg, Germany, [2]Magnetic Resonance and X-Ray Imaging Department, Fraunhofer Institute for Integrated Circuits IIS, Würzburg, Germany, [3]Department of Internal Medicine I, University Hospital Würzburg, Würzburg, Germany, [4]Department of Oto-Rhino-Laryngology, University Hospital Würzburg, Würzburg, Germany

Introduction: Pathologies of the inner ear (IE) - including sensorineural hearing loss, tinnitus, vertigo, and Meniere's disease - present significant diagnostic challenges with conventional MRI [1,2]. Quantitative MRI (qMRI) offers a potential alternative, but current studies are limited. In this work, we developed a high-resolution 3D magnetic resonance fingerprinting (MRF) sequence for joint morphometry and relaxometry of key IE structures.

Methods: The IE-MRF sequence was implemented using the open-source Pulseq framework [3] and based on an Inversion-Recovery FISP readout [4]. Isotropic resolution of 250 µm was achieved using a variable-density spiral readout and trajectory correction. Dictionary-based low-rank reconstruction and pattern matching was implemented for T_1 and T_2 quantification [5]. The method was validated using synthetic inner ear fluids and applied in vivo on a 3T MRI scanner in a healthy volunteer, with segmentation of cochlea, vestibulum, semicircular canals (SCC), and nerve. Relaxometry values were compared with gold-standard techniques.

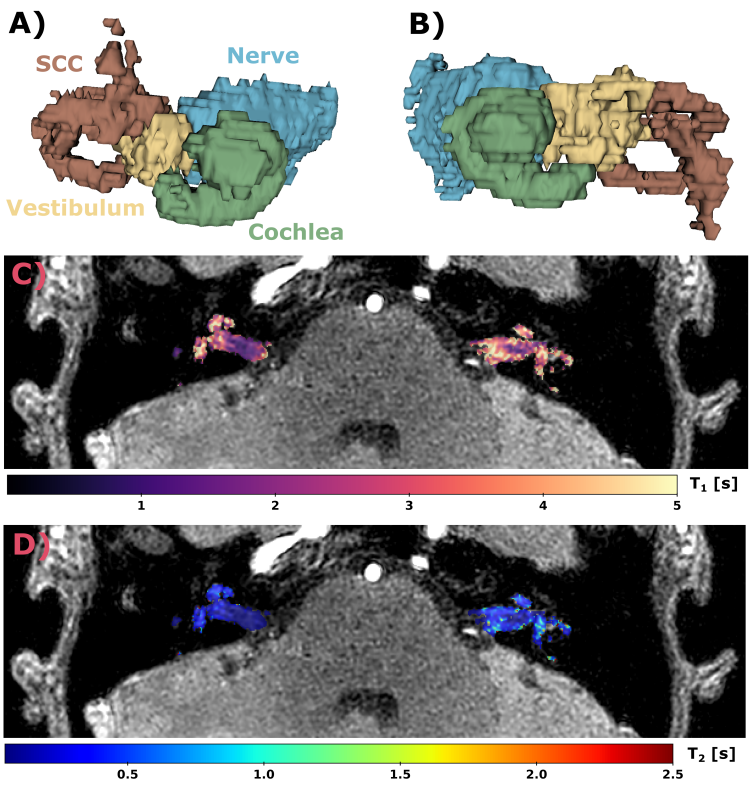

Morphometry of the left (A) and right IE and T_1 (C) and T_2 (D) relaxation time maps generated with the 3D-IE-MRF sequence.

Results: IE-MRF enabled segmentation and quantitative mapping of major inner ear structures, with high agreement for cochlea, vestibulum, and nerve. However, segmentation of the SCC was incomplete due to low signal and partial volume effects. Relaxation times for synthetic fluids and in vivo subregions were consistent with prior literature, with T_2 values slightly reduced in vivo, likely due to temperature effects.

Conclusion: High-resolution 3D IE-MRF allows combined morphometric and relaxometry assessment of the inner ear and may offer new insights into challenging IE pathologies. While current limitations include signal quality in the SCC and scan duration, future improvements in coil design, acceleration techniques, and high-field imaging are expected to enhance its clinical applicability.

References: **[1]** Davis et al. Bulletin of the World Health Organization. 97(10);646 (2019). **[2]** Benson et al. Radiology. 297(2);252-265 (2020). **[3]** Layton et al. Magn Reson Med. 77(4);1544-1552 (2017). **[4]** Jiang et al. Magn Reson Med. 74(6);1621-1631 (2015). **[5]** Hamilton et al. NMR in Biomedicine. 32(2);e4041 (2019)

Deep Learning-Based Algorithm for Reconstructing Diffusion Tensor Distribution Imaging Parameters

Jiayin Zhou[1], Zaimin Zhu[1], Daniel Topgaard[2], Pak Shing Kenneth[2], Fangrong Zong[1*]
(1.School of Artificial Intelligence, Beijing University of Post and Telecommunication , Beijing, 100876, China
2. Physical Chemistry, Lund University, P.O.B. 124, SE-22100 Lund, Sweden)

Introduction: Traditional diffusion magnetic resonance imaging (dMRI) methods struggle to characterize multiple diffusion properties within a single voxel. In contrast, diffusion tensor distribution (DTD) imaging provides diffusion tensor distribution for each voxel, offering more precise information on tissue diffusion characteristics. From the diffusion tensor distribution, essential metrics related to tissue diffusion can be computed, such as the expected values of isotropic and anisotropic diffusion, their variances, covariance, and the expected values of isotropic and anisotropic diffusion of three properties (gray matter, white matter, cerebrospinal fluid) delineated by the distribution[1]. Currently, Monte Carlo (MC) inversion remains the most prevalent method for obtaining diffusion tensor distribution. However, it faces challenges: it requires expensively computational resources and entails lengthy solution times, limiting its practical application. Moreover, MC methods independently handle each voxel without considering the spatial continuity of diffusion properties.

Methods: To address these issues, we propose a deep learning model called DTDMapper. This model takes dMRI signals as input and generates DTD metrics in an end-to-end manner. Figure 1 illustrates the model framework.

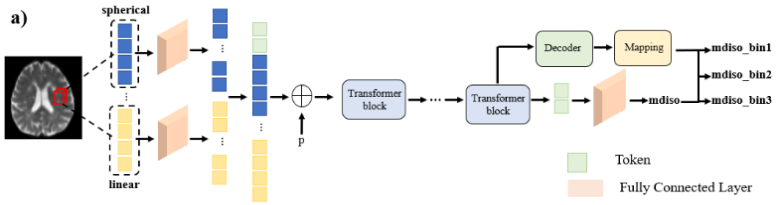

Figure1. The network framework consists of three parts: encoder, decoder. an encoder employs attention mechanism to capture relationships between central and neighboring voxels; a decoder utilizes multiple threshold and convolutional layers to emulate sparse dictionary construction and lookup.

Results and discussion: In Figure 2, the left figure illustrates the process of calculating the signal fractions using DTD, while the right side compares the model predicted results with those obtained from MC inversions. Across all parameters, SSIM surpasses 0.9. Compared with MC, our model achieves nearly a 15-fold reduction in parameter prediction time and smoother results.

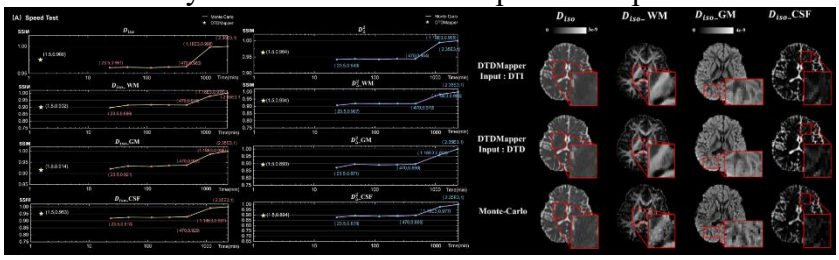

Figure 2 (A) Speed Test experiment. The horizontal axis represents the required computation time (minutes), while the vertical axis shows the SSIM compared the results of 1, 2, 5, 10, 20, 50, 100 times MC and DTDMapper (star) with reference. (B) Analysis of Output Accuracy experiment. Comparison of isotropic and anisotropy metrics of healthy subjects sub017 (male, 23 years old, MRI) under DTDMapper and Monte Carlo methods.

Conclusion: This study introduces the first application of a deep learning model for computing diffusion tensor distribution parameters, effectively addressing computational complexity and spatial continuity issues inherent to Monte Carlo methods. Our approach holds promise for widespread adoption in clinical and research settings.

References: 1. Topgaard D. Diffusion tensor distribution imaging. *NMR Biomed*. 2019;32(5):e4066. doi:10.1002/nbm.4066

From the central and peripheral nervous system to cardiac conduction: biomagnetic field detection using rotary excitation

P. Albertova[1,2], *C. L. Schäfer Gomez*[2,3], *T. Kampf*[2,3], *M. Schindehütte*[3], *P. Nordbeck*[1], *P. M. Jakob*[2], *M. Gram*[1,2]

[1]*Department of Internal Medicine I, University Hospital Würzburg, Würzburg, Germany*
[2]*Experimental Physics 5, University of Würzburg, Würzburg, Germany*
[3]*Neuroradiology, University Hospital Würzburg, Würzburg, Germany*

Introduction: Rotary Excitation (REX) is a phenomenon that occurs during the spin-lock (SL) state, enabling the detection of oscillating magnetic fields in the pico- to nanotesla range [1]. Originally proposed for detecting neural activity (low-frequency oscillations in the Hz range), REX has been applied for imaging alpha activity [2] and for the clinical localization of the seizure onset zone in focal epilepsy [3]. In this study, we demonstrate that the REX detection concept can be extended to non-sinusoidal fields, such as those arising in the peripheral nervous system (PNS) and cardiac conduction.

Methods: Physiological models of biomagnetic fields were generated from electromyography data acquired during 50 Hz electrical stimulation of the median nerve, as well as from magnetocardiography data of the cardiac QRS complex [4]. For both scenarios, optimal SL preparation parameters (SL duration t_{SL} and amplitude f_{SL}) were determined by means of Bloch simulations. Field detection was validated experimentally using a clinical 3T MRI system. The time-varying biomagnetic fields were emulated using the scanner's built-in gradient system within a spherical calibration phantom.

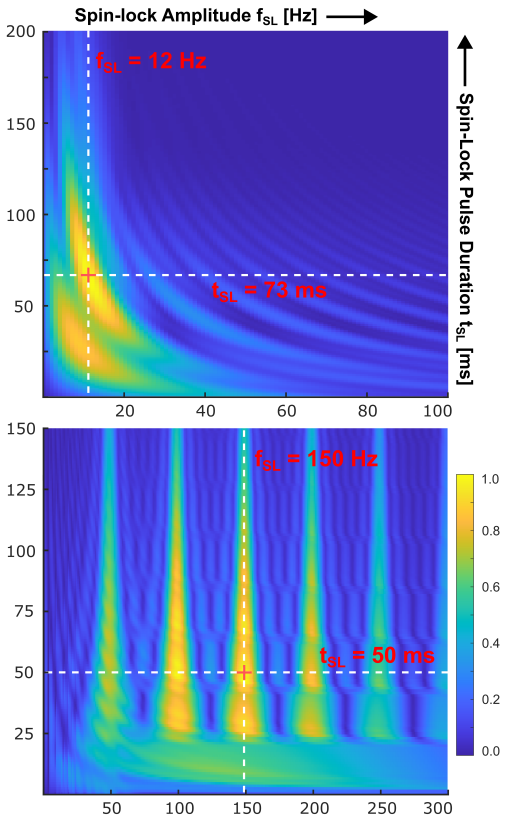

Bloch simulation: maximum REX response for cardiac QRS (top) and PNS fields (bottom).

Results: Optimal SL durations and amplitudes were determined for both applications. For detecting cardiac fields with a QRS duration of 100 ms, the maximum REX response was observed at 73 ms and 12 Hz. For the electrical 50 Hz PNS stimulation, maxima occurred at 50 ms and integer multiples of 50 Hz, with the global maximum at 150 Hz. The manifestation of global maxima in the millisecond range can be explained since the REX effect induces magnetization components, while relaxation effects counteract and reduce these components. Experimental validation confirmed the detectability of both field types using the optimized parameters, with minimum detectable field magnitudes of 1 nT and a spatial resolution of 2×2×5mm.

Conclusion: REX-based field detection was originally developed for purely sinusoidal waveforms. However, the potential applications are considerably broader, as REX is a resonance phenomenon that generates detectable magnetization whenever the SL amplitude matches a main frequency component of the temporal waveform. In this context, REX can be interpreted as spectral Fourier analysis for magnetic fields. Future studies will aim to transfer the optimized and phantom-validated protocols to ex vivo models and subsequently to in vivo detection of biomagnetic fields.

References: **[1]** Witzel et al.42(4):1357-65 (2008) **[2]** Truong et al. Magn Reason Med. 81(6):3462-3475 (2019) **[3]** Kiefer et al. Radiology. 280(1):237-43 (2016) **[4]** Jensen et al. Sci Rep. 8:16218 (2018)

Post-Traumatic Osteoarthritis Following a Sub-Critical Impact by µMRI

Amanveer Singh, Yang Xia
Oakland University, Rochester, Michigan, USA

Introduction: Osteoarthritis (OA) is a degenerative joint disease affecting millions of people, leading to pain and disability due to the degradation of articular cartilage [1]. Since treating OA becomes challenging if it is not diagnosed early, it is essential to understand the progression of the disease. This study focuses on the progression of post-traumatic osteoarthritis (PTOA) from the early stage through 14 weeks after a single sub-critical impact (~30MPa) to the femur in rabbits.

Methods: A total of thirty NZW rabbits were used to track OA progression following a controlled mechanical injury to the right knee femur while the non-impact left femurs served as a control for comparison. After the impact, the rabbits were divided into five groups of six and sacrificed at 0, 2, 6, and 14 weeks to assess OA progression in the femur articular cartilage (AC). At the 6-week timepoint, two groups were compared to evaluate the severity of cartilage damage, with one group receiving the sub-critical impact and the other with an impact ~65MPa. The intact rabbit knees were imaged using a 7T µMRI and cartilage damage was monitored using MRI T2 mapping where T2 values tracked the deterioration of the cartilage. To better study the effects of impact on cartilage the total cartilage thickness was divided into two equal regions (upper and lower) for analyzing T2 values.

Results and Discussion: After a sub-critical impact to the femur AC, a gradual increase in T2 values was observed in both regions of impact cartilage over time, indicating progressive cartilage degradations through 0, 2, 6, and 14 weeks. At 2 and 6 weeks, the changes in T2 values between non-impact and impact AC were slightly elevated when compared to the baseline (week 0), suggesting the onset of OA with early tissue damage. By 14 weeks, statistically significant changes were observed in T2 values for both regions between non-impact and impact AC indicating continued degradation of cartilage (Fig 1). At the 6-week timepoint, notable differences were seen between the 30MPa and 65MPa groups. Gradual increase in T2 values of femur AC following a sub-critical impact indicates that a direct minor injury to the cartilage can lead to significant cartilage degradation and OA development over time (Fig 2). Higher T2 changes between non-impact and impact AC for the 65MPa group suggests that a stronger mechanical force can speed up cartilage degradation [2, 3].

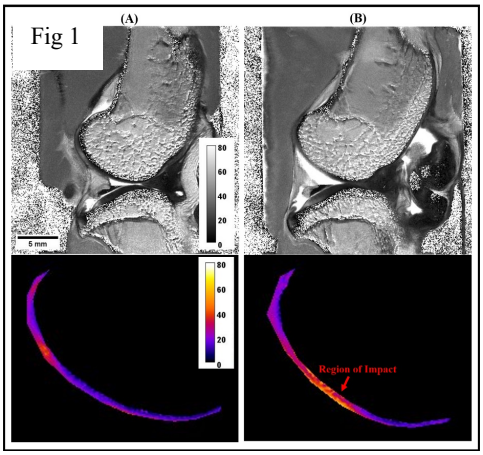

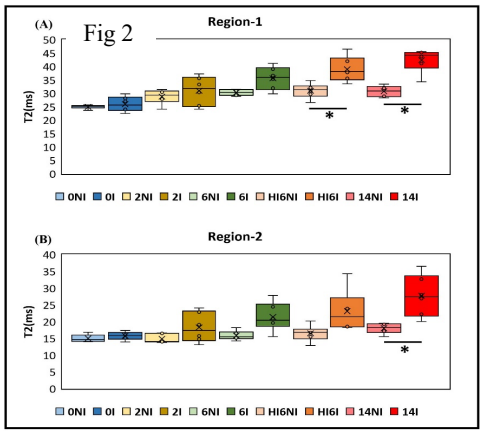

Conclusion: This study demonstrates the effectiveness of MRI T2 imaging for successfully tracking OA progression following a mechanical injury to the knee joint. The findings of this study can contribute to a better understanding of OA progression, biomechanical factors involved in OA progression, and the need for early OA diagnosis to plan for successful treatments.

References: [1] Xia, Bone Joint Res. (2013). [2] Mantebea, et al, J. Ortho. Res. (2024). [3] A Singh, et al, Connective Tissue Res. (2024).

Noninvasive Measurement of Fascia Thickness in Porcine Models for Investigating Myofascial Pain Using Single- Sided NMR

A. Jenna Necaise[1], B. Vi Nguyen[1], C. Lauren Boudreaux[1], D. Jonathan Q. Brown[1], E. Peter J Basser[2], F. Velencia Witherspoon [1,2]

[1]Tulane University Department of Biomedical Engineering, New Orleans, USA, [2]Eunice Kennedy Shriver National Institute of Children's Health and Human Development, NIH, Washington D.C., US

Introduction: Myofascial Pain Syndrome (MPS) is a chronic disorder marked by muscle pain and fascial stiffness yet lacks objective diagnostic tools—contributing to opioid overuse and unreliable treatment approaches like acupuncture. Fascia densification, a key feature of MPS, may serve as a useful biomarker. This study investigates single-sided NMR as a noninvasive technique to measure fascia thickness and identify MPS biomarkers in porcine models, chosen for their anatomical similarity to humans.

Methods: Thoracolumbar tissue samples from 12 pigs (ages 11–18 months) were collected post-mortem with fascia intact. Fascia thickness was assessed noninvasively using a single-sided NMR device (NMR-MOUSE PM25, 13.19 MHz, Magritek) at 27 °C, acquiring T_1, T_2, and diffusion data. Signal analysis was performed in MATLAB using both exponential and stretched exponential models. Validation methods included optical imaging with SYBR Gold and Eosin staining analyzed in FIJI, and ultrasound imaging (Vevo 2100, 21 MHz) for comparison.

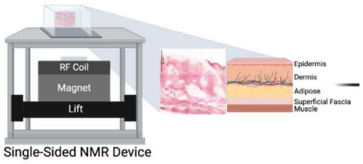

Fig. 1:Cross-sectional schematic of NMR sampling geometry, illustrating layered tissue structure from epidermis to muscle.

Results and Discussion:

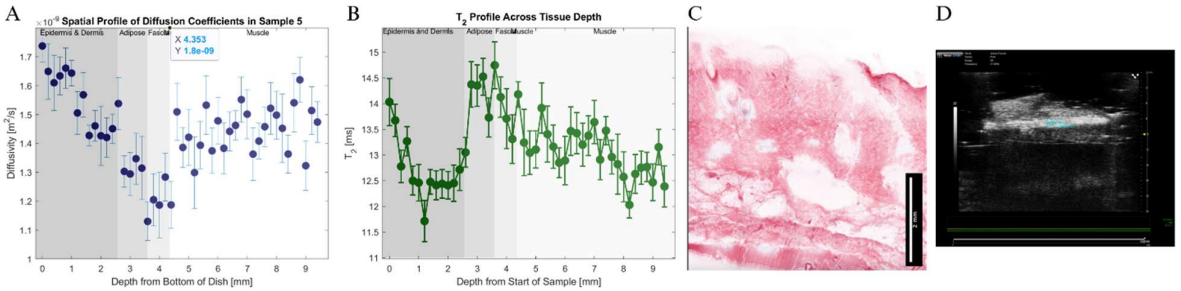

Fig 2: (A) Diffusion coefficients in m^2/s as a function of depth, with the known depth measurements overlayed. (B) T2 graph in seconds versus the depth of sample with the known depths overlay. (C) Example of optical imaging of sample, serving as ground truth. (D) Ultrasound image of sample, showing sample layers.

Conclusion: Single-sided NMR revealed clear, depth-dependent changes in tissue properties. T_1 values decreased at the fascia boundary, while T_2 values dropped within the fascia, reflecting structural shifts. Diffusion coefficients showed a characteristic dip before the fascia and rose within it, indicating a transition zone. In contrast, ultrasound provided poor delineation due to weak contrast between fascia and surrounding fat. These results suggest that relative changes in NMR signals across depth, rather than absolute values alone, offer a promising approach for identifying fascia and assessing its thickness noninvasively.

References:

[1] Langevin, H. (2021). Fascia Mobility, Proprioception, and Myofascial Pain. Life, 11, 668.
[2] Bozic, I., et al. (2024). Quantitative assessment of dyes and protocols for ex vivo microscopy. Sci Rep, 14, 21376.
[3] Blümich, B. (2019). Essential NMR (2nd ed.). Springer.

Book of Abstracts

ICMRM '25

Scientific Session 4

Hardware

Redefining NMR: Portable, Dead-Time–Free, and Chip-Powered

Jens Anders
University of Stuttgart, Stuttgart, Germany

In this invited talk, Jens Anders will present the latest breakthroughs from his group in the rapidly evolving field of chip-assisted NMR. He will showcase the next generation of portable, multi-channel NMR spectrometers that bring high performance into compact, field-deployable formats, as well as dead-time–free NMR detectors powered by innovative voltage-controlled oscillator technology. The talk will also introduce portable, chip-based DNP systems, paving the way for enhanced sensitivity in mobile and resource-limited environments. Together, these advances illustrate how semiconductor technologies are redefining the limits of NMR spectroscopy—bringing laboratory-grade capabilities to the palm of your hand.

MRI using straight wires as spatial encoding coils

I. Serša[1], *K. Tušar*[2]
[1]Jožef Stefan Institute, Ljubljana, Slovenia,
[2]Jožef Stefan International Postgraduate School, Ljubljana, Slovenia

Introduction: In conventional magnetic resonance imaging (MRI), spatial encoding of signals is performed using gradient coils that generate a spatially linearly increasing magnetic field and thus have a constant gradient. However, it has been shown in numerous studies that MRI can also be successfully performed with signal encoding coils that generate nonlinear magnetic fields [1-4]. In this study, we demonstrate that such imaging is possible with an extreme type of such coils, namely, straight wires that generate extremely nonlinear magnetic fields.

Methods: We recently proposed a new method for MRI using nonlinear encoding coils [5] in which the Fourier conjugate pair $\vec{k}$ and $\vec{r}$ is replaced by the pair $\vec{t}$ and $\vec{\omega}$. This change allows the use of the Fourier transform in the transformation of image signals from the time domain to the frequency domain. The obtained spectrum $\hat{S}(\vec{\omega})$ can then be converted into an image $\rho(\vec{r})$ using the relation:

$$\rho(\vec{r}) = \hat{S}(\vec{\omega}(\vec{r}))\left|\frac{\partial\vec{\omega}}{\partial\vec{r}}\right| \qquad \text{Eq. 1}$$

where $\vec{\omega}(\vec{r})$ is the transformation between frequency and spatial coordinates, which is an inherent property of the encoding coils, and $\left|\partial\vec{\omega}/\partial\vec{r}\right|$ is the Jacobian determinant of this transformation. This method was used in reconstruction of images acquired with three different types of simple encoding coils all build from straight wires, as sources of inhomogeneous magnetic field, in different arrangements: 2D nonsymmetric (Fig. 1A), 2D symmetric (Fig. 1B), and 3D nonsymmetric (Fig 1C). Experiments were performed with encoding coils in the *xy* plane at *z* = 0 using a spin-echo imaging sequence on a 2.35 T MRI system. Signal acquisition was performed at a BW 50 kHZ and a FOV 5 cm.

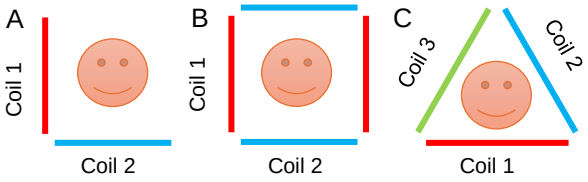

Fig. 1: Schematic of three different tested types of encoding coils arrangements.

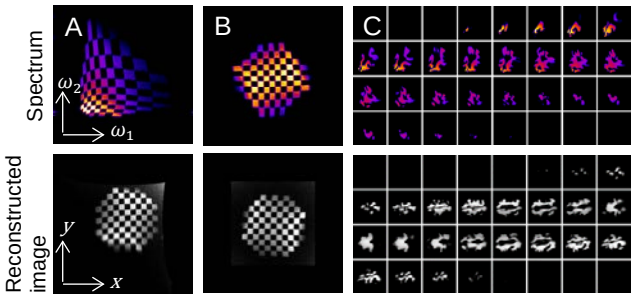

Fig. 2: Spectra and corresponding reconstructed images.

Results and discussion: All tests, i.e., 2D experiments on a checkerboard disc phantom with nonsymmetric (Fig. 2A) and symmetric (Fig. 2B) encoding coils, as well as a 3D simulation performed on a digital image of a walnut and encoding coils implemented with three wires arranged in a triangle (Fig. 2C), yielded reconstructed images that well depict the test phantoms, while their corresponding spectra have geometric and intensity distortions that were corrected in the reconstruction process using Eq. 1.

Conclusion: The results of the study may help advance "gradient" coil design towards freer geometries, higher magnetic field gradients or lower inductance and thus faster switching times.

References: [1] Hennig, MAGMA (2008). [2] Schultz, Magn. Reson. Med. (2010). [3] Stockmann, Magn. Reson. Med. (2010). [4] Wang, Magn. Reson. Med. (2016). [5] Tušar, Sci. Rep. (2024).

Compact NMR tool for underground soil contaminants monitoring

Sihui Luo[1], *Zhihao Long*[1], *Guangzhi Liao*[1], *Huabing Liu*[2], *Tingting Lin*[3], *Lizhi Xiao*[1,*]
China University of Petroleum, Beijing, China
Beijing Limecho Technology Ltd.Co, Beijing, China
Jilin University, Changchun, China

Groundwater is a vital resource for human survival, stored in porous sandy soils at varying depths underground. However, the petroleum hydrocarbon contaminants pose a serious threat to groundwater quality when they infiltrate soil pores, causing persistent pollution. Such contamination disrupts the biological, chemical, and physical properties of soil and endangers organisms in affected ecosystems. Effective remediation is therefore imperative, requiring precise detection and quantification of petroleum hydrocarbons in sandy soils. Accurate identification of contaminant types and concentrations is critical for optimizing remediation strategies.

Nuclear magnetic resonance (NMR) is a promising technique for monitoring soil contaminants and mitigating groundwater pollution. It characterizes fluid dynamics in porous media and provides key hydrological parameters, including total porosity, fluid saturation, and soil properties. Conventional NMR logging tools, however, are often impractical for groundwater and soil moisture measurements due to their bulky size and high cost. To overcome these limitations, compact NMR logging tools with smaller diameters have been developed. Despite progress, most commercial small-diameter NMR tools lack advanced two-dimensional NMR capabilities (e.g., D-T_2 correlation map) because of their low-gradient static magnetic fields—a critical shortcoming for distinguishing complex fluid compositions such as water, oil, and hydrocarbons.

To address these challenges, we developed a compact NMR logging tool (60 mm diameter) based on the NUMAR design for soil contaminant detection. The tool is compatible with PVC or fiberglass-cased boreholes (70 mm diameter) and features a hybrid magnet structure comprising a ferrite main magnet and a samarium-cobalt polarization magnet. The coil structure is optimized using an inverse design method, enhancing circumferential excitation uniformity and ensuring the signal-to-noise ratios. The tool could achieve the performance under operation frequency about 650 kHz and field gradient of about 50 Gs/cm, and also with a depth of investigation of 120 mm (from borehole axis), and a vertical resolution of 300 mm. Laboratory experiments confirm the tool's feasibility for both 1D and 2D NMR measurements, enabling reliable identification of water and hydrocarbon contaminants. Field tests will be conducted in the future work.

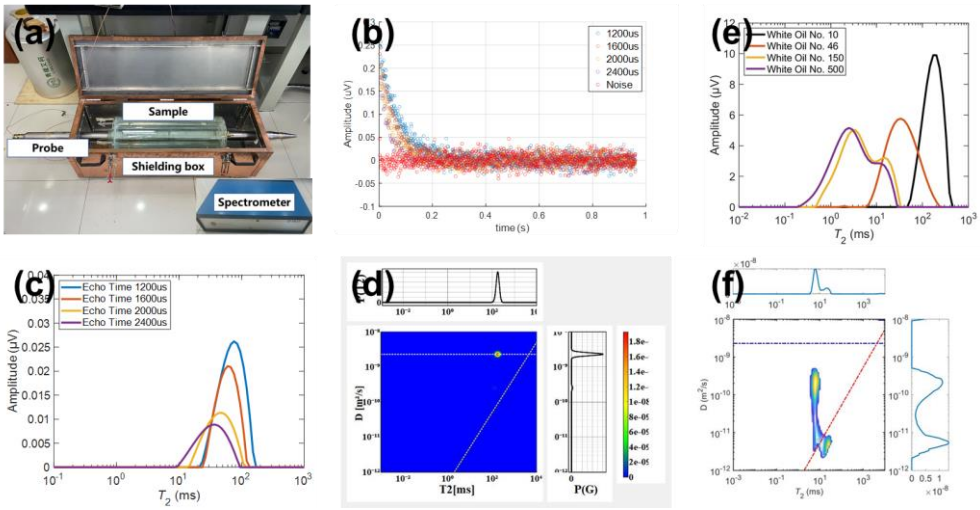

Fig. 1: (a) Compact NMR tool and laboratory experimental condition; (b) Acquired echo train with different echo spacing; (c) T_2 distributions of copper-sulfate solution with different echo spacing; (d) D–T_2 correlation maps of copper-sulfate solution; (e) T_2 distributions of white oil with different viscosities; (f) D–T_2 correlation maps of no. 500 white-oil samples.

References:

[1] Lizhi Xiao. Practical NMR for Oil and Gas Exploration. Royal Society of Chemistry, (2023).
[2] Zhihao Long, Lizhi Xiao, Sihui Luo, Huabing Liu, Xiaoguang Zhao. Inverse design of RF coil for slim nuclear magnetic resonance tool. IEEE Transactions on Instrumentation and measurement, (2024).
[3] Tingting Lin, Yida Wang, Jinshuo Cheng, Yujing Yang. Detecting and quantifying diesel and gasoline contaminants in sandy soil by multivariate analysis based on nuclear magnetic resonance T2 spectrum. IEEE Transactions on Instrumentation and measurement, (2024).

Contact-free MRI and MRS on self-standing droplets

Smaragda-Maria Argyri [1], Leo Svenningsson[1], Feryal Guerroudj[1], Diana Bernin[1], Lars Evenäs [1], Romain Bordes [1]

[1]Chalmers University of Technology, Gothenburg, Sweden

Introduction:

Magnetic resonance spectroscopy and imaging are versatile techniques that provide key information about the structure, dynamics and interactions of molecules. Yet, experimental magnetic resonance studies are often limited to the use of sample holders. Addressing this constraint would allow the implementation of real-time, dynamic studies on the molecular level of liquid samples undergoing for example evaporation, or phase transitions. Previous efforts to study self-standing droplets under a magnetic field have primarily focused on molten aluminum beads *via* aerodynamic levitation[1] or buoyancy forces of immiscible liquids[2]. However, these methods are constrained to non-volatile samples and lack direct access to the interface. Recent advancements have explored magnetic resonance studies on surface-resting sessile droplets, providing real-time dynamic insights[3], yet without endowing a fully contact-free environment.

Methodology and results:

In this study, we utilize a demagnetized acoustic levitator to investigate liquid samples in a contact-free manner. Initially, the performance of the levitator (Fig. 1a) inside a 300 MHz magnetic field was assessed. Then, magnetic resonance images of the levitator and the levitated samples were collected (Fig 1b), which acted as a direct proof-of-concept. Following, resolved NMR spectra of the levitated droplets were collected by applying localized and non-localized pulses. Finally, we examined the impact of the droplet shape on the chemical shift and conducted time-resolved experiments using pure solvents and mixtures, yielding valuable insights into physical and chemical interactions.

Conclusions:

This approach allows the implementation of contact-free, time-resolved studies at the molecular level, advancing the capabilities of magnetic resonance research.

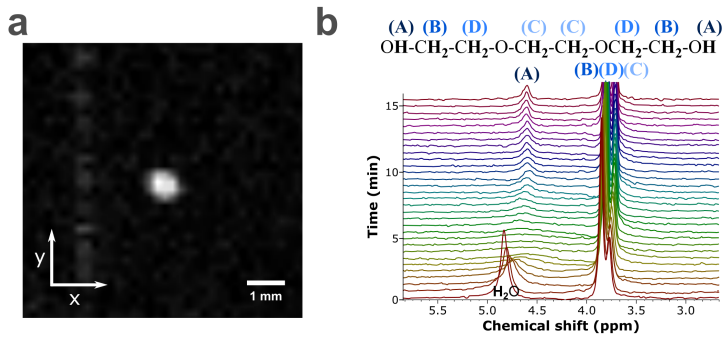

Figure 1. a) MRI of acoustically levitated droplet of hexadecane, recorded with True Fast Imaging with Steady State Precession, with 20x20 mm^2 field of view, 64x64 mm^2 resolution, 1 mm slices, 5 averages, echo time of 1.143 ms, repetition time of 2.287 ms, 21 segments, segment mode sequential, scan repetition time of 35 ms, and flip angle of 90°, and b) Series of NMR spectra of a 50 wt% triethylene glycol aqueous solution during evaporation, recorded with Image-Selected In vivo Spectroscopy by applying a 3000 ms repetition time, 8 scans, on a 5x5x5 mm^3 voxel, and 5 Hz exponential line broadening.

References

[1] Marzke, R. F., Piwowarczyk, J., McMillan, P. & Wolf, G. Al motion rates in levitated, molten Al2O3 samples, measured by pulsed gradient spin echo 27Al NMR. *J. Eur. Ceram. Soc*. **2005**, 25, 1325–1332.

[2] Gross-Hardt, E., Amar, A., Stapf, S., Blümich, B. & Pfennig, A. Flow dynamics measured and simulated inside a single levitated droplet. *Ind. & engineering chemistry research*, **2006**, 45, 416–423.

[3] Kind, J. & Thiele, C. MRI and localised NMR spectroscopy of sessile droplets on hydrophilic, hydrophobic and superhydrophobic surfaces – examination of the chemical composition during evaporation. *J. Magn. Reson.*, **2019**, 307, 106579.

Helium-3 magnetometers for high fields

P. Blümler[1], M. Fertl[1], H.J. Grafe[2], R. Graf[3], and W. Heil[1]

1) Institute of Physics, University of Mainz, Germany
2) Leibniz Institute for Solid State and Materials Research (IFW), 01069 Dresden, Germany
3) MPI for Polymer Research, 55128 Mainz, Germany

While low magnetic fields (< 10^{-2} T) can be measured extremely precisely (ca. 10^{-13}) using SQUID or SERF, nuclear magnetic resonance (NMR) offers the highest precision at high fields. Moreover, the highest metrological accuracy is achieved through continuous measurements of frequencies. This demands a sample with long coherence times, as it is the case for motionally averaged signals of gases. A state that requires only a few millibar of the gas, hence necessitates hyperpolarization of the nuclear spins even at high fields. For this reason, ^{3}He is the ideal candidate due to its ability to be hyperpolarized — either via metastability optical pumping (MEOP) [1] or the PAMP-effect [2]. Furthermore, it shows only minimal interactions with the environment and its gyromagnetic ratio has been determined independently using Penning-traps [3]. Another requirement to obtain such extremely long lasting signals (T_2* times in the order of 100 – 200s) the sample has to be kept in suitable containers to minimize susceptibility effects [4] and allow even for absolute field measurements [5].

While low-pressure and hyperpolarized ^{3}He enables extreme precision magnetometry (< 10^{-12}), we recently also produced high pressure (up to 50 bar) ^{3}He samples for applications in which optical polarization is impractical. Such thermally polarized samples can serve as very simple and robust NMR-magnetometers and may be used over a very broad temperature range (1-300 K). Their production and strategies to adjust T_1 for rapid sampling are presented for a temperature range from 5 to 300 K. [6]

Taken together, ^{3}He-magnetometers have the potential to become the new standard for high precision magnetometry at high magnetic fields.

Reference:

1. A. Nikiel, P. Blümler, W. Heil, et al., The European Physics Journal **D 68**:330, 1-12 (2014).
2. A. Maul, P. Blümler, P.-J. Nacher, et al., Physical Review **A 98**, 063405 (2018).
3. Schneider, A., Sikora, B., Dickopf, S. et al., Nature **606**, 878–883 (2022).
4. A. Maul, P. Blümler, W. Heil, et al., Review Scientific Instruments **87**, 015103, 1-8 (2016).
5. M. Farooq, T. Chupp, J. Grange, et al., Phys. Rev. Lett. **124**, 223001 (2020).
6. P. Blümler, M. Fertl, H.-J. Grafe, et al., https://arxiv.org/html/2501.08936v1.

Nano- and microscale NMR microscopy using NV-centers in diamond

Dominik B. Bucher[1]

[1]Technical University of Munich, Munich, Germany,

Nitrogen vacancy (NV) point defects in diamond have become a promising platform for magnetic resonance microscopy. The electronic spin state of these solid-state spin system can be optically polarised, coherently manipulated with microwave pulses, and read out via their spin-state-dependent photoluminescence. Using the optically detected spin state readout, NMR signals can be detected with unprecedented sensitivity [1]. In the first part of my the talk, I will give a short tutorial on NV-based NMR spectroscopy. In the second part, I will give an overview over our recent work on spatially resolved NV-NMR: 1) Nanoscale NV-NMR to detect monolayers of self-assembled molecules on an alumina oxide surface and their formation in real time under chemically relevant conditions [2]. 2) Combination of pulsed field gradient spin echo (PGSE) experiments with NV-NMR to quantify molecular diffusion and mobility within microstructures [3]. 3) Wide-field optical NMR microscopy on a camera [4]. This technique allows magnetic resonance imaging in real space on microscopic length scales. The remaining obstacles to this novel technologies and future goals are discussed in the final part.

References: [1] Allert, Chem Comm (2022). [2] Liu, PNAS (2022). [3] Bruckmaier, Science Advances (2023). [4] Briegel, Nature Communications (2025)

Book of Abstracts

ICMRM '25

Scientific Session 5

Porous Media & Low Field

Topology Optimization Method for Nuclear Magnetic Resonance Logging tool Magnetic and Soft magnetic Design

Qiao Zhen[a,b], Luo Sihui [a.b], Xiao Lizhi[a,b], Liao Guangzhi[a,b]

[1] Key Laboratory of Petroleum Resources and Engineering, China University of Petroleum, Beijing, China; [2]China University of Petroleum, Beijing 102249, China;

Introduction： Nuclear magnetic resonance logging is an important part of petroleum exploration, and the design of the NMR probe magnet, antenna, and soft magnetic material is related to the accuracy of downhole reservoir detection. Traditional probe design is often based on empirical structures, which reduces the accuracy of matching the probe magnet and antenna, increases the cost of manual optimization (time and effort).

Methods： This study uses the Finite Element Method to effectively solve the B_0 and B_1 magnetic fields . In order to optimize the antenna and magnetic field at the same time, two magnetic fields are set and the design variables are derived separately by the chain rule:

$$\int\int_{\Omega} V(\frac{\partial A_Z}{\partial_X}\frac{\partial A_Z}{\partial_X}+\frac{\partial A_Z}{\partial_X}\frac{\partial A_Z}{\partial_X})dxdy=\int\int_{\Omega} V(\frac{\partial A_Z}{\partial_X}\frac{\partial A_Z}{\partial_X}+\frac{\partial A_Z}{\partial_X}\frac{\partial A_Z}{\partial_X})dxdy+\int\int_{\Omega} J_Z N dxdy$$

N is the basis function, and A_Z is the magnetic vector potential.

We have divided the construction of magnets, antennas, soft magnetics, topology optimization and air domain into separate parts. The objective function, point distribution and constraints are as follows:

$Find$： $\rho=(\rho_1,\rho_2,\rho_N)$

$Maximize$： $\phi=\sum_{i=1}^{100} B_{0,\ i}^2 \bullet(\mathrm{B}_{1m}/\mathrm{I})$

$Subject\ to$: $0\le\rho_e\le 1$

The density interpolation model of SIMP interpolation function is used for density interpolation. The finite element material interpolation function is:

$$\mu(\rho_e)=\mu_0+\theta_p\bullet(\mu_i\bullet\mu_0-\mu_0)$$

μ_0 is the magnetic permeability of air, and μ_i is the permeability of soft magnetic material.

The model is iteratively solved using the moving asymptote method (MMA) based on gradient descent.

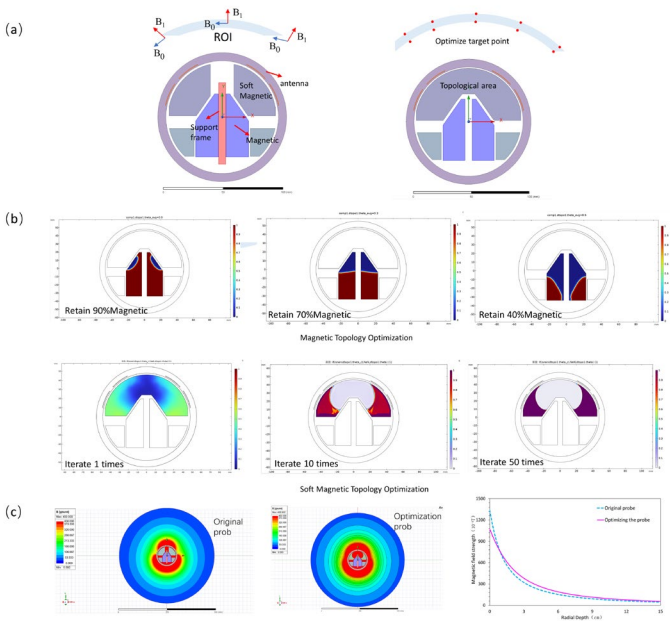

Fig. 1: (a) illustrates the optimization objective and the optimization domain. (b) shows the topology-based optimization of the magnet and the soft magnetic material. (c) presents the optimization results.

Results and discussion： The magnet volume is reduced by 10%, 30%, and 60%, the resulting magnetic field strength decreases accordingly. To generate the maximum magnetic field, the entire magnet volume is selected as the primary magnet. The soft magnetic material, after topology optimization, exhibits a horn-shaped structure. The sensitive region is located 5–7 cm outside the magnet. and it can generate a static magnetic field with an intensity of 114.6 ~ 157.8G and a gradient of 273.0 ~165 G/cm in the distal ROI as illustrated in **fig（c）**.

References: [1] Gregor, Sci. Rep. （2022）.
[2] Deaton, Struct Multidiscip O. (2014).

Fluid quantitative evaluation method of two-dimensional NMR logging

A. Li Chenglin[1], B. Tan Maojin[1]
[1]China University of Geosciences Beijing, Beijing, China

Introduction: The nuclear magnetic resonance (NMR) logging technology is widely used in the interpretation and evaluation of reservoirs. When the signal-to-noise ratio (SNR) of the echo data measured on-site of NMR logging is low, the response of the fluid component overlaps in the NMR 2D spectrum [1][2]. The blind source separation (BSS) method is to separate or recover the original source signals from the received mixed signals without knowing the source signals and the mixing parameters, and this method can be used to obtain the 2D spectra of several common fluid components of NMR logging data [3][4][5]. But a single spectrum extracted by BSS method from logging data always contains characteristics of multiple components. Therefore, we proposed a method combining BSS and the hierarchical clustering algorithms. Each 2D spectrum obtained by this method only contains one fluid component by further separation. The fluid types are determined, and the fluid volumes are quantitatively calculated for reservoir evaluation.

Methods: Assuming there are *r* fluid components in a certain stratum, T2-T1 2D spectra of m depth points are collected. The sample number in the 2D spectra is $n = n_1 \times n_2$, where n_1 and n_2 are the sample number of T2 and T1, separately. Let the 2D NMR spectra of the fluid components be $\boldsymbol{S}r\times n$, the collected data be $\boldsymbol{X}m\times n$, and there is a mixing matrix $\boldsymbol{A}m\times r$:

$$\boldsymbol{X}_{m\times n} = \boldsymbol{A}_{m\times r} \cdot \boldsymbol{S}_{r\times n} \quad \text{Eq. 1}$$

The update iteration formulas of the mixed matrix $\boldsymbol{A}$ and the source signal matrix $\boldsymbol{S}$ obtained by the Non-negative Matrix Factorization (NMF) algorithm are as follows:

$$\frac{(XS^T)_{ik}}{(ASS^T)_{ik}} A_{ik} \rightarrow A_{ik}, \frac{(A^TX)_{kj}}{(A^TAS)_{kj}} S_{kj} \rightarrow S_{kj} \quad \text{Eq. 2}$$

Results and discussion: Well A is mainly shale reservoirs, and its 2D NMR logging data are acquired by Schlumberger instrument. The processing results of the spectra of the depth 3470-3610m are shown in Fig. 1, including 8 spectra with a single fluid characteristic, and 6 fluid types are identified. The calculated oil volume (Bound oil and free oil) is compared with the result of pyrolysis experiment, and the former is consistent with the later.

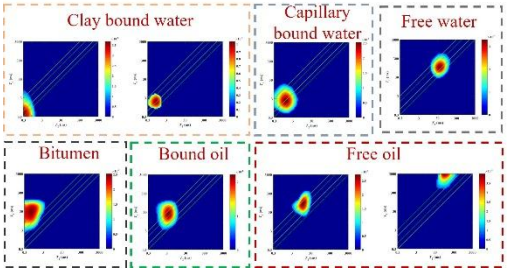

Fig. 1: Separated results by the proposed method

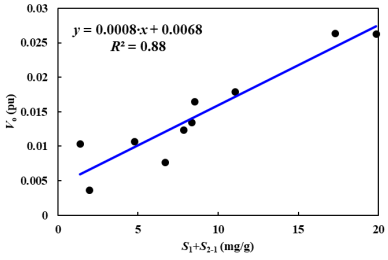

Fig. 2: Cross-plot of experiment and calculated results

Conclusion: A fluid quantitative evaluation method of 2D NMR logging, which could extract the spectra with a single fluid characteristic, was proposed by combining the BSS and hierarchical clustering algorithms. The processing results of well A are consistent with the pyrolysis experiment, indicating that this method is accurate and effective.

References: [1] Coffey, IEEE GRSL. (2019). [2] Fleury, J. Magn. Reson. (2013). [3] Jiang, Comput. Geosci. (2019). [4] Gu, J. Magn. Reson. (2021). [5] Venkataramanan, Petrophysics, (2018).

Velocity Measurement in Porous Media Using Steady-State Free Precession

M.S. Zamiri[a], D. Green[b], B. Nicot[c], L. Li[d],B.J. Balcom[a]
[1]UNB MRI Centre, Department of Physics, UNB, Fredericton, NB E3B 5A3, Canada
[2]Green Imaging, 520 Brookside Drive, Fredericton, New Brunswick, E3A 8V2, Canada
[3]TotalEnergies, Avenue Larribau, 64000 Pau, France
[4]Functional MRI Facility, National Institutes of Health, Bethesda, MD, USA

Introduction: Velocity measurements in porous media have important applications in petroleum systems, perfusion in biological tissues, drug delivery, and nutrient transport in plants. Pulsed field gradient techniques are commonly used for velocity measurements [1]. Steady-State Free Precession (SSFP) produces a periodic magnetization pattern [2] that is sensitive to flow [3]. This flow sensitivity, first reported in 1986 [4], arises from the distortion of the magnetization pattern under steady flow, leading to the formation of a new steady state [5].

Methods: This distortion was modeled using the Bloch-Torrey equations. We solved these equations analytically using Fourier series decomposition to predict the alteration of the steady-state response under steady flow conditions. To validate the model, steady brine flow was established through a Bentheimer sandstone core plug using a high-precision Pharmacia pump.

Results and discussion: As demonstrated both theoretically and experimentally in this study, SSFP measurements under steady flow conditions produce a periodic steady-state magnetization that exhibits strong flow sensitivity. This sensitivity manifests as signal attenuation in the longitudinal magnetization and as a systematic phase shift in the transverse magnetization, as shown in Fig. 1. The steady-state longitudinal magnetization and the phase of the transverse magnetization were simultaneously fit to the analytical solution, enabling quantitative velocity measurement.

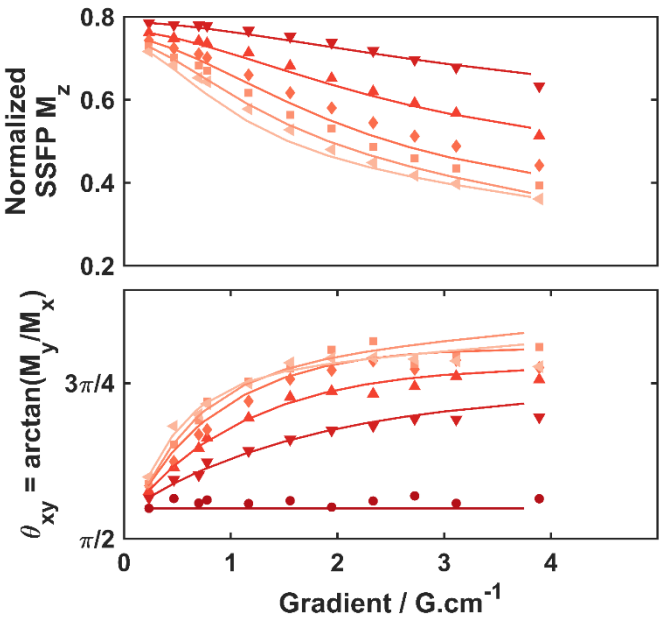

Fig. 1: (a) Measured steady-state longitudinal magnetization normalized to the no-flow case, and (b) phase of the transverse magnetization at the steady-state versus gradient in the direction of mean pore velocity of 0 (●), 105 (▼), 210 (▲), 315 (♦), 420 (■), and 526 (◀) µm/s in a Bentheimer sandstone. Solid lines are the result of the analytical solution fitting the experimental data.

Conclusions: The SSFP technique was employed to obtain quantitative velocity measurements in porous media. This method has been adapted for imaging using a preparation-readout strategy. In addition to local velocity measurement, this method offers valuable insights into fluid dynamics within porous structures.

References:
[1] J. D. Seymour and P. T. Callaghan, AIChE Journal 43, 2096 (1997). [2] H. Y. Carr, Phys. Rev. 112, 1693 (1958). [3] L. Li, K. Miller, et al., Magn. Reson. Med. 68, 1423 (2012). [4] S. Patz et al., Magn. Reson. Med. 3, 140 (1986). [5] R. B. V. Azeredo, M. Engelsberg, and L. A. Colnago, Phys. Rev. E 64, 016309 (2001).

Magnetic Resonance Studies of Adsorption Phenomena

M.L. Johns[1], N. Robinson[1], K, Yang[1]
School of Engineering, University of Western Australia, Perth, WA, Australia

Fluid adsorption using porous media provides a critical underpinning process for numerous separation and reaction operations within Chemical Engineering. Here we will demonstrate the ability of NMR to provide unique, non-invasive insights into adsorption phenomena using the following case studies:

(1) The application of low-field (12.7 MHz) ^{1}H nuclear magnetic resonance (LF-NMR) relaxation measurements to non-invasively characterize ethane dynamics and adsorption within various mesoporous silica materials (exhibiting mean pore diameters between 6 and 50 nm) will be demonstrated [1]. Our measurements provide NMR-based adsorption isotherms within the pressure range 25-50 bar, which incorporates the ethane condensation point (40.7 bar at our experimental temperature of 23.6 °C). The quantitative nature of the acquired data is validated via a direct comparison of NMR-derived excess adsorption capacities with *ex situ* gravimetric ethane adsorption measurements, which are demonstrated to agree to within 0.2 mmol/g of the observed ethane capacity. NMR T_2 relaxation time distributions are further demonstrated as a means to decouple interparticle and mesopore dominated adsorption phenomena, with unexpectedly rapid NMR relaxation values associated with interparticle ethane gas, as confirmed via a direct comparison with NMR self-diffusion analysis.

(2) Quantification of methane content in shales is a critical parameter for estimation of their potential gas production capacity. Traditional gravimetric methods for estimation of this quantity are sensitive only to adsorbed methane and are difficult to apply either to intact shale rock cores or via field measurements. Here non-invasive low-field nuclear magnetic resonance (LF-NMR) is applied to quantify excess methane adsorption capacity in intact shale rock plugs at pressures up to 200 bar; validation is provided against destructive gravimetric methods performed on fragments from the same shale rock plugs [2]. The resultant NMR transverse relaxation time (T_2) distributions contain three distinct peaks (referred to as peaks P1 - P3) which are allocated to adsorbed methane in organic pores, methane constrained to inorganic pores and bulk methane located predominately in fractures respectively. The most accurate estimate of excess methane adsorption capacity is obtained via a combination of an overall system mass balance and the methane located in inorganic pores and fractures (peaks P2 and P3, respectively), where excellent agreement is produced with corresponding destructive gravimetric measurements for the various shale samples studied.

(3) The ability of low-field NMR multi-dimensional relaxometry to distinguish functional group-specific relaxation [3], as a consequence of molecular orientation and binding during adsorption, for a range of alcohols and acids in both mesoporous silica and various metal oxide porous media will be briefly elucidated. Potential applications in adsorption science of this measurement approach will be discussed.

References:

[1] Yang, K. et al. ChemPhysChem, 23(4), (2022). [2] Yang, K. et al. Jnl Natural Gas Sci. and Eng. 108(104847), (2022).
[3] Robinson, N. et al. Magnetic Resonance Letters 3(3), 248 (2023); Dong, S. et al. Langmuir, 40(31), 16160 (2024).

Phase separation of miscible fluids in mesoporous media monitored by q space microscopy and relaxometry

N. Siebert[a], C. Mattea[a], A. Sara[b], P. Merle[b], C. Dreßler[b], S. Stapf[a]
[a]Dept of Technical Physics II, TU Ilmenau, Germany
[b]Dept of Theoretical Physics III, TU Ilmenau, Germany

Introduction: The distribution of mixtures of fluids in geometric confinement is affected by the differential interaction of the individual components with the interface. Radial density functions of the molecular distribution reveal that, depending on fluid combinations, density variations occur from between one to several molecular diameters away from the surface. Overall molecular dynamics must therefore become significantly affected if the pore sizes do not exceed dimensions of several nm. Important factors that affect the molecular distribution are firstly polarity of the surface and the molecule, furthermore molecular shape, proticity and charge distribution. In order to experimentally verify the molecular distributions in mesopores, neutron scattering and in particular NMR represent suitable approaches: deviations of molecular locations from their bulk behavior affect both the NMR spectral features and the relaxation properties, whereas translational motion both on a micro- and macroscopic scale enter into the diffusion behavior. Q space studies of transport properties as a function of encoding time are the preferred approach to visualize the equilibrium distribution of liquids in the pore space and to quantify their long-range mobility.

Methods: Binary mixtures of liquids were prepared with one component perdeuterated, and were filled into Vycor porous glass as well as several types of silica gels. Samples included acetone/cyclohexane, THF/cyclohexane and acetone/water which are all fully miscible in the bulk. Relaxation times T_1 and T_2 of ^1H as well as ^2H were determined for a range of Larmor frequencies between 1 kHz and 300 MHz, employing field-cycling relaxometry for the majority of studies. Diffusion coefficients as a function of encoding time were determined by PFG methods on 1T and 7T scanners. For selected fluid combinations, MD simulations were carried out for equivalent cylindrical silica pores, from which radial density profiles and diffusion coefficients were computed.

Results and Discussion: For acetone/cyclohexane, a pronounced reduction of the apparent tortuosity – the ratio of bulk to confined diffusivity – was found in acetone but was absent in cyclohexane [1,2]. Similar observations were made for water and acetone, suggesting a trend of surface affinity in the order water>acetone>cyclohexane. Very long NMR relaxation times confirm that cyclohexane is removed from the silica surface unless it constitutes the only phase present [3]; the effect is apparent but less absolute for water/acetone. MD radial density profiles clearly confirm the preferred adsorption of the more polar liquid. At very low acetone concentration in the mixture with cyclohexane, we found evidence for a reduction of D of 1-2 orders of magnitude, suggesting that the acetone phase close to the surface falls beyond the percolation threshold and forms islands.

Conclusion: Interaction of polar molecules with the solid polar silica surface and its hydroxyl groups leads to concentration gradients in confined liquid mixtures, possibly up to semi-stable layering of certain combinations of fluids that are otherwise fully miscible. Q space microscopy in combination with relaxation studies reveals hints towards full demixing, although local molecular exchange on scales of nm still exists. Experiments are in agreement with MD simulations on short time scales below microseconds, whereas longer times are currently only accessible by PFG experiments.

References: [1] S. Stapf *et al.,* Magn. Reson. Lett. **3**, 108 (2023), [2] R. Kimmich *et al*., Magn. Reson. Imaging 14, 793 (1996), [3] J. Ward-Williams *et al*., Magn. Reson. Imaging 56, 57 (2019),

pH controlled modification of metal oxide surfaces in mine tailings measured by low field ^{1}H NMR relaxometry

C. I. Karunarathne[1], R. Wilkinson[1], M. L. Johns[1], E. O. Fridjonsson[1]

[1]School of Engineering, Department of Chemical Engineering, The University of Western Australia, Crawley, Australia

Abstract

Porous media are prevalent in both natural formations and engineered systems, playing a key role in processes such as mineral carbonation and groundwater flow. However, understanding the physiochemical interactions within their complex pore networks remains challenging. Nuclear Magnetic Resonance (NMR) techniques, particularly, transverse relaxation time (T_2) measurements offer a powerful, non-invasive means of inferring pore-scale behaviour [1]. These measurements are highly sensitive to factors such as surface chemistry, mineral deposition and magnetic susceptibility. In systems containing iron oxides, these effects are even more pronounced due to the paramagnetic nature of Fe^{3+}. Additionally, surface charge, and thus surface relaxivity is influenced by pH, electrolyte concentration, and the isoelectric point (IEP) of the mineral surface. This study investigates how NMR T_2 relaxation of hematite-containing porous media responds to changes in pH and electrolyte concentrations, using a low-field rock core analyser. A stepwise increase in NMR T_2 relaxation time was observed when mine tailings were mixed with $MgCl_2$, attributed to acidification and the presence of sufficient divalent cations. The results imply that selective adsorption of divalent cations can shift the IEP of mineral surfaces to higher pH values [2], leading to significant shifts in NMR T_2 relaxation. To isolate these effects, a model system of borosilicate glass beads and hematite was used, where a threefold increase in T_2 was observed regardless of whether the porous media was exposed to acidic or basic solutions. These findings suggest that under acidic conditions, the formation of amorphous hydroxyl groups reduces surface relaxivity, while under basic conditions, FeOOH formation increases surface relaxivity [3]. This study highlights the importance of identifying IEP in systems with sufficient magnetic susceptibility and emphasizes the need for continuous pH monitoring for accurate interpretation of NMR results.

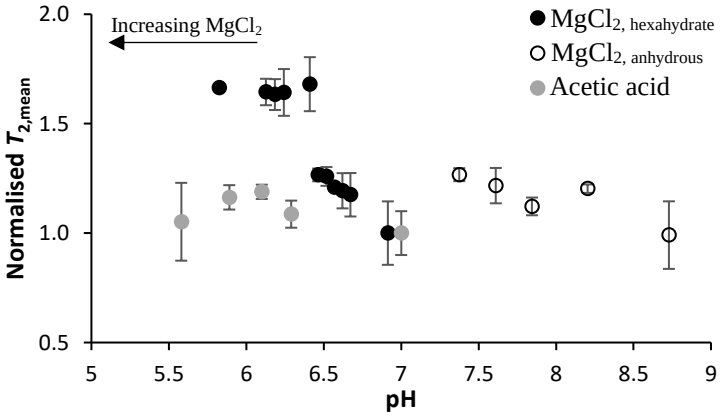

Fig. 1: Normalised $T_{2,mean}$ as a function of pH for tailings mixed with $MgCl_{2,hexahydate}$, $MgCl_{2,anhydrous}$ and acetic acid solutions. Concentration of $MgCl_2$ ranges from 0.5M to 2.5M.

References: [1] Robinson et al., Phys. Rev. Lett. (2023). [2] Kosmulski, Adv. Colloid Interface Sci. (2016). [3] Parks, Chem. Rev. (1965).

Magnetic Resonance and Magnetic Resonance Imaging with a Variable Field Cryogen Free Superconducting Magnet

Bruce J. Balcom[1]

[1]Department of Physics, University of New Brunswick, Fredericton, Canada

Introduction: Magnetic Resonance of realistic materials and processes is often confounded by magnetic susceptibility mismatch effects which dramatically increase the MR linewidth. These magnetic susceptibility effects scale with the strength of the applied Bo field and these effects can be dramatic in porous materials, which comprise the majority of the systems we study.

Control of Susceptibility Effects: In an amenable material one wishes a high field strength for increased SNR, in a more challenging material with a strong susceptibility mismatch, a lower Bo field is essential. How to bridge this divide? For several years we have been employing a cryogen free magnet with an integrated magnet power supply which permits us to increase or decrease the static field as desired, controlling linewidth and susceptibility effects for relaxation and imaging studies. Essentially, we choose the highest available field consistent with the sample and measurement we wish to undertake.

Changing the Nucleus: There is however another, more profound, advantage of the variable field magnet approach to materials MR/MRI. If we are studying a system with a complicated apparatus (for example a battery or a system at high temperature and pressure) there is no reasonable prospect of a multi resonant RF probe for multi nuclear studies. Our approach to measuring nuclei in addition to 1H is to change the static field strength to compensate for a lower gyromagnetic ratio. The result is a constant Larmor frequency and a single RF probe with identical sensitivity and tuning despite a change of nucleus. For example, at 0.79 T the 1H frequency is 33 MHz. If the field is increased to 2.99 T we measure 23Na at 33 MHz and if we increase the field to 3.1 Tesla we measure 13C at 33 MHz. This approach to MR/MRI of materials with multiple nuclei opens many new possibilities for experimentation.

Examples: In this presentation we will outline measurements where we adjust the field to control susceptibility mismatch effects. We will also describe measurements in systems where we adopt the field changing approach to undertake 19F, 13C, 23Na and 7Li studies in conjunction with 1H.

Book of Abstracts

ICMRM '25

Scientific Session 6

Magnetic Particle Imaging & Spectroscopy

Relaxation-Based Color Magnetic Particle Imaging for Functional Imaging

Emine Ulku Saritas[a,b]

[a]Department of Electrical & Electronics Engineering, Bilkent University, Ankara, Türkiye
[b]National Magnetic Resonance Research Center (UMRAM), Bilkent University, Ankara, Türkiye

Magnetic Particle Imaging (MPI) images the spatial distribution and concentration of magnetic nanoparticles (MNPs) by detecting their response to time-varying magnetic fields in the kilohertz range [1]. Due to Brownian and Néel relaxation dynamics, MNP magnetization does not align instantaneously with the applied drive field, resulting in a delayed response. These relaxation mechanisms are sensitive to both the intrinsic properties of the MNPs and their local environment, including factors such as temperature and viscosity. This sensitivity is encoded in the MPI signal and forms the basis for "color MPI" techniques, equipping MPI with additional capabilities such as temperature mapping, viscosity mapping, detection of MNP binding states, and differentiation of MNP types [2-5]. Furthermore, the sensitivity of the MPI signal to these properties can be tuned by adjusting the drive field properties [6] or by applying additional magnetic fields [7-8]. The functional imaging capabilities of color MPI offer promising applications in disease diagnosis (e.g., cancer, atherosclerosis), temperature monitoring during magnetic hyperthermia therapy, and point-of-care diagnostics.

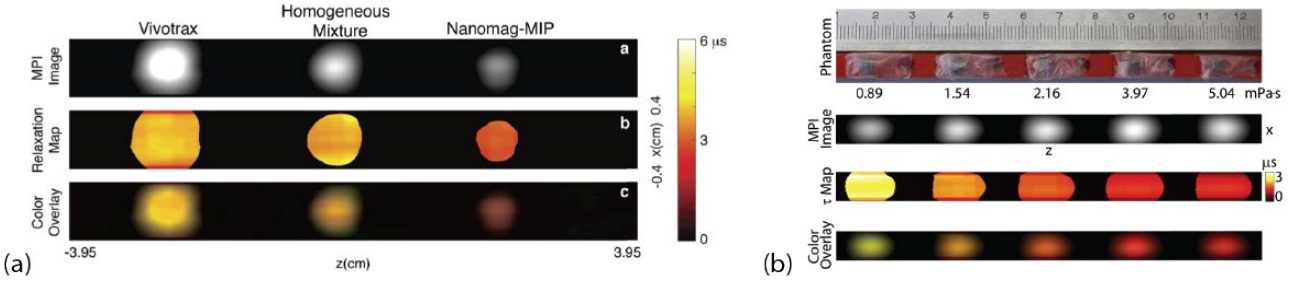

Fig. 1: Color MPI takes advantage of the differences in the magnetization and relaxation properties of MNPs, enabling a variety of functional imaging applications. The examples shown here are for (a) distinguishing different magnetic nanoparticle (MNP) and (b) viscosity mapping. Figures are from [4] and [5].

References:

[1] B. Gleich and J. Weizenecker, Nature 435, 1214–1217 (2005).
[2] J. Rahmer, A. Halkola, B. Gleich, I. Schmale, and J. Borgert, Phys Med Biol, 60:1775–1791 (2015).
[3] C. Stehning, B. Gleich, B. Gleich, and J. Rahmer, Int J Magn Part Imaging, 2:1-6 (2016).
[4] Y. Muslu, M. Utkur, O. B. Demirel, and E. U. Saritas, IEEE TMI, 37:1920–1931 (2018).
[5] M. Utkur, Y. Muslu, and E. U. Saritas, Appl Phys Lett, 115: 152403 (2019).
[6] M. Utkur and E. U. Saritas, Med Phys, 49:2590–2601 (2022).
[7] P. Vogel, M. A. Rückert, B. Friedrich, R. Tietze, S. Lyer, T. Kampf, T. Hennig, L. Dölken, C. Alexiou, and V. C. Behr, Nat Commun, 13:7230 (2022).
[8] A. Topcu, A. Alpman, M. Utkur, and E. U. Saritas, Appl Phys Lett, 125:242405 (2024).

Spatial regularization in 2D multi-color magnetic particle imaging

F. Schrank[1] *and V. Schulz*[1]
[1]Institute of Imaging and Computer Vision, RWTH Aachen University, Aachen, Germany

Introduction: Multi-color magnetic particle imaging (MPI) enables the differentiation between multiple types of magnetic nanoparticles from one measurement. However, the common reconstruction approach using two or more system matrices (SMs) to map the particle signal to different image channels [1] often results in channel leakage artefacts [2].

Methods: Inspired by the critical offset points leveraged in COMPASS to distinguish bound from unbound nanoparticles [3], we propose to find spatial regions in the SM frequency components where the phase varies significantly between the SMs of different particle types. These regions are then masked and used as a spatial regularization during the common multi-channel Kaczmarz reconstruction [1]. Specifically, we extend the row-based algorithm that iterates over all frequency components, by multiplying each update with the correponding regularization mask for this frequency component to enforce that the regions that differ significantly in phase in the two SMs have the highest importance.

Results and Discussion: In Fig. 1, some phase profiles of two SMs acquired with different types of particles, namely perimag (micromod Partikeltechnologie GmbH, Rostock, Germany) and SHP25 (Ocean NanoTech, San Diego, US), can be seen. Furthermore, the figure shows the absolute difference between the phase profiles and the regularization mask that was created by setting all values in the difference map below 0.5 to 0 and above 0.5 to 1. To test the algorithm, we simulated a measurement of two phantoms, each containing one particle type (Fig. 2, left). For reconstruction, the 200 frequency components with the highest SNR are selected for both SMs, and the algorithm is run for one iteration. The standard Kaczmarz regularization value was set individually for the two algorithms to achieve the best visual results. The middle column of Fig. 2 shows the standard Kaczmarz reconstruction, where the leakage of the SHP25 signal is clearly visible (green box). With our spatial regularization approach, this is prevented. However, our reconstructions are noisier and have more artefacts towards the edge of the field-of-view. The SHP25 channel is generally much noisier due to significantly lower signal of the SHP25 particles compared to perimag.

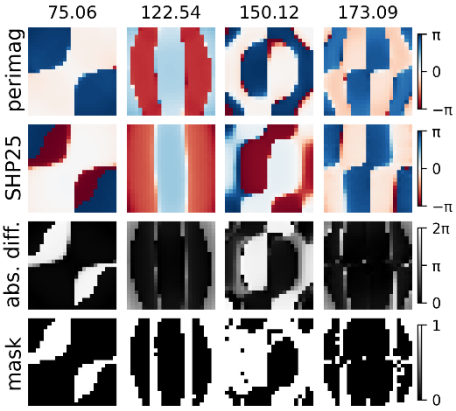

Fig. 1: From top to bottom: Phase of four SM frequency components (frequencies given above in kHz) for perimag and SHP25, absolute difference of the phase and regularization mask.

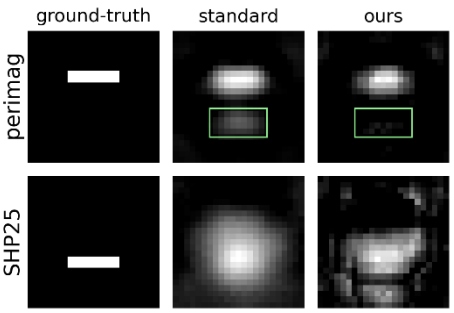

Fig. 2: Ground-truth phantoms and reconstruction result for the perimag (top) and SHP25 (bottom) channel using the standard Kaczmarz algorithm and our extension.

Conclusion: In conclusion, we proposed a spatial regularization approach for multi-color MPI which can prevent channel leakage artefacts. However, further testing and refinement of the method is necessary.

References: [1] Rahmer, Phys. Med. Biol. (2015). [2] Nawwas, Phys. Med. Biol. (2024). [3] Vogel, Nat Commun (2022).

Spatial Receive Sensitivity Assessment using MPI Transfer Function Measurements

F. Thieben[a,b], S. Reiss[a,b], J. Faltinath[a,b], M. Boberg[a,b], and T. Knopp[a,b,c]

[a]Institute for Biomedical Imaging, Hamburg University of Technology, Hamburg, Germany, [b]Section for Biomedical Imaging, University Medical Center Hamburg-Eppendorf, Hamburg, Germany, [c]Fraunhofer Research Institution for Individualized and Cell-Based Medical Engineering IMTE, Lübeck, Germany

Abstract: Upscaling Magnetic Particle Imaging (MPI) to human scale introduces regions of interest within the coil where sensitivity inhomogeneities arise. These inhomogeneities affect both image reconstruction quality and model-based system matrices. In this work, we present an approach for measuring these inhomogeneities using only a few spatial MPI transfer function measurements.

Introduction: The field-of-view (FOV) in receive coils of human-sized MPI systems [1] extends beyond the homogeneous region, with conductive material potentially distorting the sensitivity profile. Accurate coil sensitivity information is crucial for enhancing image reconstruction, especially when using model-based system matrices. Extending MPI receive path calibration from the coil center [2] to all spatial positions using smart sampling methods [3], the field profile can be assessed.

Methods: For the dedicated gradiometric receive coil of the aforementioned MPI system [1], the transfer function $\widehat{\boldsymbol{S}}_{21,\mathrm{in,cal}}$, from the input of 3D calibration coil to MPI systems analog signal input, was measured at 86 positions arranged on a spherical t-design [3]. Using solid harmonic expansions, the field profile can be determined by

$$\mathbf{P}_{\mathrm{rx}}(\boldsymbol{r}) \propto \widehat{\mathbf{G}}(\boldsymbol{r},k) = \widehat{\mathbf{G}}(\boldsymbol{r}_0,k)\mathbf{P}_{\mathrm{rx}}(\boldsymbol{r}_0)^{+}\mathbf{P}_{\mathrm{rx}}(\boldsymbol{r}) \approx \left(\frac{R}{NA}\right)\widehat{\boldsymbol{S}}_{21,\mathrm{in,cal}}(\boldsymbol{r},k) \propto \widehat{\boldsymbol{S}}_{21,\mathrm{in,cal}}(\boldsymbol{r},k), \quad \text{Eq. 1}$$

Where, $\mathbf{P}_{\mathrm{rx}}$ is the coil sensitivity, $\widehat{\mathbf{G}}$ is the MPI transfer function, $\boldsymbol{r}_0$is the coil center, R is the coil resistance, N is the number of turns, and A is the coil surface area. To measure the transfer function, a 3D calibration coil, with 10 turns in each direction and a coil radius of 2.5 mm, was moved to each of the 86 positions. The output of the network analyzer (DG8SAQ VNWA3, SDR-Kits, U.K.) was sequentially connected to each spatial direction of the 3D calibration coil, and the transmission signal at the end of each receive chain was recorded. To preserve the magneto-quasistatic approximations, the spatial position should only scale the transfer function's amplitude, not its phase. Once this condition is met, a single frequency component with sufficient signal can be used to determine the field profile.

Results and discussion: In Fig. 1, the field profile in form of a single transfer function index $|\widehat{\boldsymbol{S}}_{21,\mathrm{in,cal}}| = \left[\mathrm{sgn}(\cos(\arg(\hat{S}_{21,\mathrm{in,cal},i}))) \cdot |\hat{S}_{21,\mathrm{in,cal},i}| \text{ for } i = \mathrm{x,y,z}\right]$ of the gradiometric receive coil of a human-sized MPI system is shown [1]. Spatial field orientation and homogeneities become prominent. Due to feedthrough cancellation with more cancellation turns than receive turns a sensitivity field-free-point is found in the FOV.

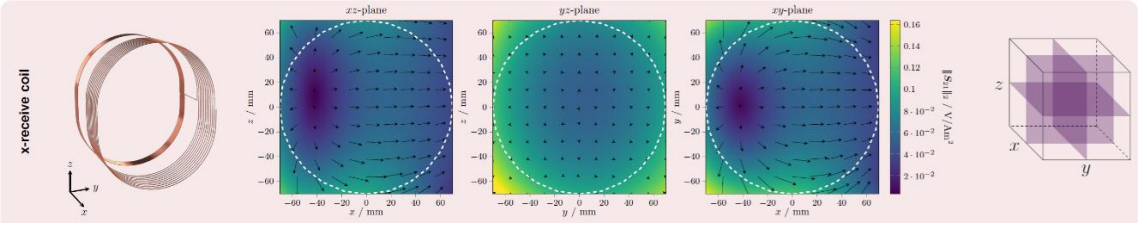

Fig. 1: Measured field profile for a dedicated receive coil. A rendering of the receive coil is shown with the measured corresponding transfer function profile of one frequency component. The dashed white circle indicates the edge of the sphere. On the right, the respective planes are illustrated.

Conclusion: The presented measurement-based method enables the assessment of spatial receive coil sensitivities. In addition to enhancing image reconstruction, it provides a foundation for the iterative improvement of receive coil design.

References: [1] Thieben et al. , IEEE TIM. (2023) doi: 10.1109/TIM.2022.3219461. [2] Thieben et al. , Commun. Eng.Phys. (2024) doi: 10.1038/s44172-024-00192-6. [3] Boberg et al. EJAM (2024), doi: 10.1017/S0956792524000883.

Next-Generation Single-Sided MPI Scanner – Towards Clinical Applications

C. McDonough[1], J. Chrisekos[2], and A. Tonyushkin[1]
[1]Physics Department, Oakland University, Rochester, MI, USA, [2]Electrical and Computer Engineering Department, Oakland University, Rochester, MI, USA

Introduction: Magnetic Particle Imaging (MPI) is a tracer-based imaging modality that enables high-contrast, radiation-free imaging of superparamagnetic iron oxide nanoparticles (SPIO) [1]. Traditional MPI scanner designs, particularly closed-bore topologies, limit access and subject size, restricting clinical applications. Single-sided MPI scanners [2] eliminate these constraints by enabling open-access imaging that is not restricted by subject dimensions, making them ideal for clinical translation [3]. In this work, we present the next generation of a field-free line (FFL) single-sided MPI scanner [4]. The upgrades highlight the potential of the scanner to significantly improve sensitivity, field of view, and image quality, making it a viable candidate for clinical diagnostics.

Methods: The MPI scanner (Fig.1a) is composed of five electromagnetic coils, three of which are "racetrack" shaped selection coils responsible for generating the FFL and defining its trajectory for spatial encoding. The top coils contain a receive gradiometer and a replaceable organ-specific excitation coil. We utilized various phantoms with SPIO tracer to test imaging and characterize the performance of our scanner. To evaluate the field of view (FOV), we imaged a spiral phantom in the coronal plane. The scan used an 8 cm FOV, a 0.4 T/m gradient, and a 1 mm FFL scan step. Spatial resolution was assessed using a two-rod phantom (25 mm long with a 1 mm diameter, separated by 4 mm) filled with Synomag-D 70 nm (Micromod) SPIO. Imaging sensitivity was evaluated using 18 µL glass bulbs filled with diluted concentrations (1:1 to 1:64) of Synomag-D 70 nm.

Results and discussion: The presented results of imaging a 3D-printed spiral phantom filled with Synomag-D SPIO demonstrate a unique large FOV of 8 cm in a twofold increase of FOV over the previous system, which exceeded the FOV of the existing commercial preclinical scanners. The spatial resolution scan produced a 2D image in which the 4 mm spaced rods were distinguishable without digital alteration of image reconstruction. In the dilution imaging experiment, the lowest imaged sample corresponded to ~2.0 µg of iron content. This result meets the small tumor detection threshold of 4.8 µg of iron for a 1 mm^3 tumor size based on a 400 mg iron dose.

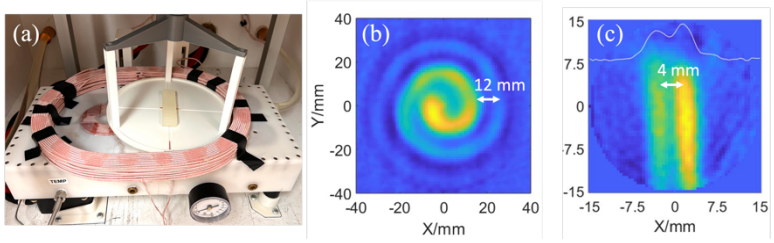

Fig. 1: a) Single-sided FFL MPI scanner with a resolution phantom; b) coronal image of spiral phantom; c) coronal image of two-rods resolution phantom.

Conclusion: We demonstrate significant improvements to a single-sided MPI scanner: enhanced spatial resolution, increased imaging sensitivity, and an expanded linear FOV. Moreover, the achieved spatial resolution falls within the range of human head MPI systems, which typically operate with gradients between 0.2–1.1 T/m, yielding corresponding resolutions of 12 mm to 3 mm [5-7]. Our scanner achieves this range with notably lower hardware complexity and power requirements. The imaging sensitivity meets the threshold for SPIO-labeled tumor detection. These results support the viability of the system for future clinical applications.

References: [1] Gleich, B., Weizenecker, J. Nature 435, 1214-1217 (2005). [2] Sattel, T. F et al. J. of Phys D : Appl Phys, 42, p.022001 (2009). [3] Kaethner, C. et al. IEEE Trans Magn 51, 2, 1–4 (2015). [4] McDonough, C., Chrisekos, J., and Tonyushkin, A. IEEE Trans Biomed Eng 71, 3470–3481 (2024). [5] Thieben, F. et al. Commun Eng 3, 47 (2024). [6] Sehl, O. C. et al. Mol Imag and Biol 27, 78–88 (2025). [7] Mattingly, E. et al. Phys Med Biol 70, 015019 (2025).

3D temperature mapping with MPI and MRI

N.J.O. Silva[1,2], J.F. Soeiro[1,2], S.P. Fernandes[1,2], J.M. Costa[1,2], T.A. Anjum[1,2], G.F. Resende[1,2], R.P. Oliveira-Silva[1,2], F.L.Sousa[2], V.M.Gaspar[2], J.F. Mano[2], P. Vogel[3,4]

[1]Departamento de Física and CICECO, Aveiro Institute of Materials Universidade de Aveiro, Aveiro, Portugal. [2]Departamento de Química and CICECO, Aveiro Institute of Materials, Universidade de Aveiro, 3810-193 Aveiro, Portugal. [3]Department of Experimental Physics 5 (Biophysics), Julius Maximilians-University Wurzburg, Wurzburg, Germany, [4]Pure Devices GmbH, Rimpar, Germany

Introduction: Temperature mapping in 3D is of utmost importance in different contexts, including hyperthermia therapies where heat is delivered to malign tissues and temperature should be controlled in space and time. MRI and MPI offer a great opportunity to obtain such measurements with complementary strengths in terms of temperature, space and time resolutions. In MRI, the intrinsic temperature variation of parameters such as T1, T2 and resonance frequency have been explored together with contrast-based approaches where a contrast agent increases temperature sensitivity. In MPI, the temperature variation of superparamagnetic nanoparticles such as magnetite has also been explored. However, in the temperature window of hyperthermia therapies this variation is small and hard to tune since is governed by the ratio between magnetic and thermal energy, which changes dramatically at cryogenic temperatures but much less around room temperature. Here we present a strategy to map temperature around room temperature based on magnetic nanoparticles with a magnetic phase transition tunable around room temperature, that provide variations of the MRI signal of about 10%/ºC and impressive variations of MPI signal of about 50%/ºC.

Methods: Magnetic Nanoparticles are synthesized by thermal decomposition and sol-gel methods (please see details here [1,2]). MRI images were obtained in a 0.5 T MRI using gradient-echo sequences and in a traveling-wave MPI, both from PureDevices GmbH.

Results and discussion: The magnetic nanoparticles are dispersible and stable in aqueous media, being able to provide temperature-dependent contrast, both in MRI and MPI. The relative variation of this temperature-contrast is tunable by the doping level of the nanoparticles. In particular, when the maximum contrast variation is tuned for ~42 ºC, we are able to produce 3D temperature maps in the context of near-infrared thermal treatment in 3D cellular assembles that mimic tissues, as shown in Fig. 1

Conclusion: Contrast agents with a controlled magnetic phase transition can be explored to generate 3D temperature maps both in MPI and MRI. This can find application in temperature monitoring during laser hyperthermia, for instance.

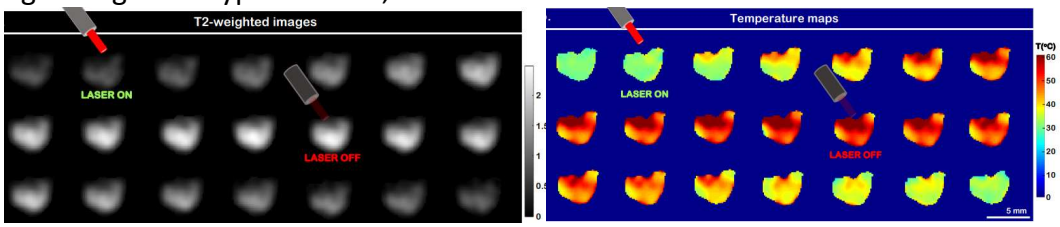

Fig. 1: T2-weighted and temperature images obtained with a cell sample before, under NIR irradiation for 82 s at 0.67W cm^{-2}, and after that irradiation (8 s integration time per image, pixel size of 0.16 mm).(From[1])

References: [1] Soeiro et al., Small Structures (2025). [2] Soeiro et al., ChemRxiv (2024).

Multimodal imaging of flow dynamics in a realistic aneurysm phantom

T. Reichl[1], A. el Ahmar[2], T. Kampf[3], J. Günther[1,7], M. A. Rückert[1], T. A. Bley[4], S. Herz[1,5], S. Schnell[2,6], V. C. Behr[1], P. Winter[2,6], P. Vogel[1,7]

[1]Department of Experimental Physics 5 (Biophysics), Julius-Maximilians University Würzburg, Germany, [2]Department of Medical Physics, University of Greifswald, Germany, [3]Department of Diagnostics and Interventional Neuroradiology, University Hospital Würzburg, Germany, [4]Department of Diagnostics and Interventional Radiology, University Hospital Würzburg, Germany, [5]Radiologie Augsburg Friedberg, Augsburg, Germany, [6]Department of Radiology, Northwestern University, Chicago IL, United States, [7]Phase Vision GmbH, Rimpar, Germany.

Introduction: An aneurysm is the pathological enlargement of a blood vessel, with rupture and treatment complications posing significant risks due to potential life-threatening bleeding [1]. Blood flow dynamics are crucial for aneurysm formation and rupture risk assessment [2]. This study compares flow dynamics in realistic aneurysm phantoms using 4D flow MRI [3], Magnetic Particle Imaging (MPI) [4], and Optical Transmission (OT) [5] and investigates the impact of various artificial aneurysm curvatures.

Methods: The aneurysm phantom was created as follows: starting from anatomical CT or MRI data, the desired structure was extracted, converted into a 3D model, and prepared for SLA printing using flexible resin. The phantom was placed in the center of the scanner and connected with pipes to the pump. The flow dynamics were determined using three different imaging modalities: 4D flow MRI [8] enables accurate measurements of 3D flow fields but requires long scan times. OT offers direct flow visualization of food color bolus but requires translucent samples and an opacity-inducing tracer. MPI enables real-time imaging of a magnetic nanoparticle bolus without background signal.

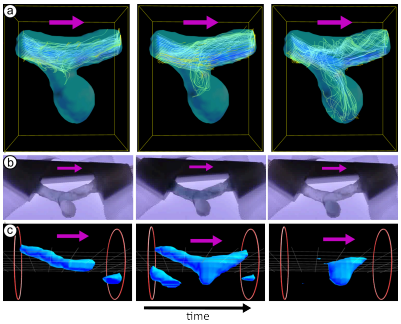

Fig. 1: Flow dynamics visualization in realistic aneurysm phantom with (a) 4D flow MRI, (b) OT and (c) MPI.

Results: The flow dynamics of a realistic aneurysm phantom were measured with 4D flow MRI, OT and MPI. The streamline visualization of the flow dynamics measured with 4D flow MRI is shown in Fig.1a. The bolus visualization for food color (OT) (Fig.1b) and Perimag® (MPI) (Fig.1c) show that bolus initially passes the aneurysm and then swirls partly into the aneurysm head, where it remains longer. Investigating the influence of vessel curvature on flow dynamics with MPI revealed significant influence on the flow dynamics inside the aneurysm head (Fig.2). The same was observed using 4D flow MRI.

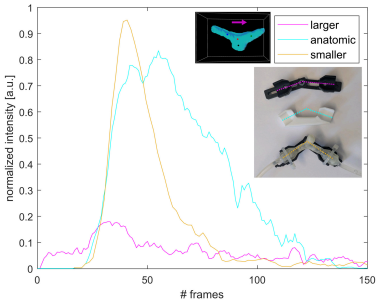

Fig. 2: Intensity tracked over time at the aneurysm head (see black point) for different aneurysm angles: larger than anatomic (pink), anatomic (blue) and smaller than anatomic (yellow).

Discussion and Conclusion: The measured flow dynamics showed good agreement and provided complementary information on the flow field and tracer distribution. Since the curvature of the aneurysm vessel was found to strongly influence the flow dynamics, further characterization of the aneurysm geometry must be performed.

References: [1] DeLuca et al., Neurovascular Neuropsychology, Springer (2020), [2] Neupane, et al. , J. Surgery (2022), [3] Markl et al. , J Magn Reson Imaging (2012), [4] Gleich, Weizenecker , Nature, (2005), [5] Adrian, Annual Review of Fluid (1993), [6] Reichl et al., Int J Mag Part Imag. (2022), [7] Guggenberger et al., J Magn Reson Imaging. (2021), [8] Schnell et al., J Magn Reson Imaging. (2017).

Book of Abstracts

ICMRM '25

Awards Sessions 1 & 2

Erwin Hahn Lecturer Awards

Paul Callaghan Young Investigator Award

Spatially-Resolved Magnetic Resonance: More Than Just a Camera

L.F. Gladden
Department of Chemical Engineering and Biotechnoogy, University of Cambridge,
Philippa Fawcett Drive, Cambridge CB3 0AS, U.K.

As in any research field, 'timing' plays a huge role in the opportunities we have and the research directions we take - particularly when you are starting a research group. In my case, the lucky 'timing' was in being hired in a chemical engineering department at much the same time as the early availability of commercial magnetic resonance spectrometers equipped with the hardware and basic software to do both chemical spectroscopy and diffusion/flow measurements, and with the ability to obtain spatial resolution in these measurements. This lecture will reflect on how spatially-resolved magnetic resonance has become increasingly useful in advancing our understanding of the physical and chemical processes that play important roles in the performance of many chemical technologies.

The motivation for the group's work has always been to *understand* the physics and chemistry underpinning the performance of a given application. Can we use magnetic resonance to remove bottlenecks in our understanding as we move from the basic science on which a technology is based through to the implementation of that technology? The questions that we seek answers to drive the development and implementation of new magnetic resonance methods in the group.

The lecture will include examples of some of the major themes of our activities over the years:

- Sorbents and catalysts: The importance of heterogeneity
- Three-dimensional structure and flow imaging: Measuring quantities that had never previously been measured
- The ability to measure unsteady-state behaviour: Undersampling, compressed sensing and Bayesian approaches
- *Operando* spatially-resolved magnetic resonance: Measurements at process operating conditions

Most importantly, this lecture is an opportunity to celebrate the work undertaken by all the research students, post-doctoral researchers and academic colleagues who have worked in the group, and the friendship of so many senior academics around the world.

Flexible Radio Frequency Pulse Optimization using Deep Learning Methods

Tristhal Parasram, Dan Xiao
University of Windsor, Windsor, Canada

Introduction:

Finding optimal MR pulses and pulse sequences for specific applications has long been an area of interest. Recently, deep learning has been explored for MR pulse optimization [1-3], demonstrating flexibility in targeting specific pulse characteristics [4]. In this work, we present a flexible pulse optimization framework that leverages modern deep learning methods to tune pulses based on a set of input-output examples. Previously, we optimized a pair of 90° and 180° pulses for a slice selective CPMG. In the current study, an improved framework has been applied to optimize prefocused excitation and refocusing pulses with uniform magnitude response and constant phase across the target bandwidth (BW), as well as delay-focused excitation pulses [5] that rephase after a specific duration. Furthermore, low B1 amplitudes were achieved, potentially requiring minimal or no RF amplification from an external power amplifier.

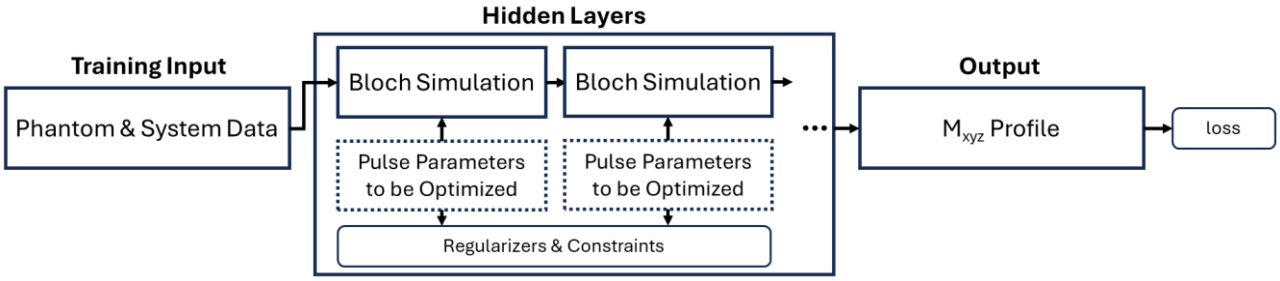

Fig 1. The model structure for RF pulse or pulse sequence optimization. The pulse amplitude, phase and/or gradient are stochastically optimized on batches from a large dataset of simulated phantoms. The dataset describes the desired effect of the pulse through examples of initial conditions and target pulse response. Constraints and regularizers are incorporated into the loss function as additional terms.

Methods:

RF pulses were optimized using a TensorFlow model comprising a trainable pulse parameter layer and a differentiable Bloch simulation layer. The optimization workflow is outlined in Fig. 1. The function of the rf pulse is defined by a dataset of initial conditions and corresponding target responses. The dataset includes system parameters, a sample phantom, and the desired effect of the pulse on the phantom. The model is trained to minimize the difference between the simulated and target responses across a group of phantoms, as specified by the loss function.

$$loss = MAE(\boldsymbol{M_{pulse}}, \boldsymbol{M_{target}}) + \|P_{amp}\|_2 + \|P_{phase}\|_2 + \|P_{grad}\|_2 + R(P) + C(P) \quad (1)$$

The first term is the mean absolute error between the simulated and target responses. The 2nd-4th terms are L2 norms on the pulse parameters, and the last two terms represent any regularizers R and constraint penalties C applied to the pulse.

In this work, the model was trained on 2^{16} simulated phantoms with random frequencies within a 1kHz range, minimizing post-pulse magnetization error relative to 3 target states. The first target is a prefocused excitation that flips equilibrium magnetization purely to M_y. This is paired with a refocusing pulse trained to perform a 180° rotation about the x-axis on randomly oriented M_{xy} with a small z component. Finally, a delay-focused excitation was developed, similar to the prefocused 90° target, but with an added free precession layer following the pulse, causing the magnetization to come into phase a specified time after transmission. To produce practical, low-amplitude RF pulses, L2 regularization and amplitude constraints were applied to the pulse parameters P.

Results and Discussion: A 10 ms prefocused 90° excitation and 180° refocusing pulse (Fig. 2 a,b) were optimized to achieve a uniform M_y flip across a 1 kHz BW. The resulting frequency response profiles for the 90 (Fig. 2c) closely matched the target, without the linear phase observed in a square pulse (Fig. 2e). In the presence of significant B0 inhomogeneity, Mxy phase variation cannot be removed by applying a gradient pulse. The prefocused pulse produces in-phase magnetization immediately after transmission. The optimized 180° refocusing pulse preserves magnetization across the BW without distortion at the echo (Fig. 2d), whereas the rectangular 180° pulse further reduces M_{xy} at higher frequences (Fig. 2f). Overall, the optimized result provides more uniform spectral weighting, minimizing attenuation of high-frequency components.

Delay-focused 90° pulses were optimized to generate echoes 0.5 ms, 1 ms, and 2.5 ms after transmission. The pulse with a 1 ms delayed focus (Fig. 3a) produced a frequency response similar to Fig. 2c at the echo time. Applied experimentally to an aqueous $CuSO_4$ phantom, it yielded a correctly timed echo (black), compared to a conventional hard-pulse spin echo (red) in Fig. 3b which was delayed by 1 ms. In simulation, a standard sinc pulse produces an echo with a 5 ms delay. The optimized pulse amplitude was 20% higher than a hard 90° pulse but 40% lower than a hard 180° pulse of equivalent BW.

When T_2* star is very short, the signal may be lost during the dead time. A delay-focused pulse can overcome this by shifting the point of rephasing beyond the dead time. For example, reducing the pulse duration to 200 us allows an echo delay of 50 us potentially bypassing the probe deadtime.

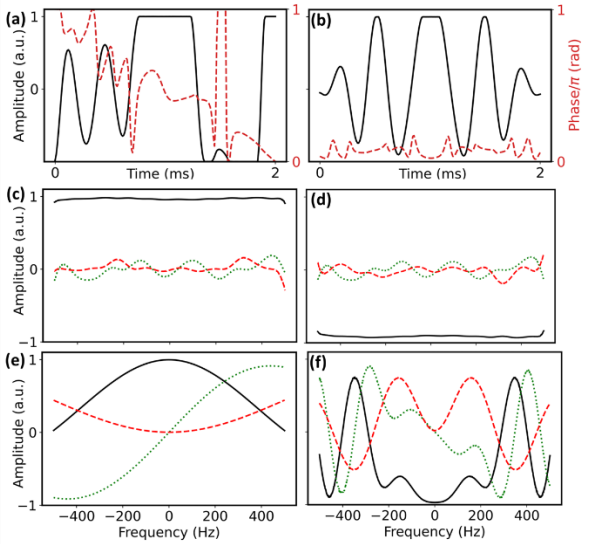

Fig 2. (a) Optimized 90° excitation and (b) 180° refocusing pulses, with amplitude (black) and phase (red dashed). The phase is constrained between 0 and π, and the pulse amplitude is flattened at the top due to the peak amplitude constraint. (c) Simulated magnetization response to the optimized 90° pulse and (d) optimized 180° pulse applied in a spin echo sequence with a 2 ms echo time. (e) Simulated magnetization response to a hard 90° excitation with equal peak amplitude to the optimized pulse, and (f) hard 180° pulse with the same amplitude as the optimized refocusing pulse, also applied in a spin echo. Responses are shown at the echo time. Colors: solid black = M_y, dotted green = M_x, and dashed red = M_z.

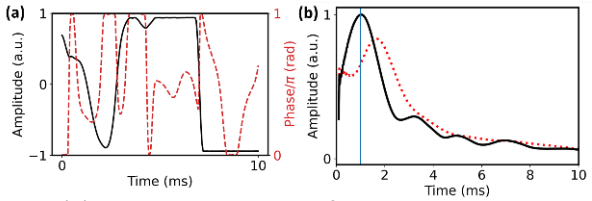

Fig 3. (a) Optimized 90° delay-focused excitation pulse with amplitude (black) and phase (red). (b) Experimental FID signal magnitude after the optimized 90° (black) and a spin echo signal with 2 ms echo time (red) on an aqueous $CuSO_4$ phantom containing titanium metal to increase B0 inhomogeneity. The vertical line marks the target echo time.

For a 60 mm, 2MHz solenoid coil, the RF power required to achieve a 1kHz bandwidth is on the order of tens of milliwatts. If only a 100-200 Hz bandwidth is required, the power can be reduced to <1mw, potentially eliminating the need for an external RF amplifier.

Conclusion: A flexible pulse generation framework was developed that requires only initial system conditions and corresponding target responses. The optimized pulses are particularly useful for low-field, low-cost MR systems with greater B0 inhomogeneity, and for systems with short T_2*. The pulses were validated through simulation and experiment. The framework also supports extension for pulse sequence design, incorporating B_0 and B_1^+ maps, power and slew penalties, and more.

References: [1] Loktyushin et. Al, Magn. Reson. Med. (2021). [2] Zhu et. Al Magn. Reson. Med. (2022) [3] Perlman et. Al Magn. Reson. Med. [4] Jang et. Al, Magn. Reson. Med. (2024). [5] Shen, Jour. Magn. Reson. (2001). [6] Parasram et. Al ISMRM (2025)

Investigation of Mixing Processes in Fluid Flow: Improving MRV Turbulence Quantification and Passive Scalar Distribution Measurements

S.Romig[1], K. John[1], S. Grundmann[1], M. Bruschewski[1]
[1]University of Rostock, Rostock, Germany

Introduction: Mixing processes play a critical role in many industrial flows, such as the blending of air and fuel in gas turbines. Benchmark experiments are conducted in water channels, where key non-dimensional parameters like the Reynolds number ensure similarity to real-world systems. Turbulent mixing is very effective and hence of particular interest. Understanding these mechanisms requires quantitative measurements of the Reynolds stress tensor (RST) for quantifying turbulence and the distribution of a passive scalar. Currently, RST measurements are often compromised by systematic errors, and passive scalar measurements suffer from high noise levels. These limitations hinder the accurate calculation of gradients and derived quantities such as the turbulent Prandtl number, which are essential for deeper analysis.

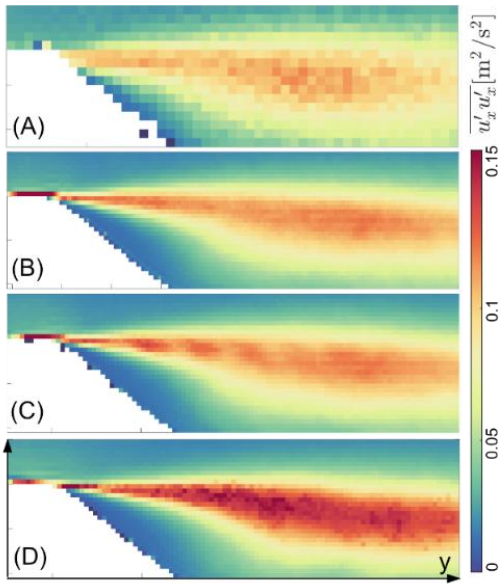

Fig. 1: streamwise RST component from (A) LDV, (B) improved sequence combined readouts, (C) improved sequence, one readout, (D) conventional sequence

This study presents the current progress of a doctoral research project aimed at advancing MRI technology for fluid dynamics applications. The work focuses on enhancing Magnetic Resonance Velocimetry (MRV) pulse sequences to improve RST measurements, as well as refining Magnetic Resonance Contrast (MRC) methods for passive scalar acquisition. The paper concludes with a demonstration of the improved MRV and MRC techniques in a representative experimental setup.

Methods: The current state-of-the-art MRV turbulence quantification is the intravoxel phase dispersion (IVPD) technique [1]. In a phase-contrast gradient recalled echo sequence, the first-order gradient moment M_1 encodes the velocity of the nuclear spins to the signal's phase. Turbulence leads to a velocity distribution producing phase dispersion that results in signal loss. However, the signal's phase also depends on velocity derivatives encoded by higher-order gradient moments. These can lead to overestimating the RST using the IVPD method, as shown in [2]. The idea is to minimize higher-order gradient moments by minimizing TE. Eq. 1 shows the Taylor series of the fluid motion inserted into the signal's phase angle ϕ.

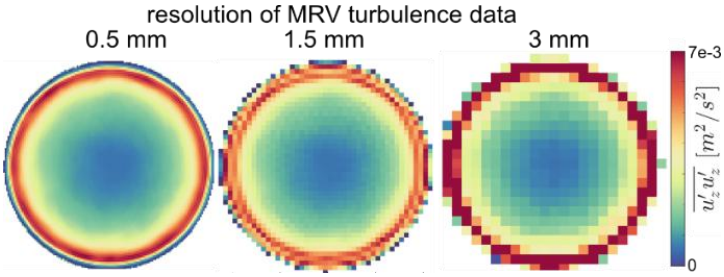

Fig. 2: streamwise RST component acquired with varying resolution

$$\phi = \gamma \int G_x(t)\, x \, dt = \phi_0 + \gamma r_0 \int_{t_0}^{TE} G(t)dt + \gamma u \int_{t_0}^{TE} G(t)t dt + \gamma a \int_{t_0}^{TE} \frac{G(t)t^2}{2} dt + \ldots$$
$$= \phi_0 + \gamma r_0 M_0 + \gamma u M_1 + \frac{\gamma a}{2} M_2 + \cdots \quad \text{Eq. 1}$$

ϕ_0 is the background initial phase, t_0 is the isophase point, when all spins are phase-aligned during excitation, r_0 is the spin's initial position, u its velocity and a its acceleration. It supports the intention of minimizing TE to minimize higher-order gradient moments, as they depend on higher

powers of time. This is achieved via three measures: a high receiver bandwidth and an asymmetric echo shortening the readout gradient, and FAST velocity encoding shortening the velocity encoding process. The low-frequency Gibbs ringing induced by the asymmetric echo is eliminated by applying an inverted readout and combining both partial k-spaces to one whole k-space [3]. Furthermore, previous results indicate that an insufficient voxel size leads to a systematic overestimation of turbulence peak values. Therefore, experiments were conducted with varying spatial resolution in a simple pipe flow and compared to reference data from [4].

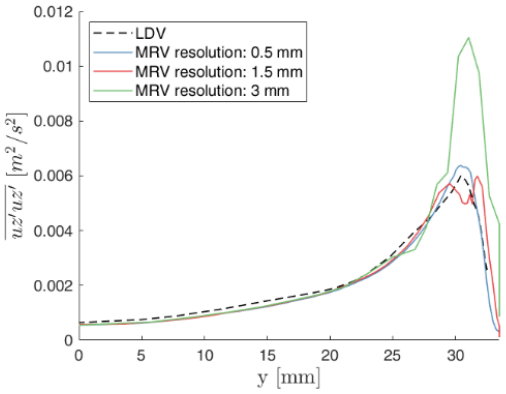

Fig. 3: circumferential average of streamwise RST component acquired with varying resolution compared to LDV data

Results and Discussion: Fig. 1 shows the streamwise component of the RST $\overline{u_x'u_x'}$. The Laser-Doppler-Velocimetry (LDV) reference data (A) and the improved MRV sequence with combined readouts (B) show good agreement, where the sequence without inverted readout shows ringing (C) and the conventional IVPD sequence (D) leads to overestimation of turbulence. The improved sequence reduced the deviation from the LDV data by a factor of 5. The behavior depicted in Fig. 2 and Fig. 3 contrasts with many other fluid mechanic measurement techniques, where low resolution typically results in underestimating peak values due to spatial averaging. Instead, for MRV, overestimation can be observed for lower resolutions. For a resolution of 1.5 mm, even qualitative deviations arise due to an unfavorable choice of resolution, which causes Gibbs ringing in the turbulent peak. The overestimation in MRV arises mainly from mean velocity variations within voxels, which introduce additional intra-voxel phase dispersion. This phenomenon becomes more pronounced as voxel size increases. Correction methods proposed in [4] only apply in case of linear velocity gradients, but for lower resolutions, the gradients are nonlinear here. This suggests that a sufficient resolution is crucial in MRV turbulence quantification. In Fig. 4, a representative benchmark experiment for turbulent mixing [5] with the main channel with cubic obstacles and a jet, where the contrast agent was added, is shown. The top shows the results from the MRC measurements, and the bottom shows the turbulence kinetic energy (TKE $= \frac{1}{2}$ $(\overline{u_x'u_x'} + \overline{u_y'u_y'} + \overline{u_z'u_z'})$), which is often used in fluid mechanics to quantify the amount of turbulence. The MRC quality could be enhanced by exact control of the boundary conditions, which allowed for multiple averages, improving the SNR.

Conclusion:

Improving RST and MRC measurement techniques in generic setups allows for the accurate investigation of mixing processes in more complex industrial applications like gas turbines. This data can hopefully be a basis to validate models for numerical simulations in engineering design processes.

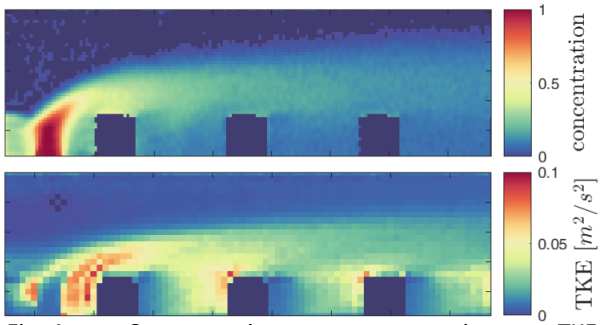

Fig. 4: top: Concentration measurements, bottom: TKE measurements

References: [1] Dyverfeldt, Magn. Reson. Imaging (2009). doi:10.1016/j.mri.2009.05.004; [2] Schmidt, Exp. Fluids (2021). doi:10.1007/s00348-021-03218-3; [3] Romig, Magn. Reson. Imaging (2025). doi:10.1016/j.mri.2025.110333; [4] den Toonder, Phys. Fluids (1997). doi: 10.1063/1.869451; [5] Benson, Exp. Fluids (2023). doi: 10.1007/s00348-023-03572-4.

Studying restricted diffusion with more accessible gradient amplitudes

A. Alfredo Ordinola[1], *B. Magnus Herberthson*[2], *C. Evren Özarslan*[1]
[1]Department of Biomedical Engineering, Linköping University, Linköping, Sweden, [2]Department of Mathematics, Linköping University, Linköping, Sweden

Introduction: Since its introduction in 1965, the Stejskal-Tanner (ST) pulse sequence [1] has dominated the diffusion MR studies of porous media, food products, and biological tissues. The ST signal is the Fourier transform of the ensemble-averaged propagator (EAP), a compromised version of the true diffusion propagator, which fully describes diffusion. Recently, a new gradient waveform (PROP; see Fig. 1) was introduced, capable of reconstructing the true propagator in both restricted compartments [2] and for free diffusion [3,4]. However, this method requires sampling a 2d-dimensional space (d = diffusion dimensionality), which is impractical. We introduce the reduced PROP (rPROP) technique, which matches the ST method in the number of measurements while providing additional information.

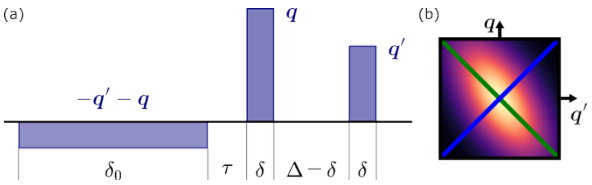

Fig. 1: (a) Propagator sensitive waveform (PROP) introduced in [2,3]. (b) 1D sampling space obtainable with PROP, ST is obtained with $q' = -q$ (green), while rPROP is obtained with $q' = q$ (blue).

In Fig. 1b, we show the qq'-plane that can be probed via the PROP method. The simulated free diffusion signal (provided in the background), is heavily suppressed in rPROP, due to the larger diffusion weighting (b -value) for the same q-value (or gradient amplitude). Since diffusion anisotropy typically arises from restricted diffusion [5], we use rPROP to detect anisotropy in samples with an overwhelming presence of isotropic diffusion. This is important for applications such as fiber-tract mapping in the brain, where the smallest trace of anisotropy could be indicative of an important connection. By taking the Fourier transform of the rPROP signal, we reconstruct the distribution of the mean value of the particles' positions at two time points defined by the two narrower pulses. This mean position distribution (MPD) is compared with the EAP available via ST.

Method: Pulse sequences featuring the rPROP and ST gradient waveforms were implemented on a 0.55T benchtop MRI system (*PureDevices*, Rimpar, Germany). To showcase the filtering effect of rPROP, data was acquired from a dairy cream (DC) sample. A two-compartment model is employed: a restricted compartment for the fat globules and a free diffusion compartment for the fluid they are suspended in. Both measurements were performed with a q_{max} of 127.3mm^{-1}. R_0 (sphere radius) was estimated from a subset of the samples (I_q in Fig. 2a) to assess whether low-to-mid q-values are sufficient to accurately extract restriction information.

The filtering capabilities of rPROP were then employed to detect anisotropy in predominantly isotropic samples. A celery stalk was scanned (with no imaging gradients) and analyzed with a multidimensional (md) approach akin to DTI. Finally, two distributions were computed for a mouse spinal cord (SC) sample. Data from both sequences were acquired with q-values ranging from 0.09 to 127.32mm^{-1}. All diffusion gradients were applied perpendicular to white matter (WM) fibers. The mean position distribution $\bar{p}_\Delta(\bar{x})$, and the displacement distribution $\bar{p}_\Delta(\Delta x)$ were then estimated via inverse Fourier Transform of the rPROP and ST signal profiles, respectively.

Results and discussion: Signals from the DC sample (Fig. 2a) shows the filtering effect of the rPROP sequence as a faster decay in the signal. The ground truth and estimated sphere's radius with ST

and rPROP were 1.9, 4.39, 2.94µm, respectively, suggesting that rPROP provided better estimates in the same I_q range [6].

Images of the celery sample featuring diffusion encoding gradients applied perpendicular to phloem and xylem cells in vascular channels are shown in Fig. 2b. For the same gradient amplitude, soma regions are attenuated much faster with rPROP than with ST. The tensor ellipsoids [7] from mdrPROP and mdST show their main eigenvector aligned along the orientation of the vascular channels, though the one obtained from mdST shows a slight tilt ($\sim$7.3°). Furthermore, the tensor obtained with rPROP data features a higher fractional anisotropy (FA $\sim$ 0.13), than the one obtained with ST data (FA $\sim$ 0.09). Detecting anisotropy as done here is a very challenging task for any technique, as the anisotropic vascular channels barely constitute 2% (volume-wise) or 4% (signal-wise) of the total sample. Thus, it is remarkable that the tensor obtained with rPROP featured a higher FA and maintained the correct main diffusion direction. It is expected that more comparable results could be obtained had the ST signals been acquired with the same b-value rather than the same gradient amplitude as was done here. However, this would require a significant increase in gradient amplitude (approximately twice as large while maintaining the timing parameters employed here). These results show that with rPROP it is possible to probe anisotropy more conveniently even in very challenging environments. Finally, images of the SC sample are shown in Fig. 2c along with the computed distributions. In both distributions, GM features wider lobes when compared to WM. However, the differences between the two regions are more conspicuous for the mean position distribution.

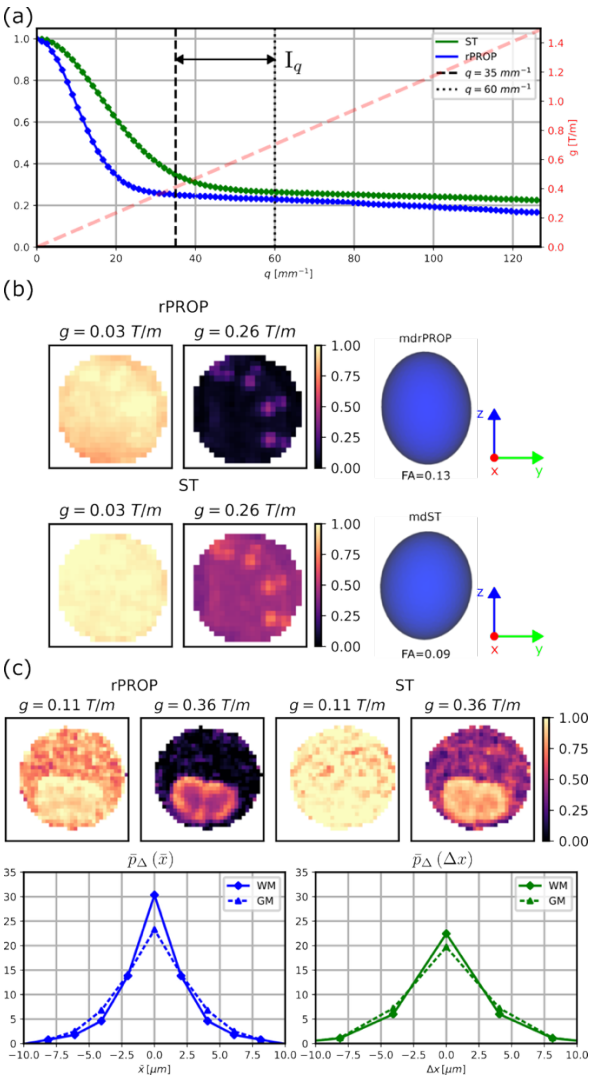

Fig. 2: (a) Signals obtained from the DC sample with ST (green) and rPROP (blue). Timing parameters: δ=2ms and Δ=30ms, δ_0=35ms, and τ=1ms. (b) Images of the celery sample acquired with rPROP and ST, and estimated ellipsoids. Timing parameters: δ=2ms and Δ=20ms, δ_0=30ms, and τ=3ms. (c) Images of the SC sample acquired with rPROP and ST sequences, and estimated mean position (blue) and mean displacement (green) distributions for voxels corresponding to white and gray matter. Timing parameters: δ =2ms and Δ =10ms, δ_0 =10ms, and τ=1ms.

Conclusion: In this work, we presented a new diffusion acquisition and analysis framework (rPROP), and showed its superiority over the ST measurements at elucidating the typically more interesting restricted compartments in complex specimens thanks to its inherently high diffusion weightings. As such, the rPROP method could be a viable alternative to the Stejskal-Tanner measurements in all characterization studies.

References: [1] Stejskal & Tanner, J. Chem. Phys. (1965). [2] Özarslan, Yolcu, Ordinola, Boito, Dela Haije, Højgaard, & Herberthson, J. Chem. Phys. (2023). [3] Özarslan, ISMRM (2021). [4] Ordinola & Özarslan, ArXiv (2021). [5] Beaulieu, NMR. Biomed. (2002). [6] Hinrichs & Kessler, J. Food. Sci. (1997). [7] Basser, Mattiello, & LeBihan, Biophys. J. (1994).

Magnetic Resonance Imaging and numerical modelling of vibrated bubbling gas-solid fluidized beds

M. Özdemir[a], *N. Hildebrandt*[a], *T. Lenczyk*[a], *M. Adrian*[a], *S. Pietsch-Braune*[a], *S. Benders*[a], *S. Heinrich*[a], *A. Penn*[a]

[a] Hamburg University of Technology (TUHH), Hamburg, Germany

Introduction: Vibrated gas-solid fluidized beds are widely used in chemical engineering applications involving granular materials, such as tablet coating in pharmaceuticals. Investigating the hydrodynamics is challenging because industrial-scale beds are large, opaque, three-dimensional (3D), and difficult to vibrate, leading many studies to rely on pseudo-two-dimensional setups that do not accurately reflect industrial conditions. In the past Magnetic Resonance Imaging (MRI) was used to resolve bubbles and measure particle velocities in 3D fluidized beds [1,2]. In these previous studies, a microimaging system and a clinical MRI scanner were used, limiting the height and diameter of the sample that can be analyzed and restricting the investigation of vibrated fluidized beds.

Methods: In this work, we used a large vertical-bore MRI system that enables the investigation of vibrated fluidized beds of various diameters. This MRI system offers unique radiofrequency (RF) shielding, allowing for the placement of an electrodynamic shaker, an RF-noise-emitting device, in the axis of the fluidized bed. Vibration was transmitted to the fluidized bed via glass-fiber-reinforced extension tubes (Fig 1.a, 1.b). The impact of vibration frequency (f) and amplitude (A) on bubble properties were investigated. MRI-active fluidized bed particles, agricultural seeds, and porous catalyst support particles of varying sizes loaded with pure water, were used to investigate the impact of particle size on fluidization. A tailored multi-channel receiver array (Fig 1.c, 1.d) for signal detection was used, allowing parallel imaging with Compressed Sensing (CS-SENSE). Gradient echo pulse sequence was used in MRI measurements with echo time of 0.75 ms and repetition time of 1.90 ms. The temporal resolution was 20 ms and the spatial resolution was 4 mm x 4 mm.

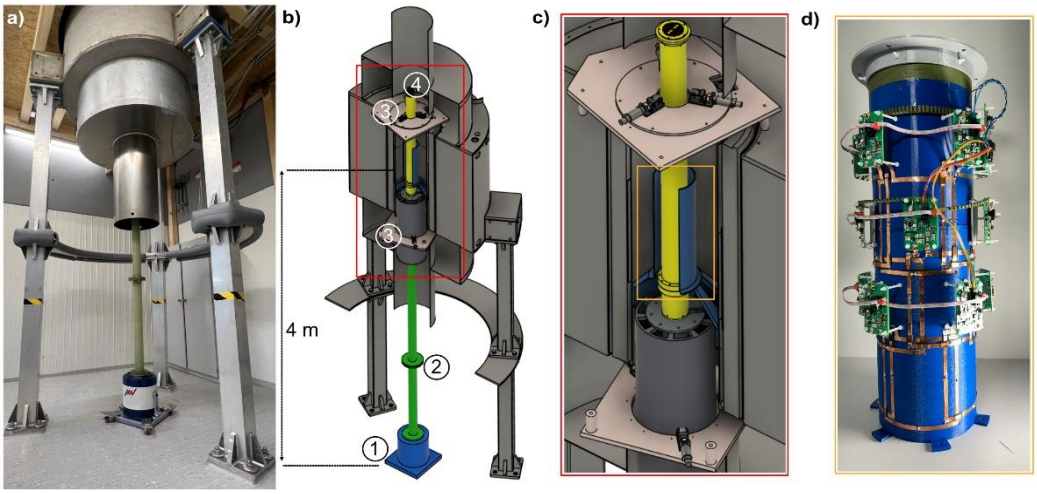

Fig. 1: a) A 3 Tesla large bore vertical MRI system, with the isocenter located 4 meters above ground. An electrodynamic shaker placed on-axis creates sinusoidal acceleration, which is transmitted through glass fiber-reinforced tubes to the fluidized bed. b) A 3D render of the 10 cm outer-diameter fluidized bed used in MRI measurements. 1=Electrodynamic shaker, 2=Vibration transmission tubes, 3=Bearing system, 4=Fluidized bed. c) A receiver array is placed around the fluidized bed in the MRI. The bearing system ensures that the motion of vibration is restricted to the axial direction. d) A 15-channel receiver array was used to detect signal from particles.

Results and discussion: Signal detection with a multi-channel receiver array enabled higher temporal resolution, 20 ms, and an improved signal-to-noise ratio (SNR) compared to the measurements using

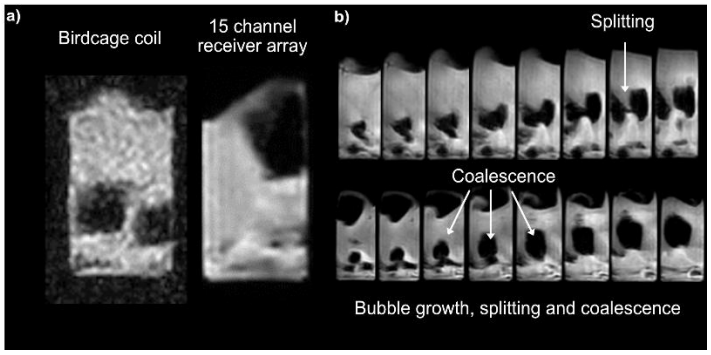

Fig. 2: MRI frames of poppy seeds fluidization in a 10 cm outer diameter fluidized bed a) with birdcage coil (left) and with 15-channel receiver array (right), b) Consecutive MRI frames showing important bubble events.

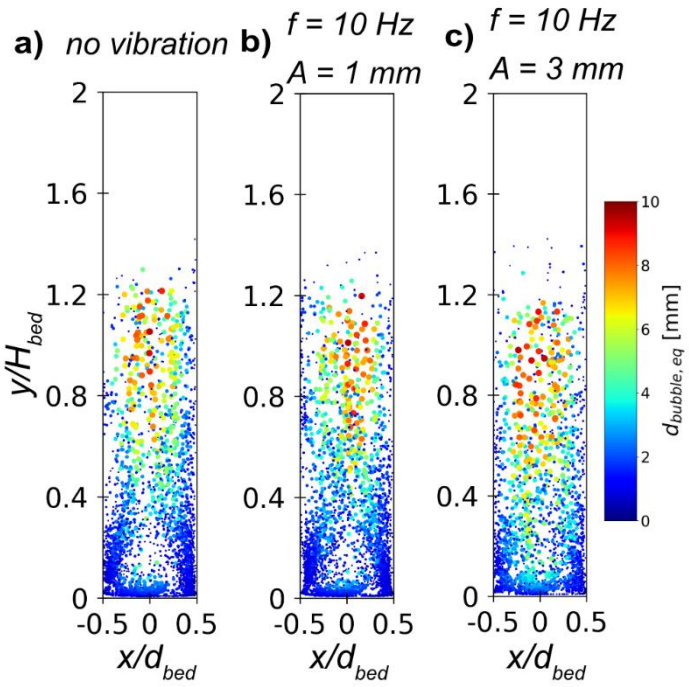

Fig. 3: Bubble size distribution of poppy seeds in the 10 cm outer diameter fluidized bed. Each circle represents a bubble centroid *(x, y)*, and the color indicates the equivalent bubble diameter ($d_{bubble,eq}$). The figure is normalized on the *y*-axis by the static bed height (*H*) and on the *x*-axis by the bed diameter (*D*).

Conclusion: Vibrated fluidized beds were investigated with MRI. Custom-built receiver array provided high temporal resolution, enabling the detection of gas bubbles. Besides agricultural seeds, the study included the fluidization of porous fine powders, expanding the scope of fluidized bed applications analyzed with MRI. We found that vibration led to a more uniform bubble size distribution. CFD-DEM simulations showed good agreement with the MRI data and established literature correlations.

the magnet's birdcage coil, 60 ms. (Fig 2.a). This enables the observation of important bubble dynamics that influence heat and mass transfer rates such as bubble growth, coalescence and splitting (Fig 2.b).

Agricultural seeds are commonly used in MRI studies of granular materials due to their high oil content, but they typically have similar particle sizes. In industrial fluidized bed applications, fine powders are also commonly utilized. In this work, we extended MRI studies to include a broader range of particles. Powders such as γ-Al_2O_3 were loaded with water and used in fluidized beds.

Impact of vibration on bubble properties were investigated by altering vibration frequency and amplitude. Vibrated fluidized bed resulted in a more homogeneous spatial distribution of bubbles (Fig 3). As the vibration amplitude increased, larger bubbles formed in the bed.

MRI data was further compared with numerical simulations, which combine Computational Fluid Dynamics and the Discrete Element Method (CFD-DEM). Initial results showed that the average equivalent bubble diameters derived from MRI measurements, CFD-DEM simulations, and established literature correlations are strongly consistent.

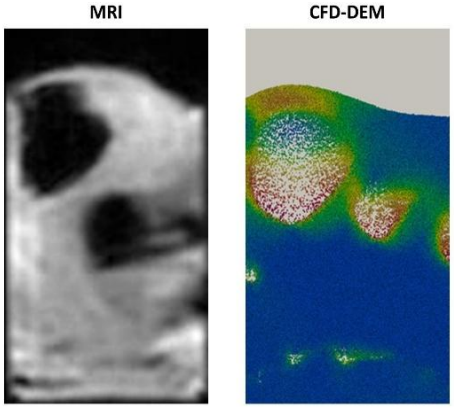

Fig. 4: A frame of poppy seeds fluidization (U/U_{mf} = 1.6) in a 10 cm outer diameter fluidized bed obtained from MRI and CFD-DEM simulation.

References: [1] Müller et al., Physical Review E, (2007). [2] Penn et al., Science Advances, (2017).

Functional Brain Imaging and Targeted Lesion Studies Using Manganese-Enhanced MRI and Focused Ultrasound in Non-Conventional Model Species

Pierre Estienne[a,b], Gwenaël Pagé[a], Benoit Larrat[a], Kei Yamamoto[b], Luisa Ciobanu[a]
[a]NeuroSpin, Commissariat à l'Energie Atomique et aux énergies alternatives, Saclay, France
[b]Paris Saclay Institute of Neuroscience (NeuroPSI), CNRS, Univ. Paris-Saclay, Saclay, France

Introduction: Investigating the neural mechanisms underlying behavior in non-model organisms remains a major challenge due to the lack of suitable neuroimaging and molecular tools. Traditional techniques such as electrophysiological recordings and immediate early gene (IEG) mapping depend heavily on established stereotaxic brain atlases or species-specific antibodies, which are generally unavailable outside classical model organisms like rodents or zebrafish.
Surgical lesion studies, often used to confirm causal relationships between brain regions and behavior, face significant obstacles in species lacking stereotaxic coordinates or in aquatic animals where surgical environments are difficult to control. As a result, the scope of comparative neurobiology is often limited to a narrow group of tractable species.
To overcome these limitations, this study presents a protocol combining Manganese-Enhanced Magnetic Resonance Imaging (MEMRI) [1] for functional imaging with Magnetic Resonance-guided Focused Ultrasound (MRgFUS) for targeted, non-invasive brain lesions. This integrated approach is demonstrated in *Amatitlania nigrofasciata* (convict cichlid), a freshwater fish, and is adaptable to a wide range of species, offering new avenues for neuroethological and comparative research.

Methods:

MEMRI Functional Imaging: $MnCl_2$ is a contrast agent taken up by active neurons. We first optimized the $MnCl_2$ dosage and administration route by testing intraperitoneal and intramuscular injections at 50 or 75 mg/kg $MnCl_2$. Based on these results, our final experimental protocol employed intraperitoneal injections of $MnCl_2$ at a dose of 50 mg/kg. Post-injection, fish participated in repeated behavioral sessions involving a problem-solving task to promote behavior-linked manganese accumulation. Forty-eight hours later, animals were anesthetized and imaged on a 17.2 T Bruker Biospin MRI scanner using a volume transmit/receive coil with inner diameter of 45 mm. For manganese accumulation quantification we acquired T1 weighted images at 80 µm in plane resolution. Other relevant acquisition parameters are as follows: TR/TE 250/2.8 ms, 24 slices, slice thickness 0.2 mm, 40 averages. T1-weighted images were analyzed using retina-based normalization to compare manganese accumulation across brain regions.

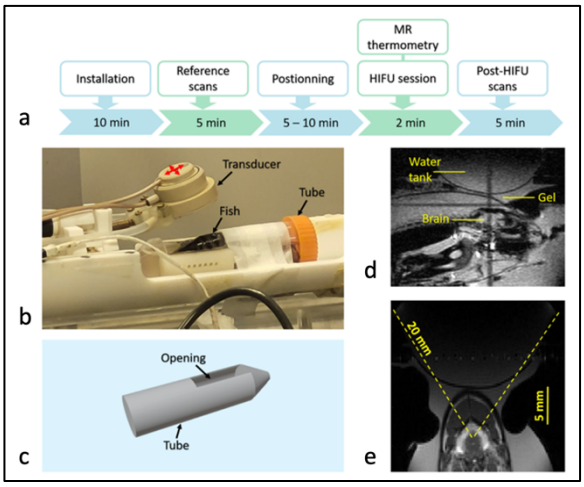

Figure 1. Experimental setup for simultaneous HIFU and MR imaging. a. Workflow of the study. b. MR and ultrasound setup. The transducer can move along the two perpendicular directions symbolized by the red arrows. c. The fish was placed in the tube and maintained in water under anesthesia. An opening was created to apply transducer on the fish head. Sagittal T1-weigthed (d.) and coronal T2-weigthed (e.) images.

HIFU Lesion Protocol: To validate functional imaging results, MRgFUS was used to induce thermal lesions in targeted brain areas [2]. An MR-compatible ultrasound transducer, placed in a 7T MR scanner [3], delivered 15-second sonications to the cerebellum with an estimated acoustic pressure

of 6 MPa. The focal spot was positioned using T2-weighted MR images (Figure 1). Real-time MR thermometry monitored tissue heating (~18°C increase), and T2-weighted scans taken 48 hours post-sonication assessed lesion formation. Visual confirmation was obtained via post-mortem inspection of formalin-fixed brains.

Results and discussion:

Intraperitoneal injection proved more effective than intramuscular administration, and the 50 mg/kg dose offered a reliable balance between contrast and animal safety (Figure 2). MEMRI enabled non-invasive visualization of behaviorally induced brain activity at sub-millimeter resolution. Manganese uptake was robust in regions associated with task engagement, with significantly higher signal intensities in the inferior lobe (mean relative intensity: 7139±388, n=10) of trained fish compared to controls (mean relative intensity: 6422±425, n=10, p<0.001).

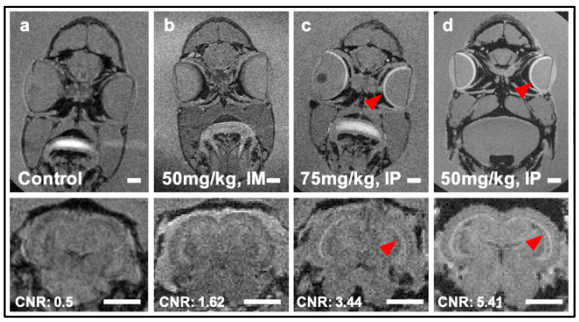

Figure 2. Manganese dosage for MEMRI in convict cichlids. T1 weighted images. a-d: Intraperitoneal injections provide better signal than intramuscular injections for similar manganese concentrations. Scale bar: 2.5mm.

HIFU induced well-localized brain lesions in the cerebellum without compromising overall health or motor abilities, allowing continued participation in behavioral tasks. MR thermometry effectively tracked focal temperature increases, while T2 signal changes and macroscopic hemorrhage confirmed lesion formation (Figure 3). Lesions in the inferior lobe, a region activated during task performance, resulted in impaired behavioral responses, validating its role in the task and demonstrating the utility of HIFU for causal studies of brain function. This dual approach addresses several limitations of traditional methods: it eliminates the need for surgical procedures or transgenic lines, allows precise targeting of deep brain structures, and can be implemented in species lacking detailed neuroanatomical data.

Conclusion: The combination of MEMRI and MR-guided HIFU represents a transformative toolkit for neuroethological research in non-conventional species. MEMRI enables functional mapping of neural activity linked to natural behaviors, while HIFU allows precise, non-invasive lesions to test causal involvement of specific regions. This methodology can be broadly applied to species across the vertebrate and invertebrate spectrum, including those lacking established genetic or anatomical resources [3]. By facilitating functional brain imaging and lesion studies in previously inaccessible species, this approach opens new avenues in comparative neuroscience and evolutionary biology.

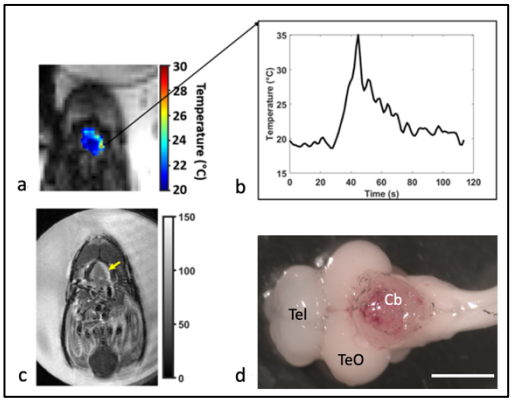

Figure 3. Thermal ablation of the cerebellum. a. Thermometry map of the cerebellum where a temperature rise was detected on the left. b. Temperature evolution over time during MR thermometry scan time. c. An hyperintense T2w signal was observed, 48 hours after HIFU protocol, at the location of the temperature rise indicated by the yellow arrow. d. Dorsal view of a lesioned fish brain, showing extensive hemorrhage in the corpus cerebelli (Cb).

References: [1] Radecki et al., PNAS (2014). [2] Dervishi et al., Int. J. Hyperthermia. (2013). [3] Magnin et al., J Ther Ultrasound (2025). [4] Wagner, Egelhaaf & Carr, J. Comp. Physiol. (2024).

Fascinated by NMR, MRI and … plants: about 50 years curiosity driven intact plant and plant materials applications with some relevant spin-off

Henk Van As

Laboratory of Biophysics, Wageningen University, Wageningen, the Netherlands

I entered the field of NMR during my MSc thesis work (1975) at the Physical Chemistry Laboratory, Free University, Amsterdam, headed by Prof. Cor MacLean. He was one of the Dutch pioneers in NMR. During this work 60 and 100 MHz (at that time high (!) field) NMR spectrometers were available.

I continued by starting a PhD thesis work on January 1 (!), 1977, at the Landbouwhogeschool (now Wageningen University), Wageningen. My thesis supervisor was Prof. Tjeerd Schaafsma. The topic was the study of water transport in plants by use of spin-echo NMR. I chose this position because of the dynamic and enthusiastic demonstration by Adrie de Jager during the application visit. I became attracted by spin echo dynamics and time domain NMR, may be plants, but was not (yet) aware of the complexity of plants and its consequences for NMR. It was really pioneering work.

In 1977 some of my, more experienced, colleagues did not believe that (whole body) MRI could ever be a method of choice in hospitals, based on the early noisy results. Notwithstanding, the first clinical systems became available in the early 80's! Significant and fascinating development of the technology followed in the decades since, leading to its widespread use in medicine and other disciplines as is clear from the spatially resolved magnetic resonance methods and their applications presented during the ICMRM (and MRPM) meetings.

After my graduation I continued as a PD and, since 1986, Associate Professor (Biophysics) at Wageningen University. The research focused on unravelling and understanding (not only water) transport processes and dynamics at different time and length scales in porous bio-systems to study structure-function relationships. For this, Time Domain NMR and quantitative MRI (correlated relaxometry, diffusometry and flow and the effect of exchange), and (rheo-)MRI methods and hardware were developed. Main applications were intact plants (production, hydraulic conductance, water limitation, product quality; first portable NMR flowmeter for flow in plants in 1982-1986), plant-like materials and foods (composition, processing, structure, function). The (some dedicated plant) NMR/MRI systems covered low field (10 MHz) up to very high field (up to 900 Hz).

In this lecture I will present results of my fascination, (portable) NMR, MRI and … transport in plants, as it developed during more than 40 years. It was curiosity driven research, resulting in some relevant spin-off. Certainly I have enjoyed it!

Serial, M. R., Terenzi, C., van Duynhoven, J., & Van As, H. (2022). MRI of Transport and Flow in Plants and Foods. *Magnetic Resonance Microscopy: Instrumentation and Applications in Engineering, Life Science, and Energy Research*, 237-261.

Book of Abstracts

ICMRM '25

Scientific Session 7

Plants

MRI in Plant Research: Unlocking the Hidden Life of Seeds

Ljudmilla Borisjuk
Leibniz-Institute of Plant Genetics and Crop Plant Research (IPK), Corrensstrasse 3,
06466 Seeland-Gatersleben, Germany

Magnetic Resonance Imaging (MRI), long established as a cornerstone of medical diagnostics, is increasingly recognized as a powerful tool for exploring the inner life of plants through *in vivo* imaging. What drives the adoption of MRI in plant research, and what obstacles must be addressed to fully realize its potential in this emerging field?

This presentation showcases how in vivo MRI, enabled by the newly established plant MRI platform at IPK [1], is opening new avenues for investigating the inner life of plant seeds. MRI now enables detailed investigations into embryogenesis and seed formation, the role of mechano-sensing, and the spatial and temporal dynamics of storage product partitioning in seeds [2,3, 4]. We've also developed method for the non-invasive visualization of sugars and amino acids in complex "sink organs" like fruits, taproots, and tubers, focusing on crops like maize, potato, and sugar beet [5].

Our new approach integrates deep learning algorithms with MRI to automate data analysis—exemplified by our MRI-Seed-Wizard [6], a tool that enables breeders to quantify more than 20 seed traits. Many of these traits cannot be measured using conventional methods, including X-ray computed tomography. Finally, I would like to share my vision of how MRI in plant science is evolving, highlight the need for closer collaboration between physicists and plant scientists to facilitate progress in the field [7].

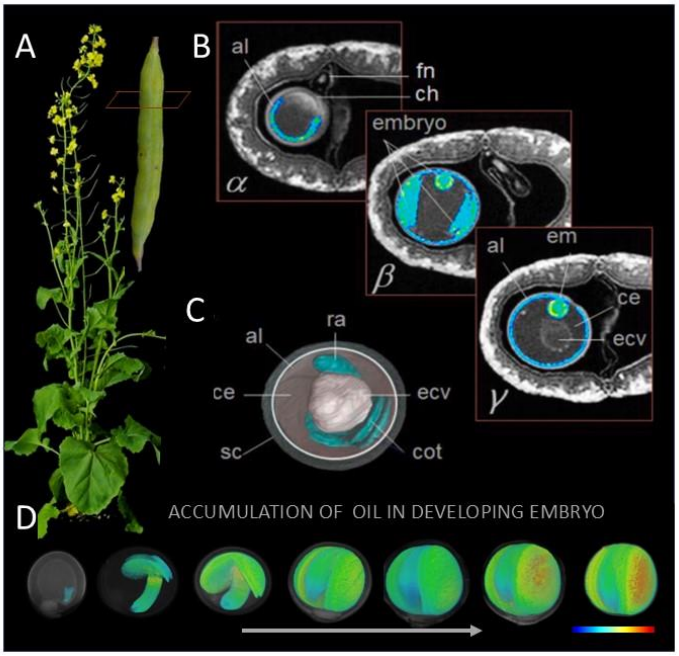

MRI-based visualization of tissue-specific lipid storage in developing embryo of oilseed rapeseed (*Brassica napus*). **(A)** Optical image of rapeseed plants and a typical silique, which contains seeds. **(B)** Virtual cross sections through the silique at mid cotyledon stage of development; lipid detected in the aleurone layer of endosperm and in the embryo proper. **(C)** schematic representation of the seed organs; **(D)** the developmental sequence of oil deposition in embryo. Abbreviations: al – aleurone; ce – cellularized endosperm; ch – chalazal region; cot – cotyledon; ecv – endosperm central vacuole; em – embryo; en – endosperm; fn – funiculus; ps – pseudoseptum; ra – radicle; sc – seed coat; se – seed; va – valve.

References: [1] Borisjuk, J. Plant Physiol. 309 (2025) 154502.
[2] Radchuk, Plant Cell 35 (2023) 2186-2207.
[3] Rolletschek, New Phytol. 244 (2024) 1328-1344
[4] Langer, Plant Physiol. 192 (2023) 1268-1288.
[5] Mayer, Sci. Adv. 10 (2024) eadq4424.
[6] Plutenko, J. Exp. Bot. 76 (2025) 393-410
[7]Borisjuk, New Phytol. 238 (2023) 1775-1794.

Establishing Ground Rules for Sensor-like Application of NMR Relaxometry for the Study of Water and Dry Matter Dynamics in Living Plants

A. Wörtche[a], *C. W. Windt*[a]

[a] Forschungszentrum Jülich GmbH, Institute for Bio- and Geosciences (IBG-2), Jülich, Germany

The largest challenge in measuring living plant organs by means of time domain NMR (TD-NMR) is that they constitute complex systems characterized by strong natural variation and spatial heterogeneity in their physicochemical properties. In NMR relaxometry this is reflected by a species and organ specific continuous distribution of T_1- and T_2- relaxation constants. Advanced multidimensional approaches can deal with this complexity and take advantage of the information that is available in the NMR data, but are time-consuming and difficult to execute and interpret. Routine characterization of intact plant organs requires dealing with this complexity in a way that is fast and suitable for non-expert operators. This might be achieved by a more sensor-like approach.

A straight-forward way to quantify some of the most elementary parameters to evaluate plant growth and yield; fresh weight (FW), water weight (WW) and dry weight (DW) is to distinguish between proton pools of different mobilities based on T_2 contrast. This can be done by comparing a measure of the total signal intensity representing both the liquid (PD_{liq}) and solid (PD_{sol}) proton fractions (=PD_{tot}), to a T_2-weighted estimate that correlates with more mobile liquid proton fractions in the sample. In this study, we explore the basic ground rules for such a T_2-weighted approach for the study of water and dry matter dynamics in living plants.

As a starting point of our analysis, we employ the previously defined Solid Liquid Content (SLC) method[1] which is based on this general idea. To test its applicability, we analyzed the relaxometric data of samples of organs of various species with widely varying water and dry matter contents and degrees of lignification (intact leaves, wheat kernels and bean pods). Despite the simplicity of the approach and the extreme heterogeneity of the physicochemical properties of plant tissue, the SLC method yields surprisingly good and linear correlations between PD_{tot} and FW, and PD_{liq} and WW, respectively. Yet, our results indicate that the SLC parameters are (slightly) susceptible to the sample specific structural and/or physicochemical properties. This has two consequences. First, the method is not generic for all species and samples, and thus needs frequent recalibration. Second, due to inherent variation in the structural and physicochemical composition of plant organs of similar origin, the accuracy of the SLC method is limited. Depending on the sample type and biological process to be studied, the accuracy may suffice to resolve the key dynamics of interest. Indeed, our results indicate that the method works well for tracking the dynamics of moisture and solid content in seeds and bean pods that exhibit large developmental changes. Contrary, the dynamics of water content in leaves of similar origin are in general small compared to the spread in the SLC results.

To ensure proper application of the method, further insight into the physicochemical and micro- and macro structural features that define the SLC parameters is required. The latter is especially relevant in the context of long-term measurements during which plant organs are expected to change these features due to e.g. senescence or as a response to environmental (stress) factors. Here, we present a systematic assessment of the relaxometric sample features probed by the SLC method in dependence of the choice of T_2-weighting and explore if finetuning of the weighting can reduce deviations in the SLC parameters and make the method more generic.

Reference: [1] C.W. Windt, M. Nabel, J. Kochs, S. Jahnke, U. Schurr, A mobile NMR sensor and relaxometric method to non-destructively monitor water and dry matter content in plants, Frontiers in Plant Science,12 (2021).

MRI of hydraulic failure in plants by means of a mobile, low field imager: can low spatial resolution be compensated by means of MRI relaxometry?

Carel W. Windt[a], *Viktor Sydoruk*[a], *Marco Meixner*[b]
[a] Forschungszentrum Jülich, Jülich, Germany
[b] Institut für Neuroradiologie, Bochum, Germany

Embolism formation in plants refers to the blockage of microscopic xylem vessels by air bubbles, as may be induced by severe drought. Emboli disrupt water transport from roots to leaves, causing hydraulic failure and ultimately plant mortality. Understanding the dynamics and spatial progression of embolism formation in the plant is crucial for assessing plant resilience in the face of climate change and extreme weather events.

Air emboli occur in xylem conduits that in most cases are much smaller than can be spatially resolved by MR imaging. A major strength of MR is that it can nonetheless visualize the process. MRI relaxometry allows to detect, rather than resolve, changes in tissue physicochemical properties and either quantify the corresponding NMR parameters, or to calculate high-contrast parameter maps.

The ability to detect embolism formation by means of spatially resolved relaxometry (i.e., with parameter maps of amplitude, T2, and combinations thereof) rather than to visualize it by brute resolving force, is especially helpful when dealing with low field MRI devices. These typically are based on permanent magnets that do not only have a lower field strength, but also lower homogeneity and higher peak width than laboratory-based supercon systems, and typically cannot muster the gradient strengths that such systems can. These factors together limit the spatial resolution that can be achieved.

In this contribution we explore how low spatial resolution can be chosen without losing the ability to detect embolism formation. By comparing MRI data of dehydrating poplar trees with highly resolved micro-CT images of the same specimens, we assess how micro-porous structures such as rays and wood fibers affect the results of spatially resolved MR relaxometry. Rays and fibers are structural wood elements that in broadleaf trees often occupy a larger fraction of the wood than do water conducting conduits (vessels and tracheids), but usually are overlooked both in terms of their contribution to MR contrast, as well as in terms of their function as a water storage compartment and contribution to stem hydraulic capacitance. To compare MRI and micro CT images automated routines were implemented, allowing for overlay, position correction and subsequent analysis of parameter images of dynamic changes in the xylem region.

We demonstrate that embolism formation can be quantified and visualized using a custom-built, mobile low-field MRI device, highlighting the potential for field-deployable MR imaging in plant hydraulic research.

Plants: A new application field for Chemical Exchange Saturation Transfer (CEST)

Simon Mayer[a,b], Fabian T. Gutjahr[a], Steffen Wagner[b], Ljudmilla Borisjuk[b], Peter M. Jakob[a]

[a] University of Würzburg, Institute of Experimental Physics 5, Würzburg/Germany

[b] Leibniz-Institute of Plant Genetics and Crop Plant Research, Gatersleben/Germany

Introduction: Chemical Shift Imaging (CSI) enables the *in vivo* detection of metabolites in living plant tissues (1). However, it can be challenging due to magnetic field inhomogeneities often occurring inside plants. Therefore, we applied Chemical Exchange Saturation Transfer (CEST) to plants (2). The CEST contrast arises from low-concentrated metabolites containing exchangeable protons. In this abstract we want to demonstrate the potential of CEST by showing exemplary results of measurements of barley and potatoes.

Methods: MR measurements were performed on a 9.4 T (barley grain) and 11.7 T (potato) MR scanner. We conducted CEST experiments in the range from ±5 ppm to detect the exchanging protons of the hydroxyl (at around 1 ppm) and the amino group (3 ppm). Even small saturations, such as a single block pulse of 200 ms duration and 2 µT amplitude, provided sufficient CEST contrast. For read-out a 2D spin echo sequence (RARE) was used. Before calculating the asymmetry spectra MRTasy, Z-spectra were B_0 corrected. CEST sugar (amino acid) maps were generated by integrating over the 1 ppm (3 ppm) peak in the asymmetry spectrum.

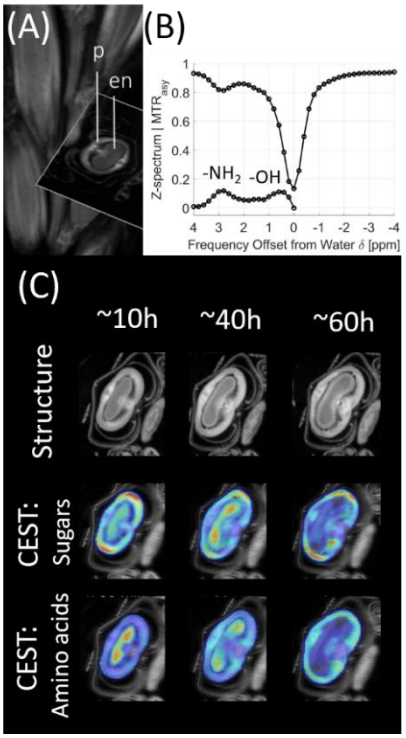

Fig. 1: (A) 3D images of a barley ear, showing position of the examined slice. p: pericarp, e: endosperm. (B) CEST spectrum from endosperm. (C) CEST-MTR$_{asy}$ maps during feeding of barley caryopsis.

Results and discussion: Both, sugars and amino acids, could be detected in the endosperm of barley grains by CEST (see Fig.1B). The endosperm of barley is shaped in two symmetrical wings, and the CEST spectra in these wings matched perfectly. Whereas in a separate CSI measurement (not shown) the NMR spectra varied due to T2* inhomogeneities. So, the decreased sensitivity to field inhomogeneities of CEST is an important advantage over CSI. In the following, the growing barley grain (attached to an intact ear) was monitored via CEST, showing the accumulation and decrease of sugar and amino acids (see Fig. 1C).

The applicability of CEST to much larger samples could be demonstrated: In our experiment with potato, CEST showed the distributions of sugars and amino acids within the tubers, whereby clear differences between varieties could be detected (Fig.2). So, it was shown that CEST is a versatile tool for the detection of sugars and amino acids in biological samples, whether small caryopses or larger sink organs. Monitoring dynamic growing processes is an interesting application where CEST-MRI provides new insight into the inner workings of intact plant tissues.

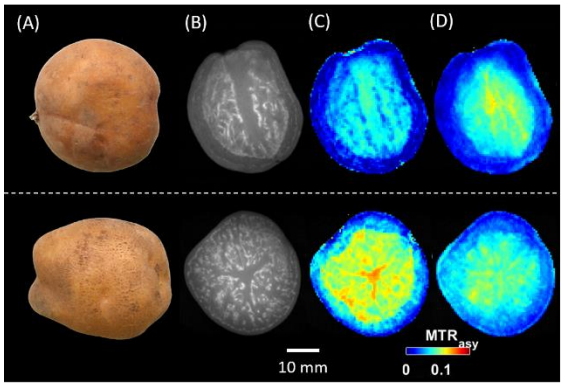

Fig. 2: CEST-MTRasy image for potato: (A) photograph of variety Ovalgelbe (top) and Flora (bottom), (B) structural MRI, (C) CEST-MTRasy image for sugars and (D) for amino acids.

Conclusion: We believe that CEST-MRI is a promising tool for plant examination and should be further explored in future research.

References: [1] Borisjuk et al., New Phytol. 238 (2023) 1775-1794. [2] Mayer et al., Sci.Adv.10, (2024) [3] Kim, et al.: Magn Reson Med (2009).

MRI mapping of structural anisotropy in plant-based protein extrudates.

S.A. Kuijpers[1], E.D. Garina[2], M.I. Gobes[1], F.J. Vergeldt[1], J.P.M. van Duynhoven[1,3], C. Terenzi[1]
[1]Laboratory of Biophysics, Wageningen University and Research, Wageningen, The Netherlands, [2]Department of Radiation Science and Technology, Delft University of Technology, Delft, The Netherlands, [3]Unilever Global Foods Innovation Centre, Wageningen, The Netherlands.

Introduction: High-moisture extrusion (HME) of plant-based proteins is the dominant industrial processing method for producing fibrous meat alternatives. Yet, the mechanisms by which fibrous anisotropic structures are formed in protein extrudates are not fully understood [1]. Conventional measurement techniques adopted for structural characterisation [2] typically do not provide spatially-resolved and/or molecular-level information. In our work, we used complementary and multi-modal techniques based on Time Domain (TD-)NMR, Chemical Exchange Saturation Transfer (CEST), Diffusion Tensor Imaging (DTI) MRI, Diffuse Reflectance (DR) [3] and Small Angle Neutron Scattering (SANS) [4], to spatially describe the development of structural anisotropy in extrudates, based on soy protein concentrate (SPC), from the molecular to macroscopic scale.

Methods: Samples were extruded using an XtruTech XTS19 at lab-scale and a Bühler PolyTwin at pilot-scale. MRI images were acquired using a 25-mm bore 600 MHz (14T) Bruker MRI spectrometer. T_1- and T_2-weighted RARE and DTI images were acquired on frozen-thawed and swollen extrudates at a resolution of 39x39x500 μm^3. RARE images were analysed using Rotation Fourier Transform, resulting in Weighted Order Parameter (WOP) maps [5], and DTI data was processed according to Kingsley (2006) [6]. CEST images were acquired using a 5-mm bore 1200 MHz (28T) Bruker MRI spectrometer at a resolution of 50x50x100 μm^3 and analysed according to Mayar *et al.* (2023) [7].

Results and Discussion: Low-field TD-NMR and high-resolution MRI revealed the anisotropic phase-separation of extrudates into protein-rich (PR) and water-rich (WR) lamellae. Ultra-high resolution CEST MRI data confirmed the presence of protein inside the WR lamellae. Freeze-thawing enhanced delamination of the WR and PR domains. MRI images and WOP maps revealed that lamellar phase separation is mostly visible close to the cooling die wall, and is dominantly oriented along the extrusion direction. Similar findings were obtained by SANS, at the nm-scale, and by DR, at the μm-scale. During passage of the cooling die, a clear increase in the volume fraction of the lamellar phase was seen by MRI. By resorting to DTI, information about structural anisotropy beyond the MRI spatial resolution limit could be obtained at length scales down to tens of μm. Inside the PR domains, and along the extrusion flow direction, diffusion appears predominantly anisotropic, in contrast to the nearly isotropic water diffusion within the WR domains.

Conclusion: In this work, we have shown how MRI could be used to quantify structural anisotropy of plant-based protein extrudates at length scales from tens of μm to sub-mm. For deadstop extrudate samples, it was observed that, upon entering the cooling die, the hot protein melt cools and solidifies, into anisotropic lamellae, dominantly in the regions close to the walls of the die. Complementary use of DR and SANS methods have shown a similar anisotropic structure development, respectively, at the μm- and nm-scale. Therefore, MRI is a powerful technique to underpin current hypotheses on shear- and temperature-induced phase separation of plant-proteins, and to provide the experimental data required to validate current *in silico* modelling efforts. Ongoing work is targeting the application of flow-MRI to study HME *in situ* using a benchtop-scale extruder.

References: [1] Van der Sman & Van der Goot, Curr. Res. Nutr. Food Sci. (2023). [2] Schreuders *et al.,* Food Control. (2024). [3] Ranasinghesagara et al., J. Food Sci. (2009). [4] Garina *et al.,* Food Hydrocoll. (2024). [5] Gobes *et al.,* submitted (2025). [6] Kingsley, Concepts Magn. Reason. A: Bridg. Educ. Res. (2006). [7] Mayar *et al.,* Food Struct. (2023).

Low field biological *J*-coupling spectroscopy

Gonzalo G Rodriguez[1,2 †], Charlotte von Petersdorff-Campen[1,2 †], Sergey Korchak[1,2 †], Oscar Sucre[1,2], Maria D Santi[1,2], Josef Elsaßer[1,2], Ruhuai Mei[1,2], Lisa M Fries[1,2], Jan Felger[1,2], Stefan Glöggler[1,2]

[1]NMR Signal Enhancement Group, Max Planck Institute for Multidisciplinary Sciences, Göttingen, Germany.
[2]Center for Biostructural Imaging of Neurodegeneration, University Medical Center Göttingen, Göttigen, Germany.

Introduction: Low-field NMR spectroscopy offers advantages for studying cells metabolism in their native environment. This is especially relevant for in-vitro studies, where low-field NMR could be used to analyze biological samples with reduced equipment size and cost, potentially benchtop research. However, the study of cellular metabolism at low, milli-Tesla, magnetic fields remains an unsolved problem. In this work, we tackle this problem by combining J-coupling spectroscopy [1] and parahydrogen-induced polarization (PHIP) [2] with our multinuclear scanner built in-house.

Methods: We developed and optimized the following steps: **1)** The PHIP protocol for providing biologically compatible [2-^{13}C] pyruvate. **2)** The design and in-house construction of a multinuclear low-field NMR spectrometer with B_0 = 0.066 T, a triple-nuclear RF coil for ^{1}H, ^{13}C and ^{23}Na channels, and five shimming. **3)** The fingerprinting matching method for quantifying the pyruvate and lactate concentration. **4)** The validation of the methodology by measuring synthetic enzymatic pyruvate-to-lactate conversion. Finally, we measure metabolism in PanC02 cancer cells for three different pyruvate and lactate concentrations.

Results and discussion: Fig. 1 shows a summary of the main results obtained from our work. This includes the implementation of strong J-couplings for [2-^{13}C] lactate that allow the differentiation with pyruvate at low magnetic fields, the optimization of a PHIP protocol that provides biocompatible [2-^{13}C] pyruvate with signal enhancements of 20,000 that facilitates its detection at low magnetic fields, and the multinuclear low-field NMR spectrometer developed in-house (top section of Fig. 2). Finally, the right box of Fig. 1 shows a pyruvate-to-lactate conversion measured at 0.066 T for PanC02 cancer cells. The pyruvate + lactate peak can be differentiated from the lactate peak, allowing for concentration quantification. Thus, we implemented a fingerprinting matching method to determine the pyruvate concentration and magnetic field homogeneity. The estimated ΔB_0 = 35 Hz describes the observed line broadening. The correlation of 0.9682 shows a good agreement between the simulated and acquired spectra.

Conclusion: Our results represent the first time that a J-coupling spectroscopy is implemented in biological samples at low magnetic fields. The differentiation of the pyruvate and lactate demonstrated that is possible to study metabolism in milli-Tesla fields.

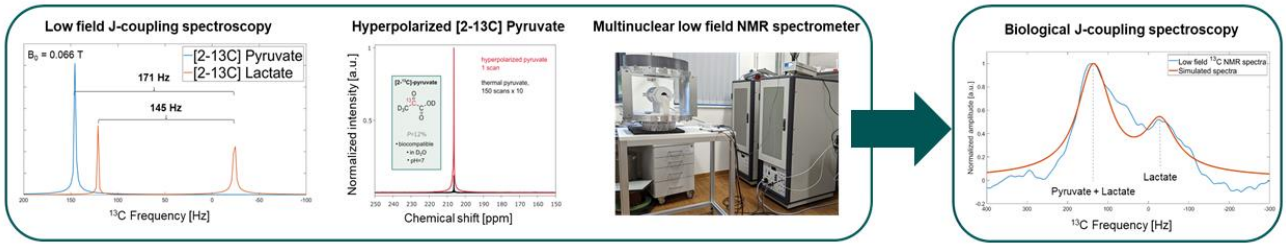

Fig. 1: The simulated pyruvate and lactate spectra at 0.066 T and ΔB_0 = 0 Hz are shown in the left. This was combined with a PHIP protocol optimized to provide a biocompatible solution with 20,000-fold signal enhancement middle. Additionally, we developed a multinuclear low-field NMR spectrometer in-house to be able to acquire the data. This includes the main magnet, shimming and RF coils (right image). Finally, we measured the pyruvate and lactate spectra in PanC02 cancer cells and calculated the pyruvate concentration and field inhomogeneity through fingerprinting matching (right box).

References: [1] Appelt, Pys. Rev. A (2010). [2] Hovener, Angew. Chem. Int. Ed. Engl. (2018).

Book of Abstracts

ICMRM '25

Scientific Session 8

Engineering & Solid-State

Imaging a sample spinning at 30 kHz and more: A new horizon for solid-state MRI

V. Sarou-Kanian, F. Fayon
CNRS, Université d'Orléans, CEMHTI, UPR 3079, Orléans, France

Introduction: Fifty years after its proof of concept [1], magnetic resonance imaging has become a gold standard technique to produce high quality images of water in soft tissues. Even today, thousands of scientific articles involving MRI are published annually, and a significant part of them are related to new methodologies (hardware, sources of contrast, metabolism, acquisition schemes and data processing) showing the vitality of this field of research. At the same time, there are far fewer publications on MRI of solids (less than a thousand), but not because of a lack of interest. Indeed, the anisotropic NMR interactions (dipolar, quadrupolar, chemical shift) that remain in the solid state are responsible for very short transverse relaxation times and strong line broadening which are deleterious for sensitivity and spatial resolution. Several strategies for MRI of solids have been proposed [2], but the current methods consist in encoding the k-space as soon as possible with strong magnetic field gradients [3]. Another approach directly derived from solid-state NMR spectroscopy is the well-known magic angle spinning (MAS) technique leading to narrowed lines and increased relaxation times, hence enhancing the sensitivity and the spatial resolution. As the object of interest is rotating, synchronization of the spatial encoding direction is performed by generating oscillating gradient shapes from a 3D axis system. This method has proved relevant capabilities for MRI of solids for moderate MAS frequencies (10 kHz) [4]. For materials with strongly coupled spin systems (homonuclear dipolar or quadrupolar couplings), it is necessary to spin the sample at very fast MAS frequencies (>30 kHz). Unfortunately, the induction of the gradient coil makes it very difficult to generate accurate oscillating gradients. In this work, we demonstrate that it also possible to obtain well-resolved images of solids at very fast MAS frequencies using simply a steady gradient. To this end, the implementation of a multiple-pulse sequence is required to sample the k-space similarly to standard MRI. This new methodology is illustrated experimentally with different solids samples exhibiting strong couplings (e.g. 1H-1H). We also focus that it gives an opportunity to convert your NMR spectrometer in a MRI scanner for free.

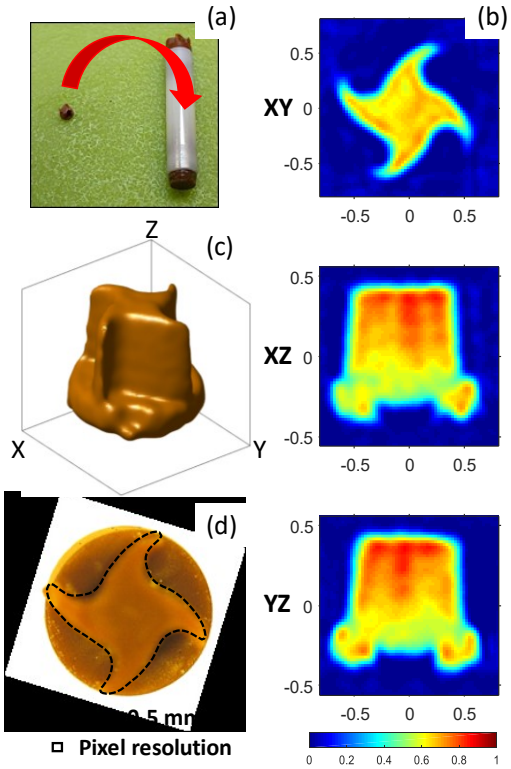

(a) Picture of a 1.3 mm drive cap before its wedging inside a 2.5 mm MAS rotor. (b) Three orthogonal slices (XY, XZ, YZ) in the rotor frame of the 1.3 mm drive cap obtained at a **spinning frequency 30 kHz**, and using the MAS-MRI-SF2 sequence (N = 12, I = 24). FOV(ZXY) = 1.1×1.6×1.6 mm^3 ; **spatial resolution (ZXY) = 50×84×84 µm^3**; scale in mm. (c) 3D isosurface of the drive cap (isosurface level = 40%). (d) Top view of the drive cap.

References:
[1] Lauterbur P.C., Nature (1973) 242:190.
[2] Demco, D.E. and Blümich, B., Concepts Magn. Reson., (2000) 12:188&269.
[3] Weiger M., Pruessmann K.P., Prog. Nucl. Magn. Reson. Spect., (2019) 114–115:237.
[4] Yon M., Sarou-Kanian V., Scheler U., Bouler J.-M., Bujoli B., Massiot D., Fayon F., Sci. Rep. (2017) 7:8224.

Crystal Structure, Particle Size, and Ionic Conductivity of Solid-State Electrolytes Studied By Diffusion and Relaxation NMR

S.Mailhiot[a,b], P.Molaiyan[b], A. Kantola [b],V-V. Telkki [b]
[a]Bruker Biospin GmbH, Ettlingen, Germany, [b]University of Oulu, Oulu, Finland

Introduction: Development of new sustainable technologies relies on the development of safer, low cost, and higher energy density batteries, such as all solid-state batteries. In all solid-state batteries, ions migrate from anode to cathode through defects in the crystal structure of the solid-state electrolyte. Diffusion based NMR measurements are a powerful tool for non-invasively characterizing this migration in the crystal structure and across grain boundaries. Diffusion derived from NMR measurements is correlated with electrical conductivity while diffusion measurements as a function of temperature and observation time allow for the measurement of activation energy and mean squared displacement respectively. Relaxation measurements give insight into motion on the atomic scale. In this work, migration of Li in two solid-state electrolyte materials is characterized, cubic Li_6PS_5Cl [1] and monoclinic Li_3InCl_6 [2]. The NMR data is complemented by scanning electroscope microscopy, x-ray diffraction, and electrical impedance spectroscopy to understand the effect of impurities, crystal structure, and grain boundaries on ion migration.

Methods: The powder samples of Li_6PS_5Cl and Li_3InCl_6 in an Argon atmosphere were sealed in 5 mm glass NMR tubes. NMR Measurements, measuring D, T_2, T_1, D-T_2, and T_2-T_2, were acquired using 9.39 and 14.1 T Bruker spectrometers equipped with 5 mm Diffusion Broadband Probes with a maximum gradient strength of 17.4 Tm^{-1} and 28 Tm^{-1}. Data was acquired from -60 to 180°C.

Results and Discussion: To test the effect of defects in the crystal structure on ion migration, which includes ion hopping and long-range motion, monoclinic Li_3InCl_6 was studied before and after annealing. After annealing, the sample showed traces of impurities and larger lattice spacing than before annealing in XRD data. R_2 relaxation rates were faster in the annealed sample, indicating an increased hopping rate of Li between atomic sites in the crystal lattice, due to this increased lattice spacing. $D(T)$ also showed faster diffusion and a smaller activation in the annealed sample, indicating faster long-range motion and improved ion conductivity. To compare the effect of crystal structure, the diffusion in cubic Li_6PS_5Cl Li_3InCl_6 studied. $D(T)$ was faster and had a smaller activation energy in cubic Li_6PS_5Cl than in monoclinic Li_3InCl_6, which corresponds to an improved electrical conductivity, which was confirmed using impedance spectroscopy.

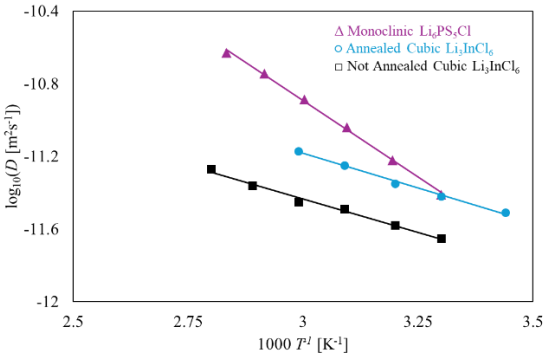

Conclusion: Relaxation and diffusion NMR are powerful tools for measuring the ion motion in solid-state electrolytes that give insight into short range motion and long-range motion. The motion of Li is a key determinant of electrolyte performance.

References: [1] Schlenker, Chem. Mat. (2020). [2] Molaiyan, Mat &. Des. (2023).

Boosting resolution and sensitivity for operando studies of catalytic processes

E.S. Kononenko[a,b], I.V. Skovpin[a], D.B. Burueva[a], V.N. Rogozhnikov,[c] L.M. Kovtunova[c], I.V. Koptyug[a]
[a]International Tomography Center SB RAS, [b]Novosibirsk State University, [c]Boreskov Institute of Catalysis SB RAS, Novosibirsk, Russia

Introduction: In addition to the notorious sensitivity problem, magnetic resonance (MR) studies of heterogeneous objects suffer from a dramatic degradation of spectral resolution. This is particularly true about the studies of heterogeneous catalytic processes in operating reactors, with multiple gas-liquid-solid interfaces leading to a severe distortion of the applied magnetic field. An efficient solution to this problem required to fully utilize the power of the MR toolkit in the operando studies of catalytic reactors at an entirely new level is still lacking.

Methods: Our approach is based on the use of hollow spherical catalyst support particles. Their geometry and a reduced solid phase content largely improve magnetic field homogeneity, both in their interior and in the interparticle voids. The use of a granular bed of hollow alumina spheres ca. 2-3 mm in diameter with a 50 micron thick shell is shown to provide a significantly improved spectral resolution and image quality for liquids and gases within the bed.

Results and discussion: The linewidth of ^{1}H NMR signals of fluids in an NMR tube filled with hollow alumina spheres was reduced by more than 10-fold compared to fluids in ordinary granular beds [1] (Fig. 1a). Next, catalyst particles comprising rhodium nanoparticles supported on hollow alumina spheres were synthesized and tested in propylene hydrogenation, clearly demonstrating their advantages in terms of achievable resolution and sensitivity in operando MR studies of a catalytic process. MR images and spatially resolved NMR spectra clearly visualized the distribution of propylene (reactant) and propane (product) along the catalyst bed. Furthermore, the high spectral resolution achieved prevented the self-cancelation of absorption/emission NMR multiplets when parahydrogen instead of normal H_2 was used for NMR signal enhancement (Fig. 1b).

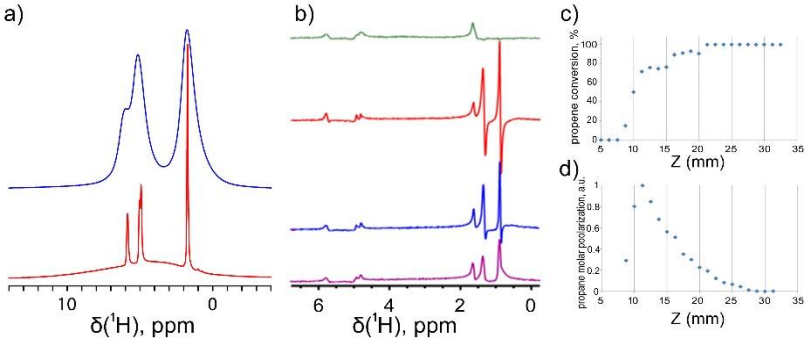

Fig. 1. (a) ^{1}H NMR spectra of propylene gas in a bed of ordinary (blue) and hollow alumina beads (red). (b) ^{1}H NMR spectra acquired during hydrogenation of propylene with parahydrogen with spatial resolution along the Rh/hollow-Al_2O_3 bed; the gas mixture is suppled from the top. (c) Propylene conversion and (d) propane molar polarization spatially resolved along the catalyst bed.

Conclusion: The use of hollow catalyst support particles opens the door for advanced operando studies of heterogeneous catalytic processes, providing sufficient spectroscopic and spatial resolution to monitor the distribution of reactants and products in the fluid phase of the reacting medium (Fig. 1c). Furthermore, the buildup and decay of parahydrogen-induced polarization within an operating catalyst layer was for the first time visualized with spatial resolution (Fig. 1d), providing the means for chemical engineering level optimization of a heterogeneous reactor to efficiently produce liquids and gases with the maximized molar hyperpolarization for a variety of applications.

This work was financially supported by RSF (grant #25-13-00053).

References: [1] Kononenko, Skovpin, Burueva, Rogozhnikov, Shefer, Salanov, Koptyug, Anal. Chem. (under review).

Large scale MRI for imaging of processes

S. Benders[1], T. Lenczyk[1], M. Özdemir[1], A. Penn[1]
[1]Institute of Process Imaging, Hamburg University of Technology, Hamburg, Germany

Introduction: Process engineering plays a pivotal role in the production of many essential goods. Therefore, increasing the understanding of the underlying processes is crucial. Conventionally, this has been achieved through integral measurements and modelling. The use of tomographic techniques, especially Magnetic Resonance Imaging (MRI), can provide spatially resolved maps of many relevant parameters. While there has been significant work on process engineering problems recently, most of the work focuses on small lab-scale systems. Yet, many processes are large-scale and rely on gravity and the limitations posed by small-bore vertical or large-bore horizontal MRI magnets can significantly constrain research efforts in these areas.

System: To address these challenges, Hamburg University of Technology has introduced a vertical MRI system. This cryogen-free system boasts a field strength of 3 Tesla, a usable bore diameter of 40 cm, and is specifically designed to accommodate samples up to 3 meters in height. It can be equipped with tailor-made receive arrays, enabling the use of advanced acceleration techniques such as parallel imaging.

Fig. 1: The TUHH vertical MRI magnet.

Results and Discussion: This unique system enables the examination of significant process engineering systems, such as fluidized beds, trickle beds and stirred tank reactors in relevant scales. External devices such as motors and shakers can be placed in line with the experiment. Measurements of fluidized beds (with up to 30 cm diameter) and stirred-tank reactors reveal the possibility to observe process-relevant parameters such as flow and bubble sizes in these systems.

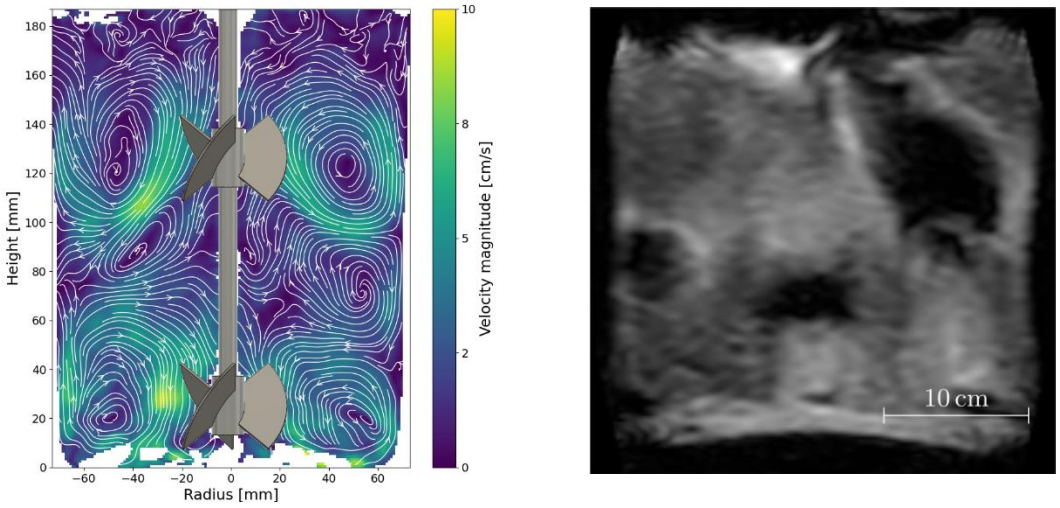

Fig. 2: Left: Flow measurement of a stirred tank reactors (130 mm diameter), Right: Measurement of a fluidized bed (300 mm diameter).

Conclusion: The TUHH MRI system allows for the exploration of process engineering systems on a larger scale than previously possible. Initial experiments across various systems demonstrate the potential to deliver valuable measurement parameters that can enhance process efficiency and effectiveness.

Radiofrequency Receive Coil Arrays for Large-Bore Vertical 3T MRI in Process Engineering

M. Adrian[a], *A. Tsanda*[a,b], *S. Benders*[a], *T. Knopp*[a,b], *A. Penn*[a]
[a]Hamburg University of Technology, Hamburg, Germany
[b]University Medical Center Hamburg-Eppendorf, Hamburg, Germany

Introduction: Magnetic resonance imaging (MRI) has become a powerful modality for the non-invasive characterization of dynamic processes in bio-/chemical engineering [1]. To expand the capabilities of our world-wide unique vertical 3 Tesla MRI system, we developed a modular suite of radiofrequency (RF) receive coil arrays with 1-, 5-, and 32-channel configurations, each optimized for different imaging objectives. Unlike traditional horizontal MRI systems, the vertical large-bore design supports upright experimental setups and large-scale imaging of pilot-scale reactors, enabling studies of flow, mixing, and reactions under realistic process conditions. Rather than pursuing a single highest-performance array, we implemented a purpose-driven approach balancing spatial/temporal resolution, field-of-view (FOV), and operational simplicity [2, 3].

Methods: The receive arrays were constructed using low-loss copper conductors on thin 3D-printed scaffolds, conforming to sample geometries. Geometric overlap minimized mutual inductance between adjacent coil elements. Active detuning circuits and low-input-impedance preamplifiers enhanced sensitivity and minimized noise. Finite element modeling (COMSOL Multiphysics) guided the coil layout to reduce inter-coil coupling, critical for high parallel imaging performance. RF bench testing validated tuning, matching, and decoupling, with S-parameter isolation levels of at least -20 dB at the operating frequency of 127.8 MHz.

Results and discussion: The arrays enabled imaging of liquids inside structured packings with Schwarz-Diamond triply periodic surface (TPSf) geometries. The 1-channel array delivered uniform sensitivity and high spatial resolution for fine structural imaging in small columns. The 5-channel array offered a balance between resolution and speed for larger setups. The 32-channel array leveraged parallel imaging for rapid 3D acquisition, improving signal-to-noise ratio (SNR) and reducing scan times. This configuration facilitated real-time imaging of flow dynamics in large reactor columns, demonstrating the advantage of tailoring array design to experimental goals and sample scales.

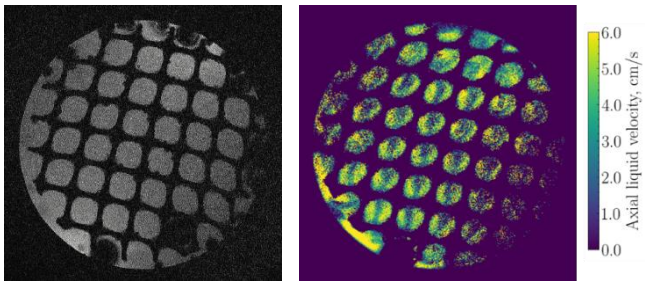

Fig. 1: (Left) MRI of DN 40 TPSf structured packing using 1-channel receive coil, with spatial resolution of 0.1 mm x 0.1 mm x 0.3 mm and temporal resolution of 60 s. (Right) MRI-based velocity mapping of the same packing at Reynolds number of 990, with spatial resolution of 0.1 mm x 0.1 mm x 1 mm and temporal resolution of 18.1 s.

Conclusion: The 1-, 5-, and 32-channel RF receive arrays significantly expand the practical utility of MRI in process engineering. By balancing resolution, FOV, and operational flexibility, this approach supports diverse applications from detailed structural imaging to real-time flow monitoring. Future work will focus on further enhancing performance, modularity, and usability of the RF receive coil arrays.

References: [1] Gladden, Annual Review of Chemical and Biomolecular Engineering. (2017). [2] Roemer, Magnetic Resonance in Medicine. (1990). [3] Wiesinger, Magnetic Resonance in Medicine. (2004).

Magnetic Resonance Imaging of Structured Packings: Overcoming Spatial, Signal, and Geometric Challenges

H. Rennebaum[a], A. Dobschall[a], S. Benders[a], M. Skiborowski[a], A. Penn[a]
[a]Hamburg University of Technology, Hamburg, Germany

Introduction: Structured packings are widely employed in trickle beds to improve the mass transfer between the liquid and gas phases in absorption and distillation processes. While integral experiments, such as pressure drop measurements and collector experiments, offer overall insights, they lack spatial and temporal detail on liquid distribution. Magnetic Resonance Imaging (MRI) overcomes this by providing resolved flow visualization, though its application is challenged by low liquid content, the need for high temporal resolution, and difficulty achieving spatial resolution on the order of hundreds of micrometers with large-bore scanners [1]. These issues are mitigated through optimized imaging sequences, doped aqueous solutions, and tailored radiofrequency coils, enabling MRI to deliver detailed insights into liquid behavior and packing efficiency.

Methods: All experiments were conducted with a 3 Tesla vertical large-bore MRI system with the ability to measure samples with a height of several meters. The trickle bed included a one meter structured packing bed with a diameter of 54 mm. 3D-printed corrugated sheet packings (480 m^2/m^3) were studied under varying gas and liquid loadings. To shorten T_1 relaxation time to 50 ms and match the magnetic susceptibility of the gas phase, which is air, the aqueous solution was doped with 16.27 mM dysprosium(III) nitrate and 1 mM gadolinium(III) chloride. The liquid distribution was measured using a gradient echo imaging sequence. Two coil designs were compared, the system-integrated Transmit - Receive bird cage body coil and a tailored single-channel surface coil.

Results and discussion: The coils were compared with regard to signal-to-noise ratio (SNR) and spatiotemporal resolution. Unlike the body coil, which suffers from low spatial resolution and long acquisition times, the single-channel coil enables significantly higher spatiotemporal resolution (Fig. 1). The shortened T_1 relaxation times allow faster signal recovery, enabling higher temporal resolution. Using a single-channel coil, doped aqueous solution, and gradient echo sequence enables MRI with spatial resolution up to 0.25 × 0.25 × 0.3 mm^3. Combining data from partially and fully filled packings (Fig. 1) enables differentiation of liquid, gas, and structured packing, allowing the determination of the gas-liquid interfacial area, which is critical for the separation efficiency. MRI-derived maldistribution factors were validated against collector experiments at the column bottom, demonstrating good agreement.

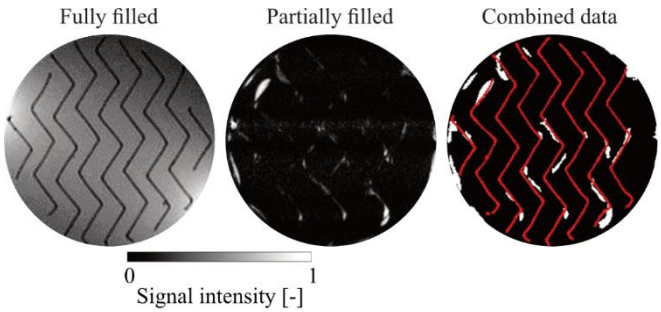

Fig. 1: MRI measurements are conducted with a spatial resolution of 0.5 × 0.5 × 1 mm^3 with a temporal resolution of 1.4 sec per frame. The combined data consider the information of the fully filled and partially filled bed enabling to differentiate between packing (red), air (black), and aqueous solution (white).

Conclusion: This study shows the use of MRI for temporally and spatially resolved measurements of liquid distribution in structured packings within trickle beds. A tailored surface coil, doped aqueous solutions, and optimized imaging enabled high-resolution imaging. MRI allows to distinguish between gas, liquid, and packing phases, enabling the determination of the gas–liquid interfacial area. The comparison with collector experiments showed good agreement, with MRI offering enhanced insight along the column height and improved radial resolution.

References: [1] Hampel et al., *Sensors* (2022).

Book of Abstracts

ICMRM '25

Scientific Session 9

Microscopy & Cellular

Deep Learning–Based Compressed Sensing Reconstruction for High-Resolution MRI of Human Embryos

A. Kazuma Iwazaki[1], *B. Naoto Fujita*[1], *C. Shigehito Yamada*[2], *D. Yasuhiko Terada*[1]
[1]University of Tsukuba, Tsukuba, Japan, [2]University of Kyoto, kyoto, Japan

Introduction: Magnetic resonance microscopy (MRM) enables non-invasive visualization of tissue microstructures and is widely used for morphological analysis of fixed human embryo specimens [1]. However, high spatial resolution imaging typically requires prolonged acquisition times. In 2023, MRM with an isotropic resolution of (10 μm)³ was achieved [2] using compressed sensing (CS) [3] with an acceleration factor of 2 (AF=2), although the scan still required approximately 12 days. Recently, deep learning (DL)–based reconstruction methods have shown superior performance over conventional CS. Among these, zero-shot self-supervised learning (ZS-SSL) [4], which requires no external training data, is particularly promising for human embryo imaging, where the availability of annotated datasets is limited. This study aims to further accelerate high-resolution MRM of human embryos by applying ZS-SSL while preserving spatial resolution.

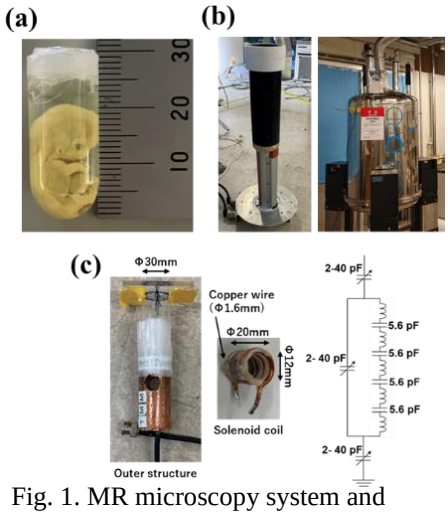

Fig. 1. MR microscopy system and embryo specimen.(a) Human embryo specimen at Carnegie stage 21 embedded in agarose gel.(b) Gradient coil and 9.4 T vertical superconducting magnet.(c) home-made RF coil and resonance circuit.

Methods: A human embryo at Carnegie stage 21 (Fig. 1(a)) was embedded in 1% agarose gel within a 12 mm-diameter test tube. Imaging was performed using a Bruker micro2.5 gradient system and a 9.4 T vertical superconducting magnet (Fig. 1(b)). A home-made RF coil was used (Fig. 1(c)). Imaging was conducted using a steady-state free precession free induction decay (SSFP-FID)–based three-dimensional gradient echo sequence with the following parameters: TR/TE=100/5 ms, flip angle=70°, FOV=1.9×1.28×1.28 cm³, and matrix size=1000×640×640, yielding an isotropic resolution of (20 μm)³. The number of excitations (NEX) was set to 24, and the total scan time was approximately 68 hours. ZS-SSL was re-implemented in PyTorch based on the method proposed by Yaman et al., using a MoDL-based architecture with a 5-layer ResNet. The learning rate was set to 5×10^{-4}, and early stopping was applied if the validation loss did not improve for 20 consecutive epochs.

Results and discussion: The reconstructed image of the accessory nerve (~100 μm in diameter) is shown in Fig. 2(b). For reference, Fig. 2(a) shows the corresponding structure in a histological section from a different embryo specimen at the same developmental stage. In the ZS-SSL reconstructed image, the accessory nerve was clearly visualized and could be distinguished from the surrounding tissue.

Conclusion: These results demonstrate that high-resolution imaging at AF=4 is feasible using ZS-SSL, achieving a fourfold acceleration without significant degradation of image quality. ZS-SSL is thus a practical and effective method for fast, high-resolution imaging of human embryos.

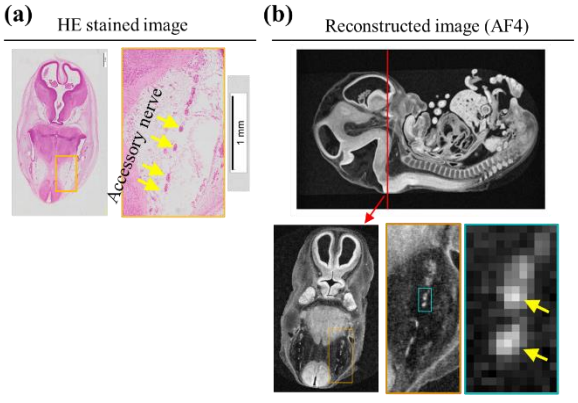

Fig. 2. Magnified images of the accessory nerve. (a) HE-stained image of a human embryo at Carnegie stage 21, used for comparison. (b) ZS-SSL reconstructed image at AF=4, showing clear visualization of the accessory nerve.

References: [1] K. Kose, Anat. Rec., 301, (2018).
[2] K. Makihara et al., J. Magn. Reson., 355, (2023).
[3] M. Lustig et al., Magn. Reson. Med., 58, (2007). [4] B. Yaman et al., Proc. ICLR, (2022).

Dynamic Magnetic Resonance Sampling Pattern Guided by Deep Reconstruction

Zaimin Zhu[a], Fangrong Zong[a]
[a]School of Artificial Intelligence, Beijing University of Posts and Telecommunications, Beijing, China.

Introduction: K-space undersampling is a primary method for reducing MRI scan time. Existing undersampling techniques typically rely on predefined static sampling patterns [1,2], neglecting inter-individual anatomical variations. This study introduces a deep learning-guided (DL-guided) sampling pattern which dynamically determine the k-lines to be sampled during the 3D k-space sampling process.

Methods: Figure 1 shows the proposed approach: k-space is progressively filled over multiple scans using a 3D EPI sequence, with the k-lines to be acquired in each scan determined by the already collected data. During the first scan, 10% of the k-lines are randomly chosen according to a Gaussian distribution. After each scan, the undersampled image is zero-padded and input into a U-Net model to predict the fully sampled image. The residual image between the undersampled and predicted fully sampled images is transformed into k-space residuals via Fourier transform. The 10% of k-lines with the largest absolute residuals in unsampled regions are acquired in the next scan.

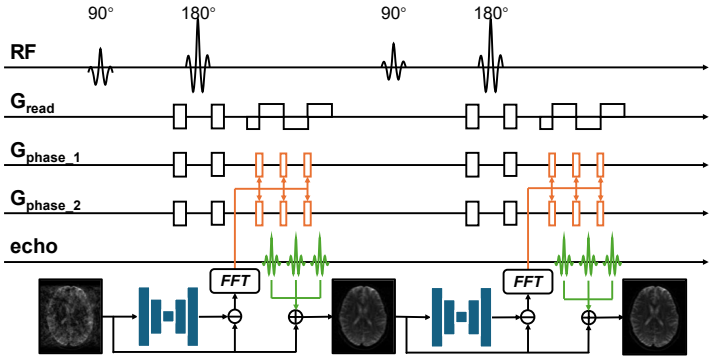

Fig. 1. The training framework of DL-guided sampling pattern.

Results and dissemination: The effectiveness of the proposed method was validated through simulations on the Human Connectome Project (HCP) dataset [3]. As shown in Figure 1, at low sampling rates, the DL-guided sampling pattern significantly outperforms fixed sampling patterns generated by Gaussian or uniform distributions in terms of reconstruction quality. Figure 2 illustrates the images obtained using the DL-guided pattern and the Gaussian pattern at different sampling rates. Notably, the DL-guided pattern achieves image quality comparable to that of a 40% Gaussian pattern even at a 20% sampling rate.

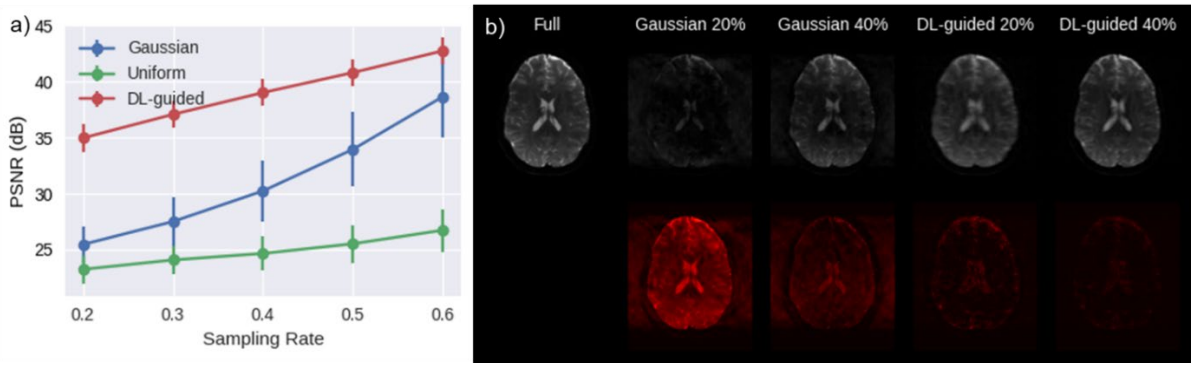

Fig. 2. a) The variation of reconstruction accuracy with sampling rate under different sampling pattern; b) MRI acquired with at different patterns and sampling rates

Conclusion: This study presents a deep learning-guided k-space undersampling method that enables accurate imaging at low sampling rates.

References: [1] Levine E., IEEE Trans Med Imaging(2017). [2] Sherry, F., IEEE Trans Med Imaging(2020). [3] Van Essen, D. C., Neuroimage(2013).

Acknowledgement: This work was supported by the National Natural Science Foundation of China (No. 82371910).

Optical Widefield Nuclear Magnetic Resonance Microscopy

J. C. Draeger[1], K. D. Briegel[1], X. Chen[1], N. R. von Grafenstein[1], P. Blümler[2], R. D. Allert[1], D. B. Bucher[1]
[1]Technical University of Munich, Munich, Germany, [2]University of Mainz, Mainz, Germany

Optical nuclear Magnetic Resonance Microscopy (OMRM) bridges the gap between magnetic resonance imaging (MRI) and optical microscopy by using nitrogen-vacancy (NV) centers in diamond to transcode nuclear magnetic resonance (NMR) signals into camera-detectable fluorescence signals [1]. Unlike conventional MRI, which requires magnetic field gradients for spatial encoding, OMRM enables direct, real-space NMR imaging over a wide field of view. In our approach, NV centers are optically initialized and read out, while microwave (MW) pulses control their spin states to couple them to external ^{1}H NMR signals [2]. These signals are excited using radiofrequency (RF) coils and detected via a high-speed camera (Fig. 1 a-c). The system incorporates a custom-designed microfluidic chip [3], integrated MW and RF components [4], and a highly homogeneous permanent magnet (Fig. 1 d). Using this setup and applying the Coherently Averaged Synchronized Readout (CASR) protocol, we achieved widefield imaging of water protons with a spatial resolution of approximately 10 µm across a field of view of ~235 × 150 µm², with each camera pixel capturing multicompnent NMR data (Fig. 1 e-f), allowing the analysis of amplitude, frequency, phase, and linewidth [1]. OMRM combines the strengths of optical imaging with the molecular specificity of NMR spectroscopy, opening new possibilities for a wide range of applications in the physical and life sciences. These applications include imaging metabolic activity in single cells or tissue slices, analyzing battery materials, and facilitating high-throughput NMR analysis.

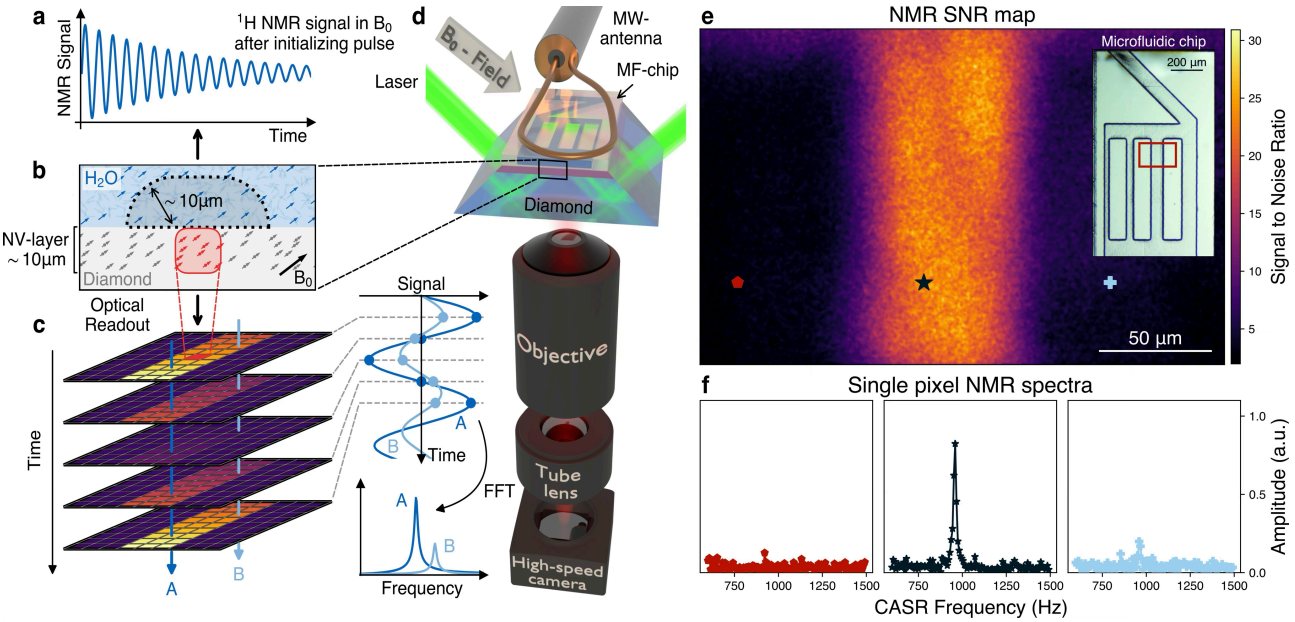

Fig. 1: Nuclear magnetic resonance (NMR) signals (a) are detected optically using a diamond containing a 10 µm layer of nitrogen-vacancy (NV) centers (b). These signals are imaged with a high-speed streaming camera where each pixel time trace corresponds to a location on the diamond and can be fast Fourier transformed (FFT) individually into frequency spectra (c,e,f). The experimental setup consists of the NV diamond, attached to a microfluidic structure, a microwave antenna and an objective with a tube lens to image the fluorescence onto a high-speed streaming camera sensor. The probehead is positioned inside a permanent magnet at ~84 mT (d).

References: [1] Briegel, Nat. Commun. (2025). [2] Degen, Rev. Mod. Phys. (2017). [3] Allert Lab. Chip. (2022). [4] Bucher, Nat Protoc. (2019).

Ultra-high field MRI and spatially resolved spectroscopy of organoids at 28.2 T

T. Nikolaeva[1], J.S. Hennink[2], R. Singer[3], C. Jakobs[1], R.J. Pasterkamp[1], A.H. Velders[2], C.M.W. Tax[1], J.R. Krug[2]**

[1]University Medical Center Utrecht, Utrecht, The Netherlands, [2]Wageningen University & Research, Wageningen, The Netherlands, [3]University of Strasbourg, Strasbourg, France

Introduction: Organoids, 3D cell cultures mimicking organs, are an interesting platform to study disease mechanisms and have the potential to partially mitigate the need for animal testing. Currently, light microscopy methods and electron microscopy are predominantly used to study the structure of organoids [1]. Magnetic resonance imaging and spatially resolved spectroscopy can complement microscopy techniques and provide translatable insights for clinical imaging and diagnosis. Due to the small size of organoids <3mm, high signal-to-noise ratios (SNR) are needed to obtain high-resolution images or localized spectra from small volumes of interest. High SNR values can be obtained by using ultra-high field strengths, such as a 28.2 T NMR spectrometer equipped with a microimaging probe (Fig.1a). Previously, we have demonstrated the feasibility of high-resolution organoid MRI towards structural imaging, diffusion imaging and localized spectroscopy [2-3]. Here, we show that very high-resolution diffusion MRI experiments with isotropic voxel sizes below 20 µm are feasible and compare the metabolite profile using single-voxel spectroscopy with and without adiabatic pulses.

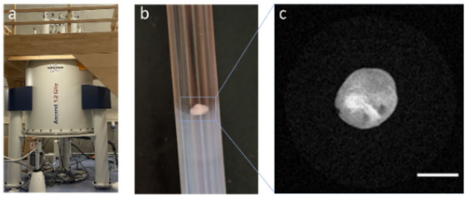

Fig. 1a. 28.2 T system. b. Organoid specimen atop a layer of agarose gel. c. 2D diffusion-weighted image (PSGE, slice thickness 0.1 mm) of a cross-section across the organoid. The scale bar represents 1 mm.

Methods: Organoid specimens: Cortical organoids (DIV55-110 [4]) were positioned in 3 and 5 mm tubes atop a layer of agar and suspended in medium (Fig 1b). MRI system: Experiments were performed on a 28.2 T magnet equipped with an Avance Neo console, a microimaging probe (Iprobe: coil diameter 5mm, 3T/m gradient set), ParaVision 360 V3.3, all Bruker, Ettlingen, Germany). The temperature was controlled at 310K. High-resolution diffusion MRI experiments: PGSE EPI 3D, voxel size 19.5x19.5x19.5µm^3, Δ 2.7ms, δ 0.9ms, 9 directions, repetition time 3.8s, echo time 9.4ms, 8 segments, 2 repetitions, b 0.1 and 1.0ms/µm^2, experiment time 21h 37min. Localized spectroscopy: sLASER/PRESS, TR 2s, TE 11.8ms(sLASER)/8.5ms(PRESS), voxel size (600µm)^3, water suppression - VAPOR, experiment time 34 min, working chemical shift 3 ppm.

Results and discussion: Diffusion-weighted images (Fig.1c) show variability in the internal structure of organoids. Using 3D PGSE EPI, an isotropic image resolution of (19.5 µm)^3 was obtained (Fig.2a). Mean diffusivity (MD) analysis confirmed spatial heterogeneity within the organoid (Fig.2a). Single-voxel spectroscopy was performed using sLASER to minimize the chemical shift displacement effect and was compared to PRESS (Fig.2b).

Conclusion: High-resolution imaging and localized spectroscopy of organoids are feasible. Further correlation with immunohistochemistry to determine structural heterogeneity and HR-MAS or MS to validate the metabolite composition is needed.

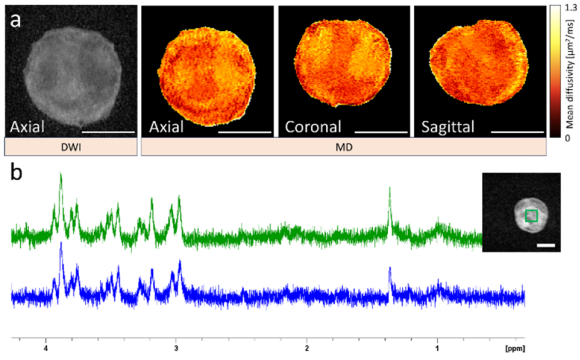

Fig. 2a. Diffusion-weighted image (DWI) and mean diffusivity (MD) maps of 3D PGSE EPI at a spatial resolution of (19.5µm)^3. For the MD analysis, a denoising protocol was used. b. sLASER (green) and PRESS (blue) spectra are shown. The voxel size and location are shown on a reference image. Scale bars represent 1 mm.

References: [1] Brémond Martin et al., Front Neurosci.(2021).[2] Krug et al., ESMRMB Proceedings (2024) [3] Nikolaeva et al. ICMRM (2025) [4] Yoon et al., Nat Methods (2019).

Refocused Acquisition of Chemical Exchange Transferred Excitation: Use of Phase in Exchange MRI

FT. Gutjahr[1], S. Mayer[1,2], J. Balling[1], F. Fidler[1,3], PM. Jakob[1]

[1]University of Wuerzburg, Germany, [2]Leibniz-Institute of Plant Genetics and Crop Plant Research, Gatersleben, Germany, [3]EZRT Fraunhofer IIS, Wuerzburg, Germany

Introduction: In 2018 we demonstrated RACETE[1] as an alternative to the CEST-approach for visualizing chemical exchange. Like CEST, RACETE can improve sensitivity by repeated transfer of magnetization. However unlike CEST, RACETE refocuses transferred excitation by exploiting the stimulated echo (STE) pathway, enabling a multitude of new possibilities[2] two of which are presented here.

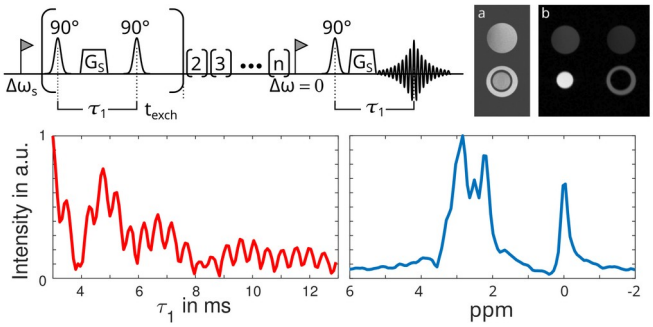

Figure 1: Top left: Sequence diagram, Top right: Phantom, a) TSE-Image b) RACETE image with separation of substances. Bottom: Absolute signal and corresponding spectrum using frequency labeled exchange.

In Fig. 1a the basic RACETE sequence diagram is shown. Two frequency-selective pulses are used to prepare an STE. During the first time interval (τ_1), a chemical shift-dependent phase is accumulated and an encoding encoding gradient (G_S) is applied. In the subsequent interval, all relevant magnetization is stored along the longitudinal axis, so no further phase is accumulated. This leads to a well-defined phase of the resulting stimulated echo, which can be read out on the water frequency after repeated excitation.

Methods/Results: Multi-substance RACETE using k-space dependent phase offsets: The phase of the RACETE signal can be controlled via the phase difference of the excitation pulse pair. By using a dual-band excitation, two pools can be excited simultaneously. Manipulating the excitation phase of one of the pools across phase steps allows shifting the corresponding image for one of the substances arbitrarily. This enables the separation of the simultaneously acquired two pool experiment similarly to a POMP experiment[3].

A vial containing salicylic acid (50 mmol/L) containing a smaller vial of Iomeprol solution (80 mmol/L) and another vial containing a mixture of both were imaged using a 17.5 T system. Fig.1a shows a spin-echo image, and Fig.1b presents the RACETE contrast with clear separation achieved using the approach described above.

Methods/Results: Measurement of exchange Spectra using frequency labeled exchange: When multiple substances with distinct chemical shifts are excited during preparation, each accumulates a unique phase during the τ_1-interval[4]. By varying this interval, a characteristic signal evolution is obtained. The resulting complex signal can then be directly transformed into a frequency spectrum representing the contributing exchanging species. In Fig 1. (bottom) both the signal and the corresponding spectrum of egg white (hen's egg), acquired on a 17.5 T system, are shown.

Conclusion: RACETE can generate true positive contrast chemical exchange contrast. The transfer of phase enables novel approaches for chemical exchange imaging.

References:[1] Gutjahr, ZMedPhys. (2019). [2] Zhao, MRI (2022). [3] Glover, JMR (1991). [4] Friedman, JACS (2010).

Book of Abstracts

ICMRM '25

Poster Sessions 1 & 2

A Highly Integrated HVNMR Spectrometer with AI-Driven Second-Order Shimming

Zhibin Zhao[1], Yitian Chen[1], Zhenghe Sun[1], Bernhard Blümich[2], Michal Kern[1], Jens Anders[1,3]

[1]Institute of Smart Sensors, University of Stuttgart, Germany

[2]RWTH Aachen

[3]Institute for Microelectronics Stuttgart (IMS CHIPS)

Magnetic field homogeneity is a fundamental requirement for high-resolution nuclear magnetic resonance (NMR) spectroscopy, particularly in compact systems where space constraints limit passive field correction methods. In this work, we present a highly integrated high-voltage NMR (HVNMR) spectrometer equipped with an AI-driven, second-order active shimming system. The system is designed to dynamically compensate for magnetic field inhomogeneities using bi-planar shim coils embedded directly into the core of a permanent magnet.

The shim coils are designed using a target field approach, with eight channels corresponding to the most relevant terms in the spherical harmonic field expansion of the used magnet. The coil structure is fabricated using laser-cut printed circuit boards (PCBs), and controlled via an FPGA-driven octal digital-to-analog converter (DAC) that powers five current drivers with a total power consumption of 6.5 W.

To speed the shimming process and make it more automated, we deploy a hybrid optimization algorithm on the FPGA. This algorithm combines a pre-trained neural network emulator – accelerated by a Xilinx Deep Processing Unit (DPU) – with actual measurement data to refine shimming performance using Gaussian process fitting. This edge-AI approach reduces optimization time by approximately 50% compared to conventional iterative search methods.

Experimental validation using acetic acid and distilled water samples demonstrates a significant improvement in spectral resolution. The full width at half maximum (FWHM) of the water sample is reduced from 32 ppm to 2.3 ppm, indicating a nearly tenfold enhancement in magnetic field homogeneity.

This work highlights the potential of integrating AI-based optimization into compact NMR systems, enabling faster and more efficient field shimming without compromising hardware footprint or energy efficiency.

A Portable 0.2 T Whole-body Magnetic Resonance Imaging System

[1]Linxin Chen, [1]Zaimin Zhu, [2]Huabing Liu, [2]Huaxue Liu, [2]Youwei Hou, [2]Mengyao Li, [2]Shuo Li, [3]Wenhui Yang, [3]Chengwei Lu, [1]Fangrong Zong*
[1]School of Artificial Intelligence, Beijing University of Posts and Telecommunications, Beijing, China
[2]Beijing Limecho Technology Co., Ltd, Beijing, China
[3]Institute of Electrical Engineering of the Chinese Academy of Sciences, Beijing, China

Introduction: Magnetic resonance imaging (MRI) is vital for neurological diagnosis [1], however, the high cost, large footprint, and infrastructure requirements of high-field systems constrain its availability in resource-limited settings [2]. To address this, we developed a compact, low-power 0.2 T portable whole-body MRI system suitable for point-of-care applications.

Methods: The system incorporates an open dual-column NdFeB permanent magnet (0.2 T, ± 5%) with passive and first-order active shimming, achieving a homogeneity of 47 ppm in a 200 mm DSV and stability within ≤ 10 ppm/h. Active thermal regulation maintains 28 ± 0.1 °C (Fig. 1.c). The gradient subsystem uses dual-planar compensated coils, delivering a maximum gradient strength of 46 mT/m and a slew rate of 40 T/m/s (Fig. 1.a). The RF system adopts a single-channel transmit-receive configuration based on a solenoid coil structure (Fig. 1.b). The system supports SE, FSE, and GRE sequences. Electromagnetic interference (EMI) is mitigated using copper mesh shielding. The system is powered by a lithium iron phosphate battery, is mobile within 500 m, and includes a manual patient table for flexible deployment.

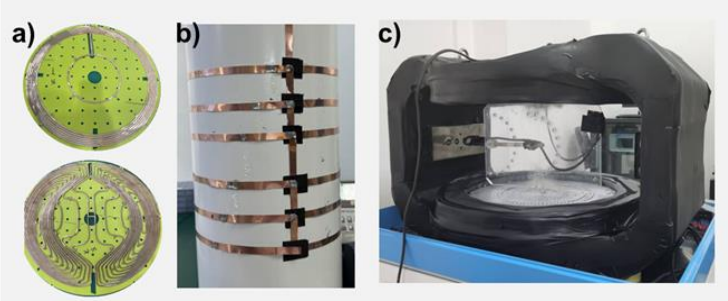

Fig. 1.a) Gradient coil; b) RF coil; c) Permanent magnet structure.

Results: A 3D GRE sequence (TR = 52 ms, TE = 13 ms) was used to acquire a brain image with a voxel size of 2.5 × 2.5 × 2.5 mm^3 (Fig. 2.a). A 2D SE sequence (TR = 0.5 s, TE = 30 ms) was used to image the hand and ankle, with a voxel size of 2 × 2 mm^2 (Fig. 2.b and Fig. 2.c). The images demonstrated good tissue contrast and structural clarity, validating imaging performance without RF shielding.

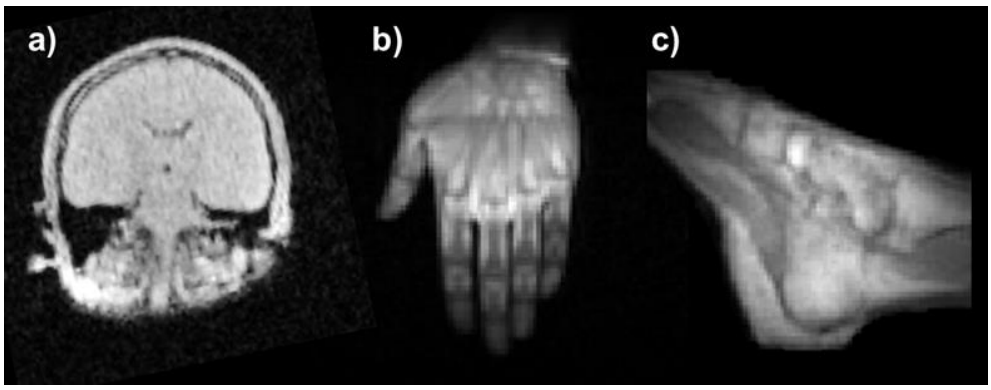

Fig. 2.a) 3D brain image using GRE; b) 2D hand image using SE; c) 2D Ankle image using SE.

Conclusion: We developed a portable 0.2 T whole-body MRI system for imaging in resource-limited settings. Preliminary evaluations demonstrated stable operation and feasible image acquisition. Future work will focus on EMI suppression and AI enhancement to support broader deployment.

References: [1] Ali et al., Artif. Intell. Rev. (2025). [2] Altaf et al., Front. Neuroimaging (2025).

Acknowledgement: This work was supported by the National Natural Science Foundation of China (No.82371910).

3D printing of magnetic filament for shimming permanent magnets

Andrew F. McDowell[1], Robert R. Lown[2]
[1]NuevoMR, LLC, Albuquerque, USA, [2]San Diego, USA

Introduction: Previously, we have successfully implemented magnetic ink to passively shim relatively high quality magnets.[1] However, the ink is not magnetically strong enough to shim simpler, cheaper magnets. We have found that 3D printing of magnetizable filament can achieve the required strong correction. For iron-core dipole magnets, the method can be effective in addressing the inhomogeneities that result from the finite pole diameter. For cylindrical Halbach arrays, the stronger corrections may all that is needed to address the inhomogeneities due to material property variations and the impact of the finite magnet length. For both types of magnets, more compact designs and simpler assembly processes may be enabled.

Methods: We use a commercially available PLA (polylactic acid) filament containing iron powder and a popular mid-level consumer-style 3D printer. The ease of printing shims allows us to address most questions experimentally, using NMR-based field mapping.

Results and discussion: We have found that the filament has an appropriately strong magnetization density and polarizes reproducibly in magnetic fields well below its saturation field. The commercially available 3D printer has sufficient resolution and precision. The printed filament material is both isotropic and linear, and the finite volume of the material, which leads to a build-up of thickness in the shim, can be accounted for via calibration.

The shim design for a particular magnet may be based on measured field maps for iron-pole magnets or on calculated fields for Halbach arrays. The design can be found using simple least squares minimization, linear programming, SVD-based techniques, or other methods.

The main limit for the method is in the software that slices the calculated shim design into layers for 3D printing. The printer operates from a text file containing g-code, and we find it useful to produce this g-code ourselves in order to achieve higher resolution in the rendering of the mathematical shim design. We have produced corrections in the form $\pm Z^{2N}$ for N= 1,2, and 3 for a 0.3T iron-pole magnet. The impact of these shims on measured field errors of the form Z^n is shown in Figure 1. These shims are constructed from annular-shaped elements. To correct other field errors, the annular elements were divided in arc segments with independent heights. For Halbach ring magnets, the shims consisted of 64 rectangular tiles of independent height arrayed on the surface of a cylinder. Shims for magnets of field 0.3, 0.5, and 1.4 T have been implemented.

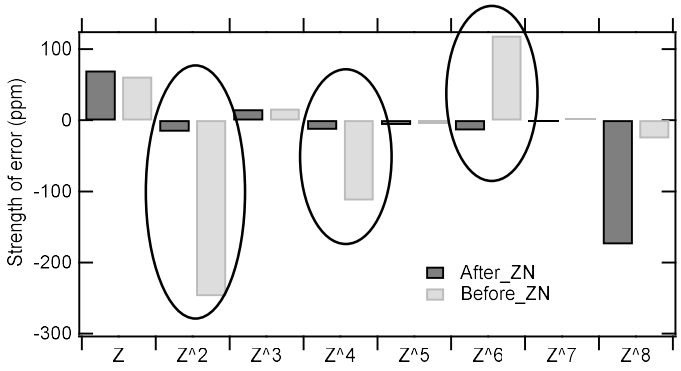

Conclusion: 3D printing of magnetic filament is an effective approach for shimming magnets that require strong correction fields.

References: [1] McDowell & Lown, App. Magn. Reson. (2023).

Figure 1. The mitigation of Z^{2N} errors (see ovals) in a 0.3 T iron-core dipole

B_0 Field Optimization of Permanent Magnet Assemblies with Characterized Field Variations in Individual Magnets Using Genetic Algorithms

K. Lavronenko[1,2], *Marcel Ochsendorf*[1,2], *Volkmar Schulz*[1,2]
[1]RWTH Aachen University, LfB Institute, Aachen, Germany,
[2]Fraunhofer Institute for Digital Medicine MEVIS

Introduction: Low-field MRI systems using permanent magnets offer accessible and cost-effective imaging solutions [1]. Yet, achieving uniform B_0 fields remains a major challenge. One of the major reasons for is the remanence variation in individual magnets. This study investigates whether characterizing individual remanence and optimizing magnet placement using genetic algorithms (GA) can improve field homogeneity prior to shimming.

Methods: We studied a ROMA configuration from the OSII project [2], comprising 2320 N52 NdFeB magnets (12×12×12 mm^3 inner, 12×12×50 mm^3 outer), generating 45–50 mT within a 20 cm spherical FOV.

1. **Magnet Characterization:** Remanence of 318 magnets from multiple batches was measured using an MMC5603 Memsic Inc. (±0.2 µT). The remaining magnets were sampled based on the observed distribution, Fig. 1.

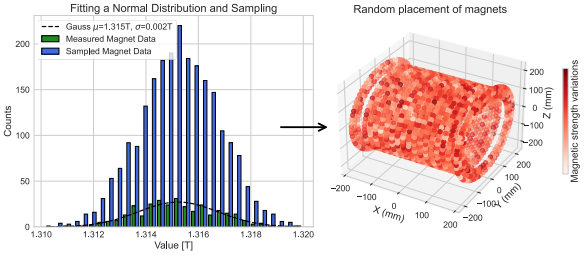

Fig. 1: Upsampling the measured magnet data using a fitted normal distribution. Right: Placement of magnets with sampled properties in the target system.

2. **Field Simulation:** A Biot-Savart dipole approximation [3,4,5] computed field maps on a 3D mesh grid for fast homogeneity assessment.
3. **Genetic Algorithm Optimization:** We evaluated 10,000 random permutations, then ran 10 GAs for both minimization and maximization of homogeneity (mutation rate: 10%, 500 mating parents, 200 generations) to analyze the possible homogeneity span when constructing the system.

Results and discussion: Fig. 2 shows the homogeneity variation across random arrangements (4431 ± 65 ppm). Maximization achieved up to 6566 ± 85 ppm, while minimization yielded 4189 ± 85 ppm — a 2377 ppm spread. This suggests that while random arrangements provide consistent average homogeneity, GA optimization can significantly enhance performance before physical assembly.

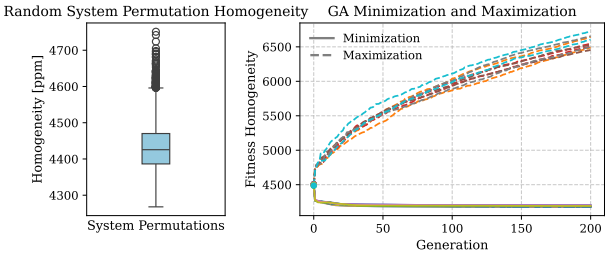

Fig. 2: Left: boxplot visualizing random homogeneity of random system arrangements. Right: development of the genetic algorithm optimizations.

Conclusion: Characterizing individual magnet remanence and applying GA-based configuration can substantially improve B_0 field uniformity in permanent magnet arrays. This approach offers a low-cost enhancement step before traditional shimming, particularly valuable in resource-constrained low-field MRI systems.

References: [1] H. Masaaki, DOI: : 10.1097/RLI.0000000000000810. [2] Winter, L. et al. DOI: 10.5281/zenodo.10079541. [3] S. Tewari et al., DOI: 10.1016/j.jmr.2021.106923. [4] T.O'Reily et al., DOI: doi.org/10.1002/mrm.28396. [5] A.J. Petrushka et al., DOI: 10.1109/TMAG.2012.2205014

Next generation optical widefield magnetic resonance microscopy

X. Chen[1], J.C. Draeger[1], U. Banerjee[1], R.D. Allert[1], K.D. Briegel[1], A. Blank[2], D.B. Bucher[1]
[1]Technical University of Munich (TUM), München, Germany, [2]Technion – Israel Institute of Technology, Haifa, Israel

Optical widefield nuclear magnetic resonance microscopy (OMRM) is a novel technique that fuses the spatial resolution of optical microscopy with the chemical specificity of nuclear magnetic resonance (NMR) spectroscopy. By leveraging nitrogen-vacancy (NV) centers in diamond, OMRM bypasses conventional magnetic resonance imaging (MRI) methods that rely on k-space encoding and magnetic field gradients, enabling direct real-space imaging of NMR signals through optically detected magnetic resonance (ODMR). In prior work, we demonstrated the capabilities of this widefield optical NMR microscopy approach by imaging NMR signals within a model microstructure, achieving a spatial resolution of approximately 10 µm over an area of ~235 × 150 µm². Each camera pixel captures a complete NMR spectrum, providing comprehensive information on signal amplitude, phase, local magnetic field strengths, and gradients [1].

Here, we present our current development for our next-generation OMRM platform, which has improved sensitivity, a larger field of view, and enhanced chemical resolution. The microscope has been integrated into a superconducting magnet with an increased magnetic field strength of > 0.4 T. It also integrates a 2.1 mm × 30 µm top-hat light-sheet illumination system and a new high-speed camera with an increased frame rate, enabling enhanced sensitivity and a 2 × 2 mm² field of view in microfluidic environments [2,3]. By combining the advantages of optical imaging with the chemical specificity of NMR [4,5,6], this technology opens up new possibilities for highly parallelized chemical analysis at the microscale. It lays the groundwork for a broad range of applications, including high-throughput NMR analysis and high-resolution magnetic resonance imaging of thin-film materials [1,7].

References: [1] Briegel, Nat. Commun. (2025). [2] Allert, Lab. Chip. (2022). [3] Bruckmaier, J. Magn. Reson. Open. (2021). [4] Bucher, Nat. Protoc. (2019). [5] Glenn, Nature. (2018). [6] Levine, Nanophotonics. (2019). [7] Bruckmaier, Sci. Adv. (2023).

µ-MRI on ion exchange resin interaction with nanoscale substances

L. Kontschak[1], O. Gruschke[2], L. Trapp[1], H.N. Baser[3], N. MacKinnon[3], P. Rychen[4], H. Nirschl[1], G. Guthausen[1,5]

[1]MVM-VM, KIT; [2]Bruker BioSpin GmbH & Co. KG, Ettlingen, Germany; [3]IMT, KIT; [4]Ovivo Switzerland AG, Witterswil, Switzerland; [5]EBI-WCWT, KIT, Karlsruhe, Germany

Introduction: Ion exchange resins are often used to remove nanoscale impurities from water. The interactions between resins and nanoparticles/molecular clusters determine the purification efficiency. Time resolved µ-MRI gives in depth insight into interactions and their kinetics.

Materials and methods: The interactions of nanoscale moieties (~ 2 - 80 nm) with anionic and cationic polymeric ion exchange resin beads (~ 600 µm) were studied by MRI at 400 MHz ^{1}H-Larmor frequency. RARE and FLASH pulse sequences were applied, using different rf coils depending on the length scale of the samples. Images with in-plane resolution down to 15 µm x 15 µm were measured with a µ-coil [1].

Results and discussion: Size and surface chemistry determine interactions between resins and nanoparticulate moieties. First, resin beds allowed the observation of interaction on the scale of ≈ 20 mm. Penetration kinetics were quantified at the next smaller length scale of resin stacks (Fig. 1) with a time resolution in the order of 4 min. The MR-images show a reduced signal intensity of the beads when a molecular contrast agent was absorbed (Fig. 1). Images were processed exploiting the circular geometry [2] to obtain the mean signal intensity averaged over the angle as a function of the radial coordinate of a single bead. The intensity profiles within a bead (Fig. 2) were modelled by a sigmoidal function to quantify kinetics. On the length scale of single beads, the localization of superparamagnetic nanoparticles on and in the beads was measured, exploiting the impact of the superparamagnetism of the nanoparticles on the static magnetic field. [3]

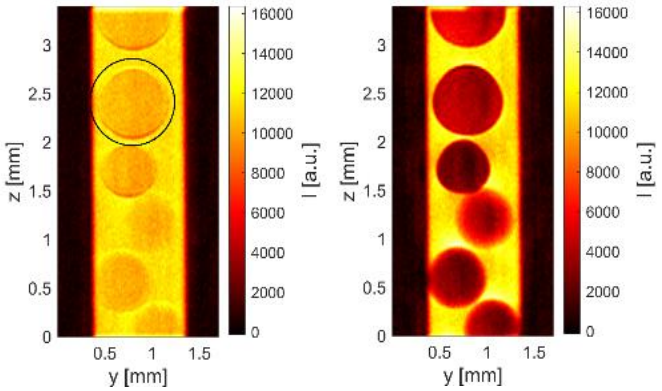

Fig. 1: Anionic resins beads in water (left) and in Magnevist solution after an exposure time of 1.5 h (right). The circled resin bead was analyzed for Fig. 2.

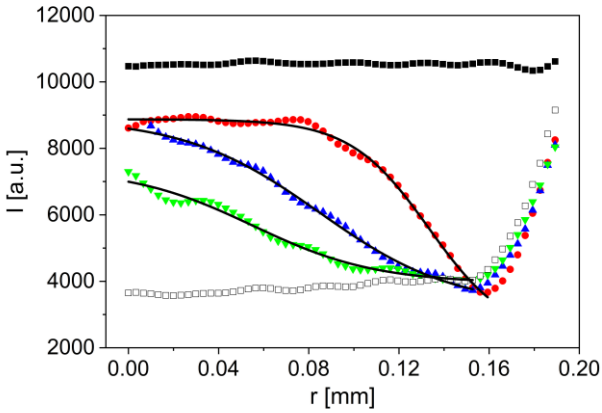

Fig. 2: Radial intensity profiles implicitly as function of the penetration time. The minimum indicates the transition between resin bead and surrounding solution.

References: [1] Bruker. Fruit fly meets microcoils – a magnetic resonance microscopy investigation of Drosophilae. Accessed May 07, 2025. https://www.bruker.com.
[2] N. Schork et al., Magn Reson Chem., 2019, 4-5.
[3] L. Kontschak et al., AIchE Journal, 2024.

Mixing polymer cocktails: Diffusion and relaxation distributions of mixed and polydisperse poly (ethylene oxide) melts

K. Lindt[a], C. Mattea[a], S. Stapf[a] , S. Mailhiot[b]

[a]Dept of Technical Physics II, TU Ilmenau, 98684 Ilmenau, Germany

[b]Bruker BioSpin GmbH & Co. KG, Rudolf-Plank Str. 23, 76275 Ettlingen, Germany

Introduction: Theoretical predictions and experimental evidence for polymer melt dynamics date back for at least four decades, with NMR being a strong contributor by a combination of several techniques: whereas pulsed and constant field gradient diffusometry determines mean-squared displacements (MSD) within a rather narrow time interval from about 1 ms to 1 s, relaxometry of attached protons and other nuclei covers a much wider range of times but gives more indirect information that needs to be translated into MSD on the basis of available models. Common to the vast majority of studies is the restriction to ideal, monodisperse linear molecules with a well-defined length, a situation that can be approximated with some technical polymers but is never perfectly met. Important questions remain largely unanswered: how does an inherent distribution of molecular weights affect the measured quantities, and are diffusion and relaxation affected in different ways?

Methods: PEO melt samples with the narrowest available dispersity (typically 1.1) in bulk and in mixtures of 10% ^{1}H-containing in 90% ^{2}H-containing PEO were studied by PFG diffusometry, relaxometry and comparative echo analysis (e.g. Hahn, solid) and were compared to artificially broadened molecular weight distributions obtained from mixing defined samples with defined molecular weights. Measurements were predominantly carried out on the ^{1}H resonance, i.e. the minority component. Diffusion experiments were carried out with a Bruker Diffusion Observe Broadband Probe providing a maximum pulse gradient strength of 16.9 T/m at a resonance frequency of 500 MHz and at variable temperatures above the bulk melting point of PEO, between 343 and 373 K. Echo and relaxation dispersion data were obtained on a Bruker Avance III 7T spectrometer and a Stelar Spinmaster Relaxometer in the field range 0.2 mT to 0.5 T.

Results and Discussion: the essential questions considered the relative change of diffusion and relaxation properties of a component A in a matrix B, or of a defined mixture, considering the different theoretical predictions for melts below and above the critical molecular weight which is estimated at 5 kDa for PEO. For diffusion, the conditions of the majority matrix (90 vol%) dominate the minority component, i.e. short chains in a matrix of long chains are severely restricted in their mobility whereas long chains in a matrix of short chains show a significantly increased mobility compared to the homogeneous bulk. Relaxation qualitatively follows this trend and supports the concept of Rouse dynamics and chain reptation, respectively, as deuteration is sufficient to suppress intermolecular relaxation contributions. For these mixtures, both diffusion and relaxation are found to mostly behave exponentially. In protonated melts of narrow and broad weight distribution, however, multiexponential behavior is clearly identified in diffusion but absent in T_1 relaxation, making PFG diffusometry a possible tool for the quantification of polymer polydispersity.

Conclusion: Diffusion behavior of polymer melts with polydispersity as low as 1.1 can be identified as non-exponential, with average diffusivity values following the expected Mw dependence. Spin diffusion and cross-relaxation are much more efficient in averaging out relaxation properties so that it can be concluded that high-gradient PFG diffusometry can establish access to a quantitative assessment of polymer quality not only in solution, but also in the melt state.

Dissolved or immobile polymer in disperse systems – a simple T2 approach

J. Okeke[a], I. Koppenhagen[b] , D. Obst[c], M. Mützel[d], T. Drießle[d], M. Britton[a], N. Nestle[b]
[a]School of Chemistry, University of Birmingham, Edgbaston, UK, City, [b]BASF SE, Ludwigshafen, Germany, [c]BASF Personal Care and Nutrition GmbH, Monheim, Germany, [d]Pure Devices GmbH, Rimpar, Germany

Introduction: In disperse polymer-containing formulations, microscopic and macroscopic dynamics of the material can be grossly different from each other, especially if solid mineral components are also present. Due to a combination of turbidity and possibly high viscosity, classical approaches (such as OECD guidelines 105 or 120) for assessing whether a substance is dissolved or not, are often hard to apply in case of such formulations. Additionally, separating the polymer from the formulation is often challenging to do and will of course change its dissolution state anyway. Thus, it is advantageous to utilize a non-invasive technique, such as TD-NMR, which is unaffected by sample turbidity and high viscosity, to probe the dynamics of these systems. Additionally, the presence of mineral components would only have a limited influence, except in the case of paramagnetic or ferromagnetic substances. By means of a combination of a solid echo and a CPMG train, a T2-decay can be recorded over about 6 orders of magnitude in time to provide an assessment of the solution state of various polymer formulations

Methods and discussion: While the measurement of this T2-decay is quite straightforward, classical evaluation strategies such as multicomponent fitting or (1D) inverse Laplace transforms often require user interference and/or come with numerical instabilities, such that a fast automatic assessment of the dissolution state of the polymer is often not easily achievable. Results can also be subject to evaluator biases. To overcome these problems , we propose a simple integral method based on the ratio between the average signal amplitude over the first 15 µs of signal and the first 100 µs of signal in the solid echo, calculating a polymer restricted mobility index according to Eq. 1. This index will be close to zero for a dissolved polymer and increases for samples containing undissolved polymer populations. Samples with different polymer concentrations can then be compared, quantitatively, by normalizing this index by the polymer concentration.

$$x = \frac{\langle s(t)\rangle_{15}}{\langle s(t)\rangle_{100}} - 1 \qquad \text{Eq. 1}$$

The CPMG part of the data is not required in this simple analysis. However, it often provides relevant supplementary insights, such as, for example, the surface relaxivity of non-dissolved disperse polymer, which is lost upon dissolution. The viability of the simple integration approach was checked over a range of data from different instruments by different vendors, indicating consistent results.

In TD-NMR experiments at typical field strengths in the range of 20 MHz, signal/noise ratio and dynamic range can be challenging in samples with low polymer concentrations. In such samples, dynamic range limitations can be overcome by partially or fully deuterating the water phase.

Characterization of time-varying magnetic fields via spin-lock based magnetic resonance fingerprinting

M. Gram[1,2], P. Albertova[1,2], P. M. Jakob[2], P. Nordbeck[1]

[1]Department of Internal Medicine I, University Hospital Würzburg, Würzburg, Germany

[2]Experimental Physics 5, University of Würzburg, Würzburg, Germany

Introduction: Spin-locking (SL) can be used to effectively reduce the Larmor frequency in the rotating frame [1]. Under SL conditions, relaxation processes such as $T_{1\rho}$ and $T_{2\rho}$ show sensitivity to low-frequency interactions and can be exploited to analyze macromolecular remodeling [2]. Besides relaxation, spin dynamics slow down, allowing magnetic oscillations in the Hz to kHz range to be absorbed [1]. This phenomenon, known as Rotary Excitation (REX), can be utilized for the direct detection of biomagnetic fields [3]. In this study, we demonstrate that REX, in combination with Magnetic Resonance Fingerprinting (MRF), can be used more broadly to characterize temporally varying magnetic fields.

Methods: The REX effect was modeled using numerical simulations of the Bloch equations via a fourth-order Runge-Kutta integration. Simulations were conducted for 10^5 combinations of relaxation times, static field deviations, and different magnetic waveforms. Gaussian- and Sinc-shaped fields with a maximum magnitude of 100 nT and varying time-bandwidth products (TBW) were simulated, and their REX responses were analyzed for different SL field strengths. The resulting dictionary was matched against experimental data acquired on a clinical 3T MRI system (Siemens Magnetom Skyra). The goal was to identify the controlled stimulus fields by means of a pattern matching algorithm.

Results and discussion: A strong agreement was observed between the simulated and measured REX signals. Gaussian and Sinc fields could be reliably distinguished in 97% of voxels within the field of view, and TBW values were identified with at least ±1 accuracy in 94% of cases. The mean inner product used for the pattern-matching algorithm was 0.997. For accurate matching, it was essential to include static field deviations (ΔB_0 and ΔB_1) in the model. ΔB_0 introduced additional oscillations in the REX response, while ΔB_1 altered the effective SL amplitude, leading to spectral shifts in the acquired signals.

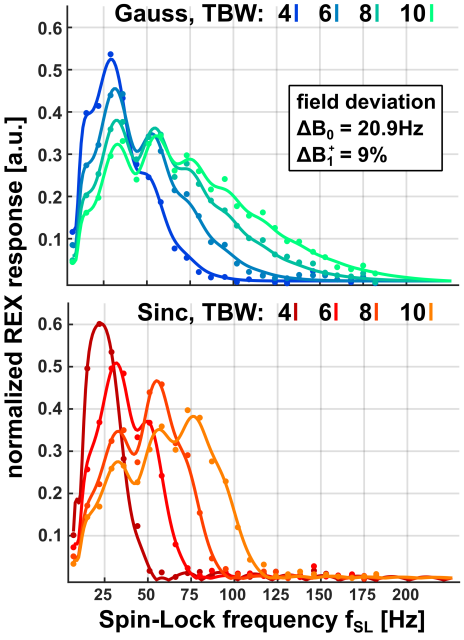

Measured (dots) and matched (lines) REX responses for Gauss- and Sinc-shaped field variations.

Conclusion: This work demonstrates that spin-locking combined with MRF concepts enables spectral analysis and temporal characterization of magnetic fields using a standard clinical MRI system. This approach also indirectly enhances the temporal resolution of SL-based field detection sequences. Future studies will explore whether this method can be applied to assess and calibrate implanted devices such as deep brain stimulators. For imaging biomagnetic fields - such as those associated with epilepsy [4] or cardiac conduction [5] - the presented approach could offer new perspectives for improved and accelerated detection.

References: **[1]** Redfield. Phys Rev. 98;1787 (1955) **[2]** Bustin et al. JCMR. 25;34 (2023) **[3]** Gram et al. Sci Rep. 13;12(1) (2022) **[4]** Kiefer et al. Radiology. 280(1):237-43 (2016). **[5]** Albertova et al. Magn Reson Med. 92(5):1965-1979 (2024)

Chemical Exchange Transfer Imaging: Efficient RACETE acquisition with Balanced Imaging Gradient Readout

F. Fidler[1,2], *S. Mayer*[1,3], *J. Balling*[1], *D. Miksch*[1], *PM. Jakob*[1], *FT. Gutjahr*[1]
[1]University of Wuerzburg, Germany, [2]Fraunhofer-Institute for Integrated Circuits, Wuerzburg, Germany, [3]Leibniz-Institute of Plant Genetics and Crop Plant Research, Gatersleben, Germany

Introduction: We implemented RACETE[1] (Refocused acquisition of chemically exchanged transferred excitation) with a modified balanced SSFP-style readout[2], enabling efficient imaging of chemical exchange (CE). Unlike standard Chemical Exchange Saturation Transfer (CEST), RACETE generates a true positive contrast by refocusing prepared and subsequently exchanged magnetization. Compared to earlier implementations[3,4], the modified approach enables full image acquisition from a single preparation, substantially accelerating data acquisition.

Methods: RACETE employs a readout module adapted from the vendor's bSSFP sequence (Fig. 1 top). Preparation consists of 90° pulse pairs around an encoding gradient (G_S), repeated N_{ETM} times. The readout module following exchange pool preparation reuses G_S once to decode the stimulated echo signal after each α-pulse, and again after the data acquisition. The imaging block is repeated to fill k-space.
Measurements were performed on a 750 MHz spectrometer (Bruker, Germany) using salicylic acid in water. Parameters: N_{ETM} = 150, ω_1 = 9.1 ppm, matrix 128×64, FOV 20×20 mm², TE/TR = 3.5/7.0 ms, α = 50°. A FLASH-like method with similar settings was used for comparison, acquiring 128 FIDs post-preparation.

Results: Fig. 1 summarizes the results obtained with the newly developed RACETE sequence. It includes a comparison of the signal amplitudes from the first 128 readouts after a single preparation for both the RACETE method with balanced gradients and the FLASH-like spoiled approach. The figure also shows a stack of ten consecutively acquired RACETE images after a single preparation, enabling $T_{1,water}$ evaluation. Total acquisition time for this image series was 8 s, including 2 s for the preparation module.

Discussion: The modified RACETE maintains the true positive CE-contrast, while increasing the efficiency. Imaging gradients are fully rebalanced in each TR, the encoding/decoding gradients G_S are not. This ensures that the non-exchanged, non-encoded water signal is not refocused during any of the acquisitions, preventing contamination of the RACETE contrast. Simultaneously, the additional refocusing enhances signal by refocusing each STE, increasing SNR and permitting larger flip angles than in a purely FLASH-like approach.
These improvements support in vivo applicability: RACETE images can be acquired rapidly, and inherent $T_{1,water}$-evaluation can be used to eliminate unwanted $T_{1,water}$-influences from chemical exchange contrast.

References:
[1] Gutjahr, ZMedPhys. (2019).
[2] Fidler, Proc. ISMRM (2007).
[3] Mayer, Proc. ESMRMB (2019).
[4] Zhao, MRI (2022).

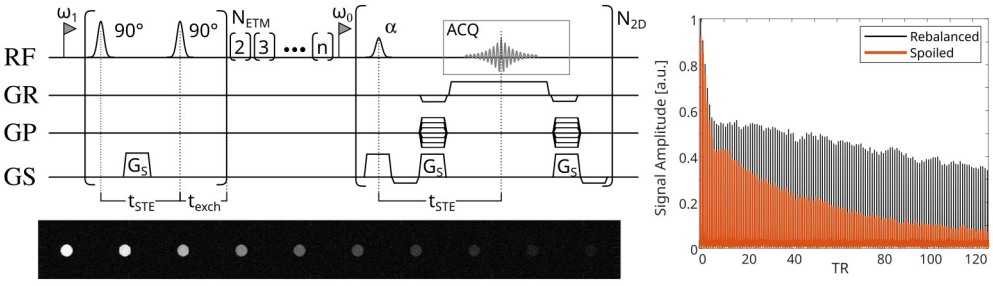

Figure 1: Left: Simplified sequence diagram, Right: Comparison of 128 spoiled and balanced readouts. Bottom left: Images acquired after single preparation.

Understanding liquid transport in innovative 3D formed cellulose-based packaging using MRI

F. Guerroudj and D. Bernin
Chalmers University of Technology, Gothenburg, Sweden,

Introduction: Driven by the global shift toward circularity and sustainable resource management, the packaging industry (for e.g. food, cosmetics, ...etc) is being redefined through the development of innovative 3D fiber-based packaging made from waste and recycled materials. As single-use plastics continue to pose a major environmental threat, there is an increasing demand for renewable, recyclable alternatives that offer comparable performance. Among these innovations is the dry-formed cellulose packaging technology [1] capable of replacing plastic at scale. In this process, fluff cellulose pulp is fed into a mill where it is separated into individual fibers and combined with functional additives. The fibers are then airlaid into dry pads, which are shaped into thin, rigid products through a heat and pressure-based deep-drawing step, followed by trimming and finishing. This method significantly reduces water usage and yields high-rigidity packaging that outperforms traditional wet-moulded fiber products. To further optimize this process and improve the product performance, in-depth material characterization is essential. Our work focuses on using MRI to investigate liquid transport within these fiber-based materials.

Methodology: A MRI method has been developed and applied to monitor water ingress in flat packaging surfaces [2]. For complex packaging geometries, a specific MRI instrumentation is required. As part of our research, we are designing a miniature radiofrequency (RF) coil adapted to the shape of the packaging and placed near the region of interest to enable localized measurements of liquid transport. By minimizing the coil's dimensions, we increase the filling factor, which enhances the signal-to-noise ratio (SNR) and significantly improves the sensitivity of the MRI analysis.

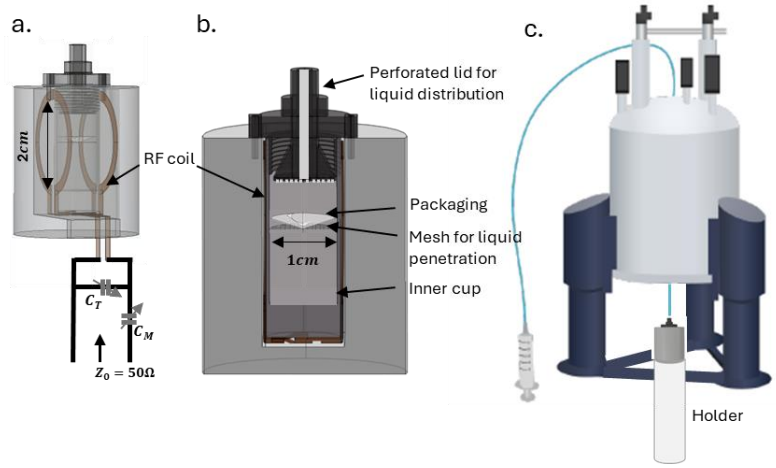

Figure: MRI setup. (a) The RF coil and its electronic circuit. (b) A cross section of the setup. (c) Implementation of the setup in the MRI magnet.

Conclusion: We believe that this advanced analytical approach will provide deeper insights into liquid transport within complex 3D materials, advancing dry forming technology to produce higher-performance, innovative and sustainable packaging. This will establish a solid foundation for scalable, circular solutions that support the transition to a more sustainable, biobased economy.

References: [1].Dry Forming Process. https://www.yangi.se/the-process . [2]. M. ÅKESSON. Master's thesis in Materials Engineering. Chalmers Univ of Tech

Measurements of intra-diffusion coefficients for gaseous binary mixtures

S. Kobeissi[1,2], N.N.A. Ling[1,2], E.F. May[1,2], M.L. Johns[1,2]
[1]Department of Chemical Engineering, The University of Western Australia, Crawley, WA, Australia
[2]Future Energy Exports CRC, Crawley, WA, Australia

Introduction: Diffusion in gaseous mixtures is critical to many industrial and geological processes, yet experimental data are sparse, particularly for intra-diffusion coefficients at elevated pressures. Existing relationships between intra- and mutual-diffusion, well established in liquids, are less validated for gases. We address this gap by measuring intra-diffusion coefficients (D_i) in three binary gas mixtures across a range of compositions and industrially relevant pressures and temperatures.

Methods: Measurements were conducted using a custom-designed, NMR-compatible Sapphire High Pressure cell integrated into a 43 MHz benchtop NMR spectrometer (Figure 1). Intra-diffusion coefficients (D_i) were measured using the Pulsed Field Gradient Spin Echo (PGSE) technique across methane–nitrogen, methane–helium, and methane–hydrogen binary mixtures at temperatures from 28 to 40 °C and pressures up to 100 bar. The composition of each mixture was verified by NMR spectroscopy, and measurements were corrected for restricted diffusion effects using validated numerical simulations.

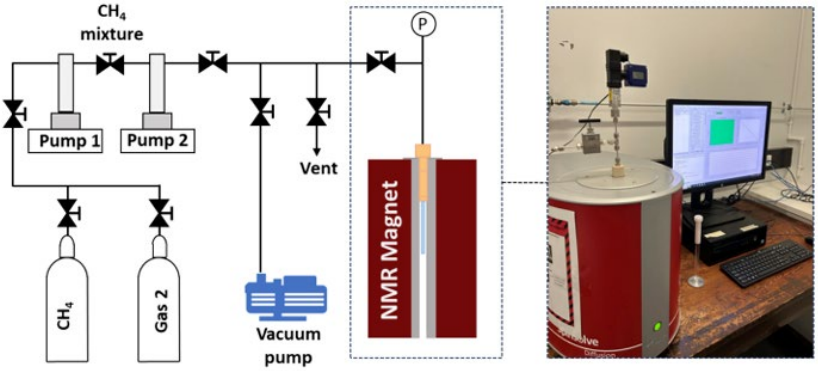

Figure 1: Experimental Setup

Results and Discussion: Intra-diffusion coefficients were obtained as a function of composition for all mixtures studied. Values of D_i were extrapolated to infinite dilution and compared to mutual diffusion coefficients (D_{12}) from both literature and Chapman-Enskog kinetic theory [1,2]. For methane–helium mixtures, agreement was within experimental uncertainty. For methane–nitrogen, D_i (x_i=0) exceeded D_{12} predictions by 8–10%. In the methane–hydrogen system, both CH_4 and H_2 intra-diffusion coefficients were measured, revealing good agreement for H_2 but a moderate deviation for CH_4.

Conclusion: This study provides new experimental data on intra-diffusion in gaseous binary mixtures using an NMR-compatible high-pressure setup [3]. Results show generally good agreement with kinetic theory, but also reveal differences that suggest the need for refined models, particularly in mixtures with hydrogen. These data support the development of predictive models for high pressure and temperature gas diffusion as a function of composition.

References: [1] Berry Jr., AIChE J. (1960). [2] Chapman, S., The Mathematical Theory of Non-Uniform Gases (1990). [3] Kobeissi, S., Chem. Eng. Sci. (2025).

Cooking Eggs in NMR
Measuring the Denaturation of Egg Protein using T1&T2 Relaxometry

S. Wintzheimer[a], T. Driessle[a], A. Krönlein[a], M. Mützel[a], P. Vogel[b,c], M. Distler[a]

[a] Pure Devices GmbH, Rimpar, Germany, [b] Department of Experimental Physics 5 (Biophysics), University of Würzburg, Germany, [c] phase VISION GmbH, Rimpar, Germany

Introduction: Protein denaturation is a fundamental process in food science and biochemistry, involving structural changes in protein molecules under thermal stress [1]. Chicken eggs, which contain a variety of proteins with distinct thermal stabilities, serve as an excellent model system for investigating heat-induced denaturation. Traditional analytical methods often lack the temporal resolution or sensitivity to capture real-time molecular transitions. Time-Domain Nuclear Magnetic Resonance (TD-NMR) offers a non-invasive and sensitive approach to monitoring these structural changes via T1 and T2 relaxation times, which reflect molecular mobility and interactions in the protein matrix [2]. In this study, TD-NMR with controlled temperature variation was used to monitor the denaturation behavior of egg proteins during the cooking process.

Methods: Fresh chicken eggs were separated into egg white and egg yolk, and samples were prepared in 15 mm NMR tubes. Additionally, a mixed sample of egg white and yolk was created, and vegetable oil was used as a reference. Samples were placed in a variable-temperature (VT) NMR probe and initially equilibrated at 49 °C. The temperature was then increased in 1 °C steps up to 90 °C, with measurements taken at each step after 3 minutes of thermal equilibration. Subsequently, the temperature was decreased in the same manner. For each temperature point, T1 inversion recovery and T2 Carr-Purcell-Meiboom-Gill (CPMG) measurements were performed. The resulting relaxation data were fitted using both single- and double-exponential models. For analysis, T1 and T2 values and fitted signal amplitudes at time t = 0 were used.

Results: Figure 1 presents the estimated fraction of non-denatured proteins as a function of temperature, with the total denatured content shown in red and the T2 trend of egg white shown in purple. The observed T2 changes correlate with the known denaturation temperatures of specific proteins, particularly Ovalbumin and Ovomucoid.

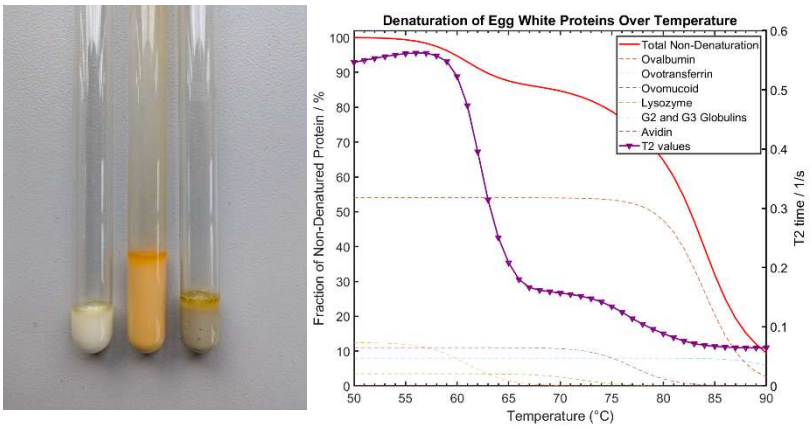

Fig. 1: left: Egg white, yoke and mixed egg in glass tubes after denaturation experiment. Right: Fraction of the non-denaturated proteins compared to T2 values.

Conclusion: Both the relaxation times and the extrapolated signal amplitudes at t = 0 provide valuable insights into the thermal denaturation behavior of egg proteins. These changes can be linked to the known thermal stability of specific proteins, demonstrating the potential of TD-NMR relaxometry for real-time, non-invasive monitoring of protein structure during cooking processes.

References: [1] Y. Mine, Trends in Food Science&Technology, 6(7):225-32, 1995. [2] J.van Duynhoven et al., Ann Rep on NMR Spectroscopy, 69:145-97, 2010.

Sweet NMR: T2 relaxometry of different chocolate varieties

S. Wintzheimer[a], T. Driessle[a], A. Krönlein[a], M. Mützel[a], P. Vogel[b,c], M. Distler[a]

[a] Pure Devices GmbH, Rimpar, Germany, [b] Department of Experimental Physics 5 (Biophysics), University of Würzburg, Germany, [c] phase VISION GmbH, Rimpar, Germany

Introduction: Time-Domain Nuclear Magnetic Resonance (TD-NMR) has proven to be a valuable tool for non-invasive analysis of complex food systems, offering insights into molecular mobility and phase behavior through relaxation time measurements. Chocolate, as a multi-component material, exhibits temperature-dependent structural changes, particularly due to the phase transitions of cocoa butter—a key fat component with well-defined melting characteristics. In this study, we applied TD-NMR with variable temperature control to investigate the thermal behavior of different types of chocolate. By monitoring T2 relaxation times across a temperature range, we aimed to characterize structural transitions and their reversibility, providing a deeper understanding of how composition and processing influence the physical properties of chocolate.

Methods: The study examined the following chocolate varieties:

- Cheap dark chocolate (no name)
- Milk chocolate (Schogetten)
- Aerated chocolate (Milka Luflee, Mondelez)
- As reference sample of vegetable oil was used.

The chocolate was cut into shavings and pressed into a 15 mm glass tube to ensure good thermal contact to the tube.

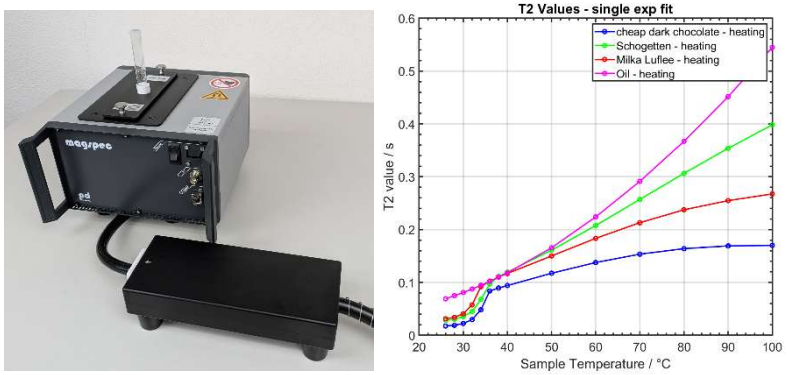

Fig. 1: left: Portable MagSpec MRI system with 0.5 T B0-field strength and heating device. **Right**: T2 values of different chocolate varieties.

The sample was put into the variable temperature (VT) probe which was set to room temperature (26°C). The temperature was increased in 2°C steps up to 40°C. In this range most of the relaxation time changes were expected. Further temperature increase was performed in 10°C increments up until a maximum temperature of 100°C. After reaching the maximum of 100°C, the temperature was decreases in reverse. After 5 minutes tempering at the target temperature (waiting time), a T2 CMPG measurement was performed. The acquired data was fitted to a single exponential model. For further evaluation, the fitted T2 values as well as the fitted signal amplitudes at time t = 0 were used.

Results: Figure 1: right shows the T2 values for the increasing temperature profile. One can see the melting of the cocoa butter occurs between 28°C and 36°C, which agrees with literature values [2]. The temperature dependency of the T2 values for the different varieties of chocolate is also clearly different.

Conclusion: The relaxation times show interesting effects at different temperatures. The effects can be correlated to the phase transition of the cocoa butter. Boltzmann calibrated measurements can for example be used for SFC (solid fat content) determination of chocolates.

References: [1] J.van Duynhoven et al., Ann Rep on NMR Spectroscopy, 69:145-97, 2010. [2] Ullmann's Food and Feed. Vol. 2, Wiley, 655 f 706, 2017.

Structural investigations of nuts by NMR

L. Trapp[1], N. Weis[1], T. Eirich[1], H. Schacht[2], H. Nirschl[1], G. Guthausen[1,3]

[1]Institute of Mechanical Process Engineering and Mechanics, Karlsruhe Institute of Technology, Karlsruhe, Germany, [2]Food Process Development, Fraunhofer Institute for Process Engineering and Packaging IVV, Freising, Germany, [3]Engler-Bunte-Institut, Water Chemistry and Technology, Karlsruhe Institute of Technology, Karlsruhe, Germany

Nuts contain a large amount of oil (≈ 60 % ww^{-1}) mainly stored in subcellular structures (oleosomes) [1-3]. They play a key role in the shelf life and quality of nuts, especially in chocolate products. Nuts in chocolate products usually undergo specific processes inducing thermal and mechanical stress. The stability and integrity of oleosomes is hereby crucial, as potential instability leads to undesirable effects such as fat bloom or oil syneresis [4]. Changes in these microscopic structures due to thermal and mechanical stress must be considered. In-situ MRI measurements were carried out and complemented by PFG-NMR (PFG-STE) for diffusion measurements [5]. MRI detects macrostructural changes on length scales ranging from 50 µm to millimeters above the length scale of cells. Special equipment allows for the analysis of nuts during roasting or blanching under controlled temperature conditions in the magnet. The spatially resolved MRI measurements determine the oil distribution in the coarse structure of the nut. Diffusion measurements provide additional information on the microstructure (100 nm - 10 µm). Thus, insight into the type of oil mobility was obtained. A model was developed for the size determination of oleosomes based on droplet size determination in emulsions [6-8], which needed to be extended by a term describing quasi-free diffusion oil. The investigations show the potential of the quasi-non-destructive measurement of the microstructure in nuts using PFG-STE. The influence of thermal process parameters such as roasting temperature and duration were deduced on the micro- and macrostructures of the nut.

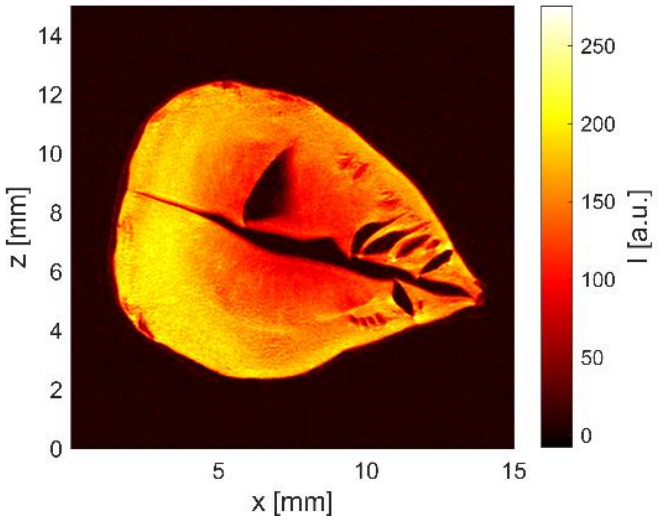

Fig. 1: MR Image of a roasted hazelnut.

References: [1] B. Mert und T. A. Vilgis, Hydrocolloid coated oleosomes for development of oleogels, Food Hydrocolloids, 119, 106832, 2021. [2] A. C. Dave, A. Ye und H. Singh, Structural and interfacial characteristics of oil bodies in coconuts (Cocos nucifera L.), Food Chem., 276, 129, 2019. [3] A. Barre, M. Simplicien, G. Cassan, H. Benoist und P. Rougé, Oil bodies (oleosomes): Occurrence, structure, allergenicity, Revue francaise d'allergologie, 58, 574, 2018. [4] Z. Shi, K. Li und Z. Meng, Recent trends in oleosomes: Extraction methods, structural characterization, and novel applications, Trends in Food Science & Technology, 104621, 2024. [5] L. Trapp, H. Schacht, H. Nirschl und G. Guthausen, Oleosomes in Almonds and Hazelnuts: Structural Investigations by NMR, Frontiers in Physics, 13, 1494052, 2025. [6] J. S. Murday und R. M. Cotts, Self-Diffusion Coeffcient of Liquid Lithium, J. Chem. Phys., 48, 4938, 1968. [7] C. H. Neuman, Spin echo of spins diffusing in a bounded medium, The Journal of Chemical Physics, 60, 4508, 1974. [8] K. J. Packer und C. Rees, Pulsed NMR studies of restricted diffusion. 1. Droplet size distributions in emulsions, J. Colloid Interface Sci., 40, 206, 1972.

Spatially and Time-Resolved MRI Studies on the Penetration of Inkjet Inks in Printing Substrates

E. Schmid[1], *H. Nirschl*[1], *G. Guthausen*[1,2]

[1]Karlsruhe Institute of Technology, Institute of Mechanical Process Engineering and Mechanics, 76131 Karlsruhe, Germany, [2]Karlsruhe Institute of Technology, Engler-Bunte-Institut, Chair of Water Chemistry and Water Technology, 76131 Karlsruhe, Germany

Thanks to technical developments, inkjet printing is a good alternative to conventional printing technologies for industrial applications (for example offset print). Impact of an ink drop on the paper, its distribution on the surface and its absorption and penetration are crucial for production efficiency, product quality and energy consumption. Due to its non-invasive and non-destructive operation, Magnetic Resonance Imaging (MRI) was applied to monitor the progress of ink penetration via spatially and time-resolved ^{1}H measurements [1, 2].

1D-MRI measurements were carried out at an ^{1}H Larmor frequency of 200 MHz on an in-situ printing experiment with a time resolution in the order of seconds: A paper disk was placed on a 3D-printed carrier in a 5 mm NMR tube and a defined ink volume was applied to the paper via a hose (Fig. 1). Thus, the penetration of the ink along *z* was measured time-resolved to quantify the absorption behavior (Fig. 2).

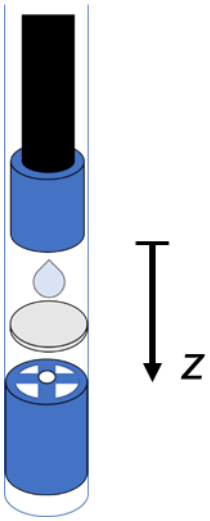

Fig. 1: Experimental setup in a 5 mm NMR tube with paper disk, carrier (blue) and an ink drop.

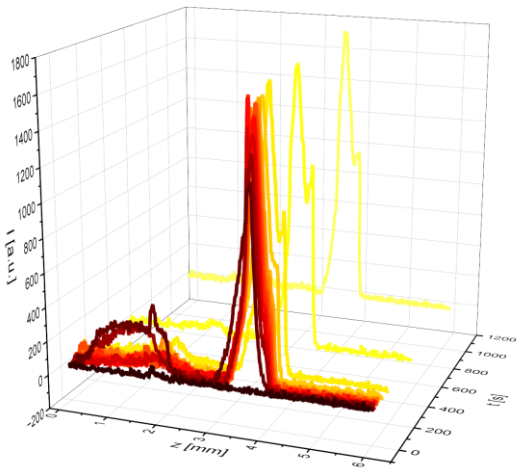

Fig. 2: Signal intensity profiles along *z* as a function of the experiment time. *t* = 0 s corresponds to the time at which the drop is added to the paper surface.

In order to investigate the effects of different inks and substrates on ink penetration, measurements were carried out on various material combinations. In addition, data processing was investigated in order to maximize the knowledge gained.

References: [1] S. Schuhmann und G. Guthausen, *NMR-Messmethoden: Produkt- und Prozesscharakterisierung*, Chem. unserer Zeit, 55, 236, **2021**.

[2] R. J. K. Nicasy, H. P. Huinink, S. J. F. Erich, O. C. G. Adan und N. Tomozeiu, *Ultra Fast Imaging NMR method for measuring fast transport processes in thin porous media*, Magnetic Resonance Imaging, 103, 61, **2023**.

Anaerobic digestate dewatering performance monitored using low-field ^{1}H NMR relaxometry

E.G. Bertizzolo[1], N. Ling[1], F. Tessele[2], M. L. Johns[1], E. O. Fridjonsson[1]

[1]School of Engineering, Department of Chemical Engineering, The University of Western Australia, Crawley, Australia, [2]Tessele Consultants, Attadale, Australia

Abstract

A growing challenge of industrial waste management is the large industrial-scale conversion of organic waste into valuable resources. For the transformation of anaerobic digestate (AD) into bio-based fertilizer [1] the de-watering step, via flocculation and mechanical dewatering, necessitates precise monitoring. Here we present low-field NMR relaxometry (T_2) results (see Fig 1) used to non-invasively track the change in digestate structure in response to varying flocculant dosing [2]. A series of NMR experiments were performed during flocculation and after mechanical de-watering for a dosing range of 0 to 5.25 wt%. Results show that monitoring AD samples during the flocculant dosing phase performs well at predicting solid's cake structure, and therefore de-watering performance, after the mechanical de-watering process. These findings encourage further exploration of low-field NMR to monitor similar solid-liquid separations of industrial digestate, and to allow for further assessment of low field NMR relaxometry as a monitoring tool for optimal flocculant dosage prior to mechanical de-watering.

Sample	Dosing (% wt)
1	0.00
2	0.75
3	1.50
4	2.25
5	3.00
6	3.75
7	4.50
8	5.25

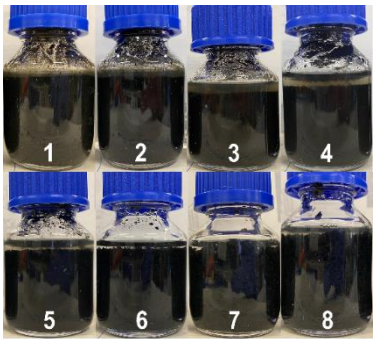

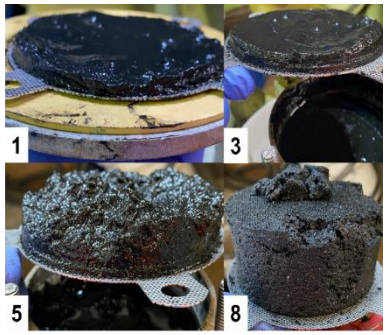

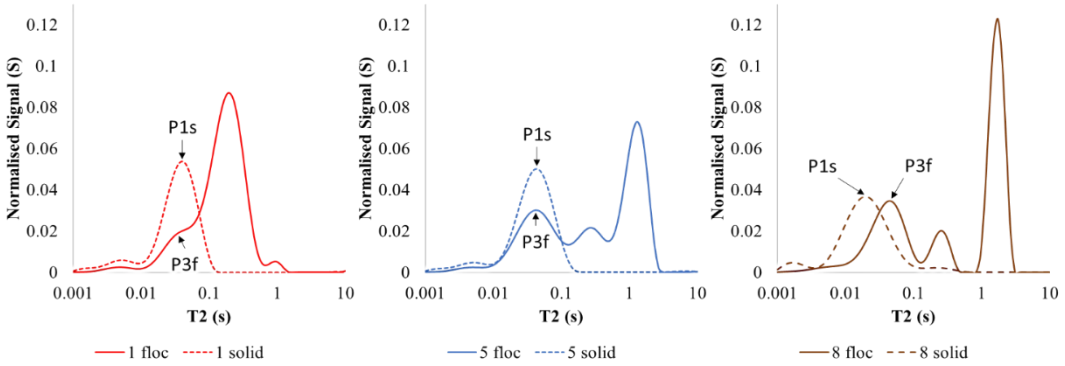

Fig. 1. Shows (a) flocculant dosing used, (b) photo collage of flocculated samples, (c) resulting solid's cake highlighted (Sample 1, 3, 5 and 8) after mechanical de-watering. (d) T_2 relaxation distributions for sample 1, 5 and 8 for flocculated (f, floc) and mechanically de-watered (s, solid) samples.

References:

[1] Ramirez *et al.* (2021), Animal Production Science, **61**, 541-550. [2] Bertizzolo *et al.* (2023), Water Research, **245**, 120660.

NMR Characterisation of Water-in-Crude Oil Emulsions: Effects of ICD-Induced Shear and Naphthenic Acids

N. N. A. Ling, M. Jackson, E. R. Shilliday, B. Hoskin, E. O. Fridjonsson, B. F. Graham, M. L. Johns
Department of Chemical Engineering, The University of Western Australia, Crawley, WA, Australia

Introduction: Water-in-crude oil emulsions present persistent challenges in oil production, increasing viscosity and complicating phase separation. These emulsions may form due to mechanical shear encountered in wellbore components such as Inflow Control Devices (ICDs) (Figure 1) and may be stabilized or destabilized chemically through surface-active compounds such as naphthenic acids (NAs).

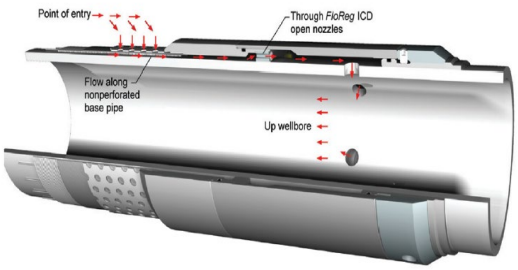

Figure 1: Nozzle type ICD

Methods: We employed Pulsed Field Gradient Nuclear Magnetic Resonance (PFG-NMR) and ^{1}H spectroscopy to quantify droplet size distributions (DSDs) [1], water content, and phase behaviour in opaque crude oil emulsions. An ICD-mimicking homogenizer was developed to simulate short-residence, high-shear mixing [2]. For chemical destabilization studies, commercial and indigenous NAs were added to crude oil samples emulsified with water, with samples analysed over time using PFG-NMR [3].

Results and Discussion: The ICD experiments revealed partial emulsification at high shear and low residence time, with median droplet size and emulsion viscosity increasing with water cut. In NA experiments, commercial NAs induced significant coalescence and phase separation (Figure 2) while indigenous NAs showed negligible effect. DSD broadening and a reduction in emulsified water signal were captured effectively by NMR, with bottle tests visually confirming separation trends.

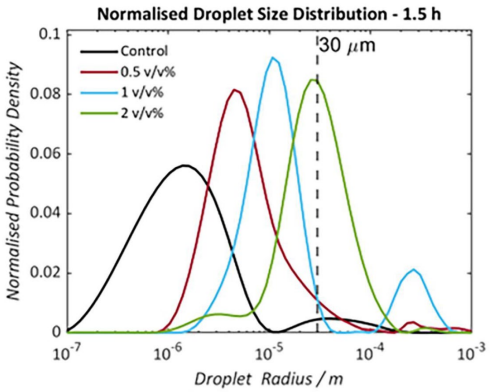

Figure 2: Saline (3.5wt %) crude oil A emulsion samples doped with 0 (black), 0.5 (red), 1 (blue), and 2 (green) v/v% Naphthenic Acid (Commercial).

Conclusion: This work highlights the utility of NMR for in situ, non-invasive crude oil emulsion characterisation and provides new insight into both mechanical and chemical drivers of emulsion stability relevant to petroleum transport and separation strategies.

References: [1] Hollingsworth, K.G., Magnetic Resonance Imaging (2003). [2] Jackson, M., Geoenergy Science and Engineering (2024). [3] Shilliday, E. R., Journal of Dispersion Science and Technology (2024).

A novel method for identifying pore fluids using nuclear magnetic resonance (NMR) logging in conglomerate reservoirs during oil-based mud (OBM) Drilling

Liang Xiao[a], *Jing Li*[b], *Tingting Hu*[b], *Xiuhong Xie*[a]
[a]China University of Geosciences,Beijing, China, [b]PetroChina Xinjiang Oilfield, Urumqi, China

Introduction: Identifying pore fluids in conglomerate reservoirs during oil-based mud (OBM) drilling presented significant challenges. Traditional methods, such as crossplotting porosity and resistivity or overlapping multiple curves, often fallen short due to extremely low hydrocarbon saturation. The differences in log responses between oil-bearing formations and fully water-saturated layers were minimal. However, nuclear magnetic resonance (NMR) logging could play a crucial role in formations drilled with water-based mud (WBM), and various methodologies had been proposed. Unfortunately, in formations where OBM was used for drilling, existing methods were ineffective because they did not account for the impact of OBM filtrate on NMR T_2 spectra. **Methods:** This study aimed to enhance the applicability of NMR logging for pore fluid identification in formations drilled with OBM. We conducted NMR experiments on 10 representative core samples retrieved from the Permian Urhe Formation in the Shawan Depression, located on the southern margin of the Junggar Basin. The samples were analyzed under three saturation conditions: fully brine-saturated, OBM displacing brine, and crude oil-saturated states. We sought to clarify the NMR response mechanism under the OBM displacing condition. For the fully brine-saturated rocks, the NMR T_2 distribution demonstrated a shallow unimodal pattern, with relaxation times ranging from 0.03 to 10 ms. When large pore spaces were occupied by OBM filtrate, the resulting T_2 spectrum showed a bimodal distribution, spanning from 0.03 to 60 ms, with the second peak correlating to the bulk relaxation time of the OBM filtrate. Following the injection of crude oil into the pore spaces, the NMR T_2 distribution evolved into a trimodal pattern. The left peak represented the surface relaxation of bound water, while the second and third peaks corresponded to the bulk relaxation characteristics of the OBM filtrate and crude oil, respectively, with the maximum relaxation time exceeding 100 ms. We established two T_2 cutoff values—3 ms and 100 ms—to classify the NMR T_2 spectra into three segments. Three parameters, S_1, S_2, and S_3, were derived from the NMR T_2 spectra, representing the ratios of pore spaces occupied by small, medium-sized, and large pores to the total pore space of the rock. A new parameter, termed the pore fluid index (ifluid), was introduced to indicate the presence of different pore fluids, as expressed in Equation 1. Criteria were developed to identify hydrocarbon-bearing formations, water-saturated zones, and dry layers (**Fig. 1**). **Results and discussion**: Field applications demonstrated that the proposed method was effective for our target conglomerate reservoirs during OBM drilling. **Conclusion:** The accuracy of pore fluid identification using NMR logging had significantly improved. Once this technique was widely adopted, it would facilitate better evaluation of conglomerate reservoirs in OBM drilling, thereby greatly expanding the applicability of NMR logging.

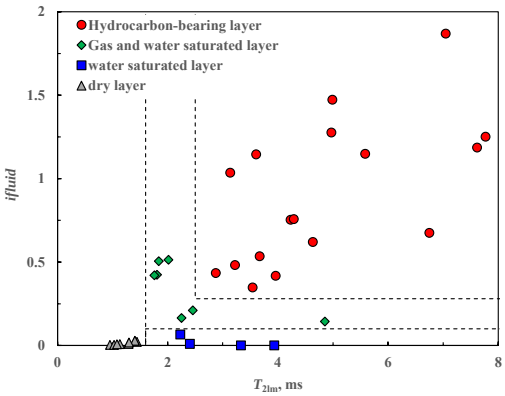

Fig. 1: Criteria for identifying pore fluids based on NMR logging in wells drilled with oil-based mud (OBM).

$$ifluid = \frac{S_2 \times S_3}{S_1^2} \times \varphi \qquad \text{Eq. 1}$$

Where, S_1, S_2, and S_3 represent the percentages of the total pore space of the rock occupied by small, medium-sized, and large pores, respectively. φ is the NMR total porosity in %.

References:
[1] Coates G R, Xiao L Z, Primmer M G. Houston: Gulf Publishing Company, USA (2000). [2] Gao F M, Xiao L.SPE Journal (2024).

Operando ^{1}H MRI reveals dead lithium in a symmetric Li|Li cell

R. Peklar[1,2], I. Serša[1,2], U. Mikac[1]

[1]Jozef Stefan Institute, Ljubljana, Slovenia, [2]Jozef Stefan International Postgraduate School, Ljubljana, Slovenia

Introduction: Reversibly plating and stripping lithium metal holds promise for high-energy-density batteries but is plagued by the formation of dendritic structures that compromise safety and cycle life. Indirect ^{1}H MRI, which images the proton-rich electrolyte displaced by metallic deposits, offers a non-invasive, three-dimensional view of dendrite morphology and evolution [1]. Here, we apply this technique to a symmetric Li|Li cell undergoing a plating–stripping cycle, enabling direct visualization of dendrite growth and dissolution in situ. By tracking volumetric changes and tip-velocity dynamics, operando ^{1}H MRI yields quantitative insights into lithium plating kinetics, which can be then used to evaluate electrolyte performance and the transient processes underlying dendrite formation.

Methods: A symmetric Li|Li cell (electrode gap 15 mm, 1 M $LiPF_6$ in EC:DMC) was imaged using a four-echo RARE sequence, while a galvanostat supplied ±1.5 mA; current was reversed after 20 h. Binary dendrite masks were generated by histogram-based thresholding and connected-component filtering, yielding time-resolved volumes, tip-velocity maps, and front heights.

Results and discussion: Dendrites nucleated as dense "moss" and transitioned to branched structures within ~10 h, consistent with a Sand's time prediction of 4.7 h at the applied current. Front height on the initially plated electrode reached ≈ 5 mm, with tip velocities in line with the predictions of Chazalviel [2]. Upon current reversal, only the freshest dendrite tips dissolved, indicating lithium passivation by SEI. The counter-electrode then grew new dendrites that mirrored the first cycle. Volumetric growth rates and tip velocities in the second half-cycle exhibited a slight delay, likely due to a present Li^+ concentration gradient.

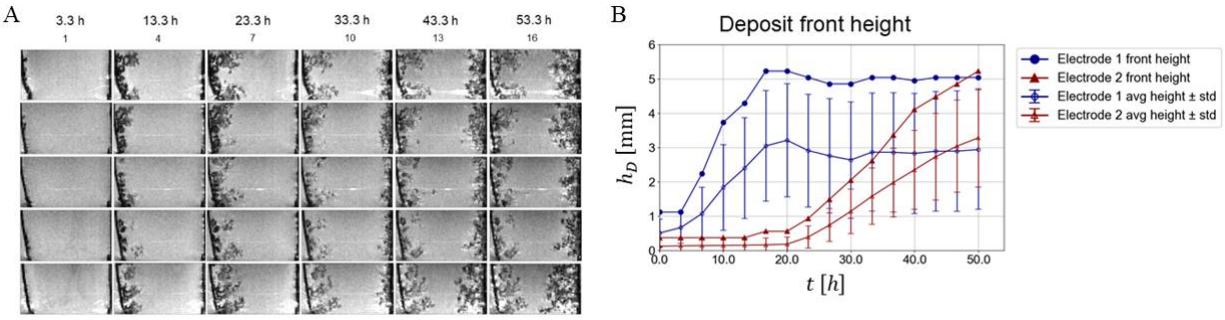

Figure 1. (A) Time-lapse of MRI slices at various depths. (B) maximum and average front height of the deposits.

Conclusion: Operando ^{1}H MRI directly shows that polarity reversal strips only the most recently deposited lithium, leaving a substantial "dead-Li" structure in place. Although tip velocities and bulk growth rates are unaffected by the reversal, the persistent scaffold poses a continuing short-circuit risk. These findings highlight both the diagnostic power of ^{1}H MRI for battery research and the limited efficacy of simple current-reversal protocols at rehabilitating lithium-metal anodes. Future work will combine simultaneous impedance spectroscopy and ^{7}Li concentration mapping to correlate the electrochemical and structural signatures of inactive lithium.

References:

[1] Ilott, Proc Natl Acad Sci U S A (2016). [2] Chazalviel, Phys Rev A, (1990).

Towards quantitative analysis of magnetic nanoparticle mixtures using COMPASS

J. Günther[1,2], *T. Kampf*[3], *M. A. Rückert*[1], *T. Reichl*[1], *N. Gehrke*[4], *V. C. Behr*[1], *P. Vogel*[1,2]
[1]Julius-Maximilians University, Würzburg, Germany, [2]Phase Vision GmbH, Rimpar, Germany,
[3]University Hospital of Würzburg, Würzburg, Germany, [4]nanoPET Pharma GmbH, Berlin, Germany

Introduction: Magnetic nanoparticles (MNP) offer great potential for biomedical applications. In particular, the possibility of functionalizing MNPs, i.e. to bind small biomolecules to their surface, makes them a versatile tool [1]. Calculating concentrations from a mixture of different MNP types is an important task since this concept can be translated to the differentiation of MNP with different mobility properties [2]. Among others, this opens possibilities to quantify the binding state of functionalized MNP with a specific biomolecule. Critical Offset Magnetic Particle Spectroscopy (COMPASS) is a suitable method for this task [3]. Here, we analyzed binary mixtures of different sized MNPs via COMPASS measurements using a system matrix approach.

Methods: COMPASS is an extension of conventional magnetic particle spectroscopy (MPS measuring the particles nonlinear magnetization response to an oscillating magnetic field while sweeping through an additional offset field. This provides additional information about MNP magnetization compared to MPS. To reconstruct the concentrations of a particle mixture the following equation must be solved:

$$Ax = b \Leftrightarrow A^{-1}\, b = x, \qquad \text{Eq. 1}$$

where A is the system matrix consisting of the COMPASS signal of 5 particle systems of different sizes (Feraspin™ S (20-30 nm), M (30-40 nm), L (40-50 nm), XL (50-60 nm), XXL (60-70 nm)), x is the concentration and b is the measured signal of the mixed sample. For this experiment, a concentration series of Feraspin™ L and a mixture series of Feraspin™ XL and Feraspin™ S were investigated. For comparison, Singular Value Decomposition (SVD) [4], Kaczmarz algorithm [5] and Non-Negative Least Squares (NNLS) method [6] have been tested.

Results and Discussion: By natively including the condition of nonnegativity of all concentration values, NNLS leads to the best results without requiring any pre knowledge about the particle sample. Figure 1a) shows the reconstruction of the concentration series of Feraspin™ L and Figure 1b) shows the reconstruction of the mixture series of Feraspin™ S and XL. The results show a high level of agreement when compared with the actual concentrations set in the samples.

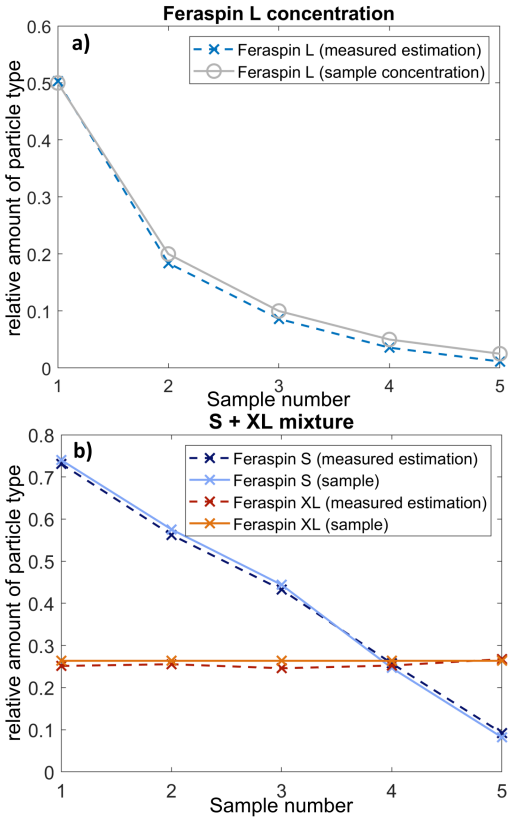

Fig. 1: a) concentration series of Feraspin™ L, reconstructed from a system matrix of five Feraspin™ systems of different size. b) mixture series of Feraspin™ XL and S

Conclusion: It was shown that COMPASS measurements and NNLS based reconstruction enable a good estimation of the concentration of binary MNP mixtures from a system matrix of five different MNP types.

References: [1] Wu, ACS Appl. Nano. Mater. (2020). [2] Viereck, J. Magn. Mater. (2019). [3] Vogel, Nat. Commun. (2022). [4] Hansen, BIT Numer. Math. (1987). [5] Hanke-Bourgeois, Linear Algebra Appl. (1990). [6] Bro, J. Chemom. (1997).

Real-time Magnetic Particle Sensing for Brain Perfusion – a simulation study

P. Vogel[1,6], T. Reichl[1], T. Kampf[1,2], M.A. Rückert[1], J. Günther[1,6], A. Wörle[1], M. Herzberg[3,4], M. Pham[2], V.C. Behr[1], S. Herz[4,5]

[1]Department of Experimental Physics 5 (Biophysics), Julius-Maximilians University Würzburg, [2]Department of Diagnostics and Interventional Neuroradiology, University Hospital Würzburg, [3]KWM Juliusspital, Würzburg, [4]Department of Diagnostics and Interventional Radiology, University Hospital Würzburg, [5]Radiologie Augsburg Friedberg, Augsburg, [6]Phase Vision GmbH, Rimpar

Introduction: Stroke is a major global health burden, affecting 15 million people annually, with 5 million deaths and 5 million cases of permanent disability [1]. As incidence rises with aging and lifestyle factors, better diagnosis and treatment are essential especially in the first hours – because **time is brain**. Recent advances in Magnetic Particle Imaging (MPI) [2] and Magnetic Particle Spectroscopy (MPS) [3] offer new opportunities for rapid stroke diagnostics [4] using magnetic nanoparticles (MNPs) to enable real-time, highly sensitive measurement of cerebral blood flow. Here, we introduce the concept of **StrokeCap**, a lightweight setup for early stroke detection.

Methods: The basic idea behind rapid stroke detection is the measurement of blood perfusion in different areas of the brain. For that, MNPs are intravenously injected in the blood flow and measured using MPS [5]: the presence of MNPs near an MPS sensor causes an unambiguous signal in form of higher harmonics due to the nonlinear magnetization response to a sinusoidal magnetic field (amplitude: ~5mT@15kHz) (**fig.1a**). Using a single-sided tx/rx system (**fig.1b**), the amount of MNPs can be tracked over time within the sensitivity area of each corresponding rx-coil. Arranging an array of MPS sensors around the head allows spatio-temporal detection of perfusion on the brain's surface (**fig.1c**). The time-dependent perfusion signals (**fig.1d**) can be visualized in different ways, e.g., as time-to-peak visualization (TTP) (**fig1.e**).

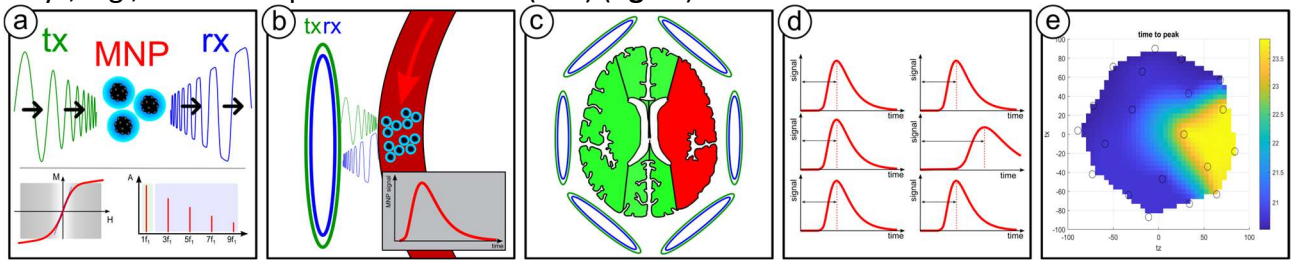

Fig. 1: (a) MPS basics: nonlinear magnetization response of MNPs to sinusoidal magnetic fields. **(b)** Single-sided MPS sensors provide spatio-temporal detection of MNPs using an array of MPS sensors **(c)**. The MPS signals of each MPS sensor **(d)** can be visualized in different ways, e.g., as time-to-peak representation **(e)**.

Results: For initial simulation studies, real CT perfusion data from stroke patients have been processed to provide 3D time-dependent perfusion information of the injected tracer. Using a home-built software [6], different tx/rx coil setups have been implemented and compared for their performance.

Discussion and Conclusion: The use of real perfusion data from CT within a home-built simulation framework requires several steps and is limited due to CT's temporal resolution, which restrains the optimization process of tx-rx systems for the StrokeCap.
However, initial simulation results allowed to design a lightweight concept for rapid and flexible deployment in emergency medical settings.

Acknowledgements: We thank Dr. Michael Angerer from Kliniken Nordoberpfalz AG Weiden for providing CT perfusion datasets for simulations.

References [1] Feigin V.L. et al., The Lancet Neurology. 20(10):795-820 (2019). [2] M. Graeser et al., Nat Commun. 10:1936 (2019). [3] P. Vogel et al., Nat Commun. 13:7230 (2022). [4] J. Guenther et al., IJMPI. 8(1):2203064 (2022). [5] S. Biederer et al., J Phys D: Appl Phys. 42:25007 (2009). [6] P. Vogel et al., IJMPI. 9(1):2303081 (2022).

Eliminating first echo transient from CPMG in inhomogeneous magnetic fields

Shin Utsuzawa[1]
[1]SLB, Sugar Land, USA

In NMR well logging, NMR signal amplitude is proportional to the formation porosity filled with ^{1}H-containing fluids, such as oil, gas, and water. This makes NMR a lithology-independent porosity tool. However, signal amplitude at t = 0 (which is proportional to porosity) cannot be measured due to ringing. Therefore, it must be inferred from an echo train measured with the CPMG sequence.

However, CPMG echoes obtained in inhomogeneous magnetic fields (which are found on NMR well logging tools and other inside-out NMR equipment) exhibits a transient [1]. In particular, the first echo is ~25 % smaller than the rest of the echoes. Therefore, it must be corrected before applying an inversion to obtain porosity. Because the size of the transient depends on signal bandwidth, which changes due to temperature and borehole/formation conductivity, this process is error prone.

Here, we propose a method to mitigate the CPMG echo transient by using two-step phase cycling. Figure 1 shows two measurements, one with the regular CPMG with the refocusing pulses phase shifted from the excitation pulse by 90 degrees, and another with a modified CPMG with the first refocusing pulse phase shifted from the rest of the refocusing pulses by 90 degrees (therefore, this first refocusing pulse is phase shifted from the excitation pulse by 0/180 degrees). The latter is like generating a CP echo and keep refocusing it with CPMG pulses. By combining these two measurements, we obtain the same amplitude and shape throughout the echo train.

However, there is one caveat; amplitude of this "combined" echo train is the same as that of the first echo, i.e., ~25 % smaller than the regular CPMG echoes. This makes it a hard choice when signal-to-noise is limited. A solution is to infer the amount of necessary correction from a short sub-measurement (Figure 2) and apply corrections to the main measurement based on regular CPMG. This will ensure robust porosity measurement with minimal increase in the total measurement time.

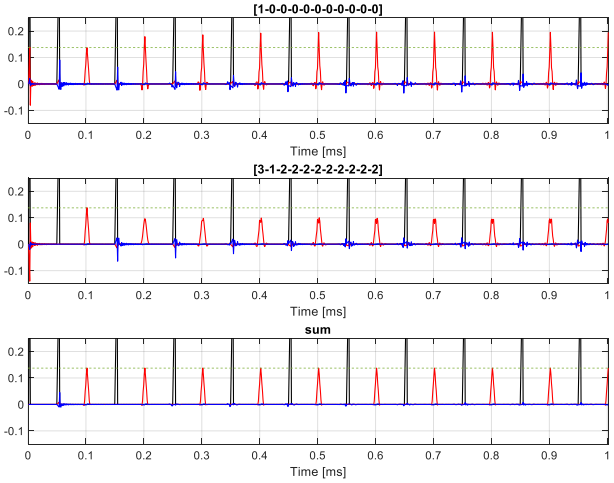

Figure 1. Two-step phase cycling to obtain an echo train with constant amplitude and shape. (top) Regular CPMG with the second and the following echoes ~25 % larger than the first echo. (middle) Modified CPMG with the second and the following echoes ~25 % smaller than the first echo. (bottom) The sum of steps 1 and 2.

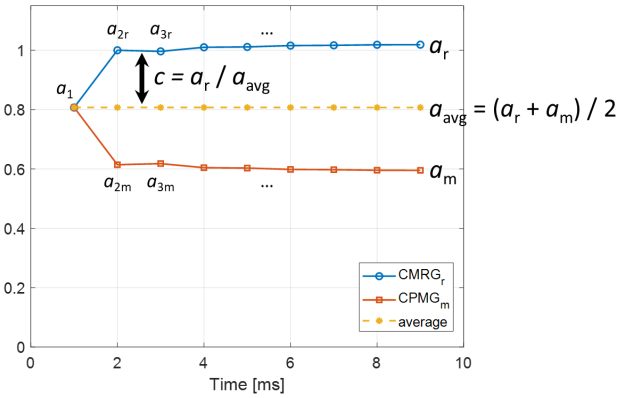

Figure 2. Correction of the first echo transient. The necessary correction factor c may be obtained as the ratio of the regular CPMG (a_r) to the average of the regular CPMG and modified CPMG (a_m).

Reference:

[1] M. D. Hürlimann and D. D. Griffin, *J. Magn. Reson.***143**,120-135 (2000).

Accelerated porous structure determination of biocompatible hydrogels by Time-Resolved Restricted Diffusion NMR method

M. Czarnota[a], *S. Domański*[b], *M. Urbańczyk*[a]
[a]Institute of Physical Chemistry Polish Academy of Sciences, Warsaw, Poland,
[b]Polbionica S.A., Warsaw, Poland

Introduction: Restricted diffusion measurements with Nuclear Magnetic Resonance spectroscopy provide useful information about porous structures. A disadvantage of this measurement is its duration, which can be shortened significantly by applying fast methods [1]. Restricted diffusion measurements utilize the behavior of molecules with movement limited by porous structures since the diffusion coefficient is lower than expected for unrestricted movement. An example of a porous structure can be a gelatin methacrylate (GelMa) hydrogel. GelMa is a biocompatible material that has plenty of applications in medicine. One of the most promising applications is as a scaffold for bionic organs such as the pancreas [2].

Methods: We use Time-Resolved Diffusion NMR to accelerate Restricted Diffusion measurements of GelMa hydrogel samples with varying GelMa concentration, its degree of substitution with methacrylic groups, and illumination time. We also used Scanning Electron Microscopy to compare the results from both methods.

Results and discussion: We obtained the diffusion coefficient of water dependence on diffusion time for GelMa hydrogel samples. The measurement time for a single sample was between 50 minutes and 3 hours, depending on the T_1 relaxation time of water in the sample. In this case, the measurement time was about 14 times shorter than the conventional one with the same resolution of diffusion time dimension. The estimated average size (diameter) of pores is in the range of 60-95 µm. The size was calculated from surface-to-volume ratio (S/V) from the short time (<100ms) dependence of diffusion coefficient (D) on diffusion time (Δ) [3]:

$$\frac{D(\Delta)}{D_0} = 1 - \frac{4}{9\sqrt{\pi}} \times \frac{S}{V} \times \sqrt{D_0 \Delta} \qquad D_0 - \text{unrestricted diffusion coefficient} \qquad \text{Eq. 1}$$

Assuming that pores are spherical, which was validated by SEM, the diameter can be calculated from S/V. From the D(Δ) dependence over the whole range of Δ [3]:

$$\frac{D(\Delta)}{D_0} = 1 - \left(1 - \frac{1}{\alpha}\right) \frac{c\sqrt{\Delta} + \left(1 - \frac{1}{\alpha}\right)\frac{\Delta}{\theta}}{\left(1 - \frac{1}{\alpha}\right) + c\sqrt{\Delta} + \left(1 - \frac{1}{\alpha}\right)\frac{\Delta}{\theta}} \qquad \theta - \text{pore scaling constant} \qquad \text{Eq. 2}$$

$$c = \frac{4}{9\sqrt{\pi}} \times \frac{S}{V} \times \sqrt{D_0}$$

the tortuosity (α) values were calculated.

Conclusion: We were able to accelerate the Restricted Diffusion measurements successfully. By using the Time-Resolved method, GelMa hydrogel's properties can be acquired much faster, about 14 times.

References: [1] Urbańczyk, Anal. Chem. (2020). [2] Klak, Micromachines (2020). [3] Latour, J. Magn. Reson. (1993)

T_1 Relaxation Time Distribution Inversion: Reinvented

Armin Afrough [1], *Thomas Vosegaard* [1]
[1] Aarhus University, Aarhus, Denmark

Introduction: Multi-exponential recovery is prevalent in T_1 relaxation processes in NMR and MRI where a signal recovers through multiple relaxation processes to an equilibrium steady-state value. In heterogeneous materials, these processes exhibit a complex behavior reflecting the eigenvalues of relaxation-diffusion and exchange processes that is better represented by a probability distribution function $f(\tau)$ of lifetimes, as

$$s(t) = \int_0^\infty f(\tau)\left(1 - \alpha\, e^{-\frac{t}{\tau}}\right) d\tau. \qquad \text{Eq. 1}$$

The goal of T_1 relaxation time distribution inversion is to compute $f(\tau)$ from signal $s(t)$.

Methods: Eq. 1 is commonly solved for $f(\tau)$ by two schemes by either (a) fitting the data to a pre-defined mathematical model with assuming a fixed value of $\alpha = 2$ or $\alpha = 1$ [1], or (b) normalizing the signal in the positive real space and employing methods designed for multi-exponential decay [2]. We recognized that these schemes are not appropriate or efficient – especially in inhomogeneous radiofrequency fields, for quadrupolar nuclei, and for samples with long T_1. We provide a robust alternative solution to finding $f(\tau)$ in multi-exponential *recovery* processes with *unknown recovery factor* α and *without extended measurement windows*. By recasting the recovery signal as a linear system,

$$s(t) = \sum_{i=0}^{N_\tau}[f_i - \alpha f_i \exp(-t/\tau_i)] = f_\infty - \sum_{i=1}^{N_\tau} f_i' \exp(-t/\tau_i), \qquad \text{Eq. 2}$$

that includes the unknown steady-state value f_∞ explicitly, and the recovery factor α implicitly, we solve for f_i' and f_∞ by employing regularization – and finally obtain the lifetime distribution f_i corresponding to τ_i.

Results and discussion: The invented method performs an excellent inversion even for non-ideal recovery factors and short measurement windows; see Fig. 1. We applied the method, and will show its results, in NMR spectroscopy of milk powders and crude oil, surface NMR of aquifers, and dynamic nuclear polarization – where it showed interesting results that would not be obtained without.

The method can detect lifetime components approximately at the same order of magnitude as the longest measurement time. The recovery factor appropriately captures instrument and sample non-idealities and folds these imperfections into a fitting parameter with physical significance.

Conclusion: The revised formulation finds $f(\tau)$ in any one- or multi-dimensional datasets with at least one recovery dimension in NMR, MRI, surface NMR, and dynamic nuclear polarization build-up curves – completely transforming how we process T_1 recovery data and distinguishing it from multi-exponential decay analysis.

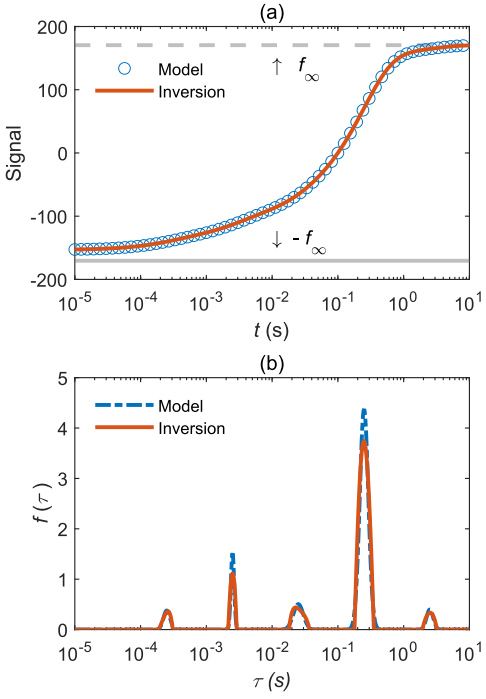

Fig. 1: Excellent agreement was found between the model and its inversion for non-ideal cases; here with recovery factor $\alpha = 1.9$ and a signal that is still rising at the longest measurement times.

References: [1] Venkataramanan, IEEE Trans. Signal Process. (2002). [2] Afrough, Phys. Rev. Applied (2021).

On the source of unresolved Nyquist ghosting in EPI at ultrahigh field

H. Scholten[1], I. Homolya[2], H. Köstler[1]

[1]Department of Diagnostic and Interventional Radiology, University Hospital Würzburg, Würzburg, Germany, [2]Chair of Molecular and Cellular Imaging, Comprehensive Heart Failure Center, University Hospital Würzburg, Würzburg, Germany

Introduction: Nyquist ghosting in echo planar imaging (EPI) arises from a misalignment of the forward and reversed k-space lines.[1] For human-sized 7T scanners, it has been reported that the standard navigator-based correction method[2] does not suppress ghosting sufficiently[3–5], because the shift between odd and even echoes varies over time.[3,5] We show that this is related to mechanical resonances of the gradient coils, and apply a trajectory correction, which improves ghost suppression.

Methods: We acquired single-shot EPI images of a spherical phantom in a coronal slice on a 7T scanner with two orthogonal phase encoding directions. We characterized the gradient system with the gradient system transfer function (GSTF)[6] and used it to calculate corrected k-space trajectories.[7] Dwell time differences between the GSTF acquisition and the k-space sampling points were compensated for.[8] From the corrected trajectories, we calculated the shifts between forward and reversed k-space lines.

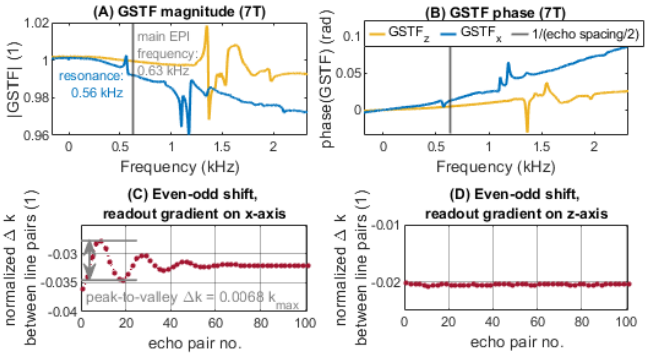

Fig. 1: (A) Magnitude and (B) phase of the GSTFs of the x- and z-axis of the 7T gradient system. (C,D) GSTF-predicted shift between center points of odd and even readouts.

Results: Fig. 1 shows that the main frequency of the oscillating EPI readout gradient, is close to a mechanical resonance of the gradient coil of the physical x-axis (A,B). The GSTF-predicted shift between odd and even readout echoes oscillates if the readout gradient is on the physical x-axis (C), but is constant with the readout gradient on the physical z-axis (D). The varying shift between echoes results in severe ghosting artifacts under the navigator-based correction (Fig. 2A,B). With the GSTF-based correction (C), both the average and maximum ghost intensity is reduced. With the readout gradient on the z-axis (Fig. 2D-F), the maximum ghost intensity is also lower with the GSTF-based reconstruction (F).

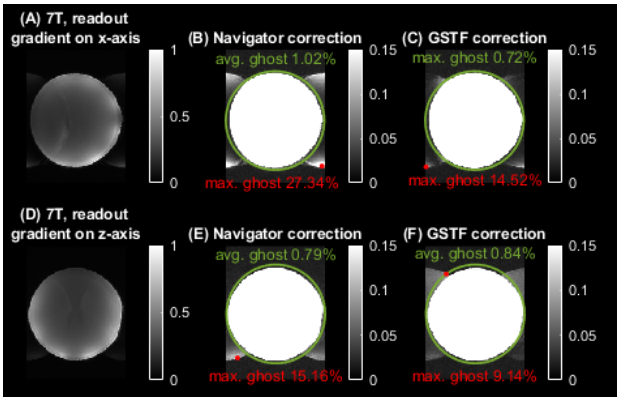

Fig. 2: Coronal phantom images. (A,B,C) Readout gradient on x-axis. (D,E,F) Readout gradient on z-axis. Average ghost intensity: outside the green circle. Red circles: maximum ghost intensities.

Discussion and Conclusion: Our GSTF-predicted trajectories replicated the oscillating k-space shifts that were previously reported for 7T systems[3,5]. We also confirmed the associated failure of the navigator-based ghost correction. We related this effect to a mechanical resonance. As shown before[7], a GSTF-based trajectory correction can reduce Nyquist ghosting, as it incorporates mechanical oscillations of the coils. Ghosting can also be reduced by shifting the axis or main frequency of the oscillating readout gradient away from any resonances. This work thus identified an additional source of residual Nyquist ghosting in EPI at ultrahigh field, and two possible alleviations.

References: [1] Bernstein, Handbook of MRI Pulse Sequences (2004). [2] Heid, US Patent (2000). [3] Poser, Proc. ISMRM (2010), [4] Josephs, Proc. ISMRM (2020), [5] Goa, Proc. ISMRM (2021), [6] Scholten, Magn. Reson. Med. (2023), [7] Vannesjo, Magn. Reson. Med. (2016), [8] Scholten, NMR Biomed (2024)

Chemically Resolved MRI with Field Inhomogeneity Correction

A. Tsanda[a,b], S. Benders[a], M. Adrian[a], A. Penn[a], T. Knopp[a,b]
[a]Hamburg University of Technology, Hamburg, Germany
[b]University Medical Center Hamburg-Eppendorf, Hamburg, Germany

Introduction: Magnetic Resonance Imaging (MRI) allows spatially resolved *in situ* identification of chemical species via their shifts from the proton resonance frequency, which is beneficial in chemical engineering. However, traditional spectroscopic methods are time-consuming at high spatial resolutions. Recent techniques adapt non-spectroscopic sequences by incorporating prior knowledge of chemical species spectra to overcome this constraint [1], but they remain sensitive to magnetic field inhomogeneities, particularly in large-bore systems. This work addresses that limitation by combining field inhomogeneity correction with chemical species reconstruction in a unified method.

Methods: We extend the forward model by Harbou *et al.* [1], which combines weighted *k*-space contributions from individual chemical species based on their spectra, introducing both amplitude scaling and phase shifts. The model represents a superposition of the Fourier transform and a chemical shift operator. Here, we further modify the Fourier operator to incorporate field inhomogeneity maps [2], enabling the model to account for spatial phase variations. Experiments were conducted on a cylindrical water phantom with an inserted tube containing acetone–water mixtures at varying ratios. Data were acquired using a multi-echo gradient echo (mGRE) sequence with 32 equidistant echoes (1.81 ms spacing, starting at 1.1 ms), yielding a 21.5 s scan time for a 16 cm × 16 cm field of view and an 80 × 80 grid.

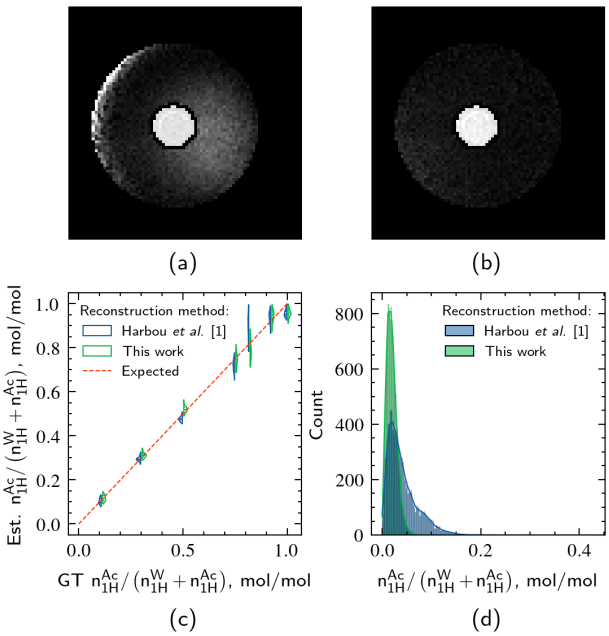

Fig. 1: Chemically resolved reconstruction in the transverse plane of a tube with an acetone–water mixture submerged in a larger tube: (a, b) acetone ratio maps with (a) and without (b) field inhomogeneity correction; (c) acetone ratio distributions in the inner tube across varying concentrations; (d) ratio distribution in the outer tube across experiments.

Results and Discussion: Fig. 1(a–b) shows reconstructions for an acetone proton molar ratio of 0.3 in the inner tube, with and without field inhomogeneity correction. Artifacts–visible as white regions in the outer tube–are removed after correction, yielding a more homogeneous appearance. Image quality in the inner tube remains unchanged. Fig. 1(c) shows acetone ratio distributions in the inner tube. The mean absolute errors (MAEs) are 0.033 ± 0.024 (with correction) and 0.026 ± 0.013 (without), with no significant difference (Wilcoxon signed-rank test: $p = 0.375$, $n = 7$). In the outer tube (Fig. 1(d)), the MAEs are 0.041 ± 0.012 and 0.020 ± 0.002, showing a significant improvement after correction ($p = 0.016$, $n = 7$, $\alpha = 0.05$).

Conclusion: This work presents a reconstruction method that simultaneously resolves chemical species and corrects field inhomogeneity artifacts in non-spectroscopic Cartesian mGRE data. It achieves ~3% precision in estimating the acetone–water ratio. Correction effects are most evident in the larger water-filled region—an important consideration, as real-world samples are often similarly sized. Future work should focus on designing experiments that better reveal the expected effects in the smaller mixed region, where differences may have been masked by its limited size.

References: [1] Harbou, J. Magn. Reson. (2015). [2] Eggers, IEEE Trans Med Imaging. (2007).

NMR Relaxometry for Molecular Structure Analysis of Stimuli-Responsive Lyogels in Varied Solvent Polarities

M. Adrian[a], K.M. Eckert[a], M.R. Serial[a], L. Rennpferdt[a], A. Tsanda[a,b], S. Benders[a], H.K Trieu[a], T. Knopp[a,b], I. Smirnova[a], A. Penn[a]

[a]Hamburg University of Technology, Hamburg, Germany

[b]University Medical Center Hamburg-Eppendorf, Hamburg, Germany

Introduction: Stimuli-responsive lyogels exhibit pronounced macroscopic changes in response to external stimuli, positioning them as promising candidates for applications such as flow control valves and catalyst carriers in SMART reactors [1]. For their effective integration in such systems, it is essential to understand their internal pore structure and diffusion behavior, as these factors directly influence functionality. While several techniques exist to quantify macroscopic swelling and shrinking, few methods provide insight into the microstructural transformations occurring during these processes.

Methods: To address this gap, we employed ^{1}H Nuclear Magnetic Resonance (NMR) relaxometry and diffusometry to study solvent dynamics within lyogels under different environmental conditions. NMR is particularly well-suited for examining molecular mobility within macro-, meso-, and nanoporous systems by detecting changes in relaxation times and self-diffusion coefficients [2, 3]. Using a Spinsolve 60 MHz benchtop NMR spectrometer (Magritek, Germany), we investigated the dynamic swelling and shrinking behavior of lyogels in solvents with differing polarity.

Results and discussion: Our measurements revealed significant variations in the relaxation time profiles depending on solvent polarity, reflecting changes in molecular mobility and pore structure during swelling and shrinking (Fig. 1). These relaxation dynamics provide valuable insights into the solvent-polymer interactions at the microstructural level, which are often inaccessible by traditional swelling ratio measurements. The data suggest that solvent polarity play a critical role in modulating the internal morphology and transport behavior of lyogels.

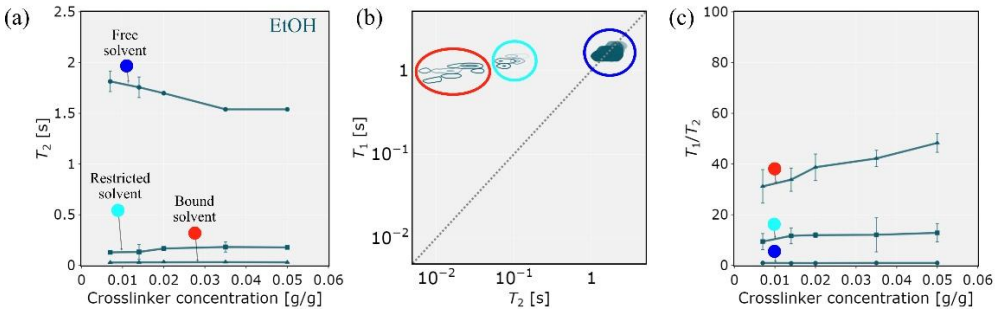

Fig. 1: (a) T_2 relaxation, (b) T_1-T_2 correlation map, (c) T_1/T_2 ratio of stimuli-responsive lyogels in ethanol (EtOH).

Conclusion: ^{1}H NMR relaxometry proves to be an effective tool for probing the microstructural evolution of stimuli-responsive lyogels. By offering detailed insights into solvent dynamics and polymer-solvent interactions, this method supports the rational design and integration of lyogels in SMART reactor technologies and other responsive material applications.

References: [1] Eckert, Fluid Phase Equilibria. (2024). [2] Giussi, Soft Matter. (2015). [3] Gruber, Polymer. (2023).

Sandstone Wettability in Supercritical CO_2-Brine-Rock Interactions Evaluated with ^{13}C and ^{1}H Magnetic Resonance/Magnetic Resonance Imaging

Ming Li [a], Pavel Kortunov [b], Alex Lee [b], Florin Marica [a], Bruce J. Balcom [a]

[a] MRI Centre, University of New Brunswick, Fredericton, Canada
[b] ExxonMobil Technology and Engineering Company, Annandale, NJ, USA

Introduction: Carbon dioxide produced anthropogenically is thought to be a major contributor to global warming. Carbon capture and storage technologies play a pivotal role because they contribute to reducing emissions from hard-to-abate industries. The effectiveness of CO_2 containment underground hinges on the assumption that the sealing formation remains water wet in the presence of dense CO_2. In this work we employed MR/MRI techniques to determine if the pore space in a Berea sandstone core plug test sample was water wet, or CO_2 wet as illustrated in Fig. 1.

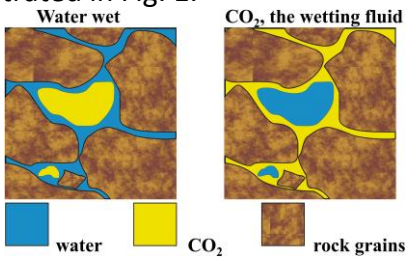

Fig.1: Pore wettability schematic: if water-wet (left), CO_2 occupies pore center; if CO_2-wet (right), water occupies pore center. Wettability describes the preference of two or more fluids to contact the pore surface. Wettability strongly affects fluid transport.

Methods: A novel variable field superconducting MR/MRI instrument was employed to undertake ^{1}H and ^{13}C measurements. The static field was switched from 0.79 T to 3.14 T as required to interrogate ^{1}H and ^{13}C at the common frequency of 33.7 MHz. A comprehensive suite of measurements was employed: ^{13}C and ^{1}H T_1, T_2, 2D T_1-T_2, 1D and/or 2D SPRITE images. Core plug saturations of brine and CO_2 were quantified from MR and MRI measurements. Measurements were undertaken at high pressure and temperature (4000 psi and 50 °C). The CO_2 phase was supercritical under these conditions. ^{13}C enriched CO_2 was employed to permit more rapid ^{13}C relaxation measurements and ^{13}C MRI measurements.

Results and discussion: Surface relaxation is well known in MR of porous media studies to be a good indicator of surface interactions and therefore wettability. T_2 is the most common parameter employed to examine surface relaxivity. In this work, the ^{13}C T_2 was not diagnostic since the high diffusivity of supercritical CO_2 resulted in a diffusion through internal magnetic field effect dominating the observed T_2. The ^{13}C T_1, particularly in T_1-T_2 relaxation correlation results showed that ^{13}C did not wet the pore surface. These results were confirmed by ^{1}H T_1-T_2 results of the brine phase. The ^{13}C enriched CO_2 phase was compressed in the core plug with a bolus of ^{12}C. ^{13}C MRI was employed to monitor mixing of the two species.

Conclusion: Supercritical ^{13}C and ^{1}H relaxation times indicate Berea sandstone remained strongly water-wet when exposed to CO_2. This multinuclear study showed the ability of MR/MRI to examine realistic processes under challenging experimental conditions.

Reference: Li, M., Kortunov, P., Lee, A., Marica, F., and Balcom, B.J. *"Sandstone Wettability in Supercritical CO_2-Brine-Rock Interactions Evaluated with ^{13}C and ^{1}H Magnetic Resonance",* Chemical Engineering Journal (2024) 500, 157100.

Monitoring Salt Precipitation in Porous Media Using ^{23}Na MRI

M.S. Zamiri[a], N. Ansaribaranghar[a], D. Green[b], B. Nicot[c], B.J. Balcom[a]
[1]UNB MRI Centre, Department of Physics, UNB, Fredericton, NB E3B 5A3, Canada
[2]Green Imaging, 520 Brookside Drive, Fredericton, New Brunswick, E3A 8V2, Canada
[3]TotalEnergies, Avenue Larribau, 64000 Pau, France

Introduction: Salt precipitation, also known as salt-out poses a challenge for CO_2 storage in saline aquifers, due to potential injectivity loss. While ^{1}H MR/MRI has been used to monitor water evaporation [1], ^{23}Na MR/MRI offers additional insight by enabling the tracking of sodium in both dissolved and crystalline forms. Furthermore, ^{23}Na MR/MRI can be combined with ^{1}H MR to give sodium concentration in the brine phase.

Methods: Experiments were conducted on Bentheimer sandstones saturated with 8 wt% NaCl brine, with dry N_2 as a model gas. Salt precipitation was monitored using a variable field magnet allowing to switch between ^{1}H and ^{23}Na MR measurements. The ^{23}Na MR signal was resolved using both T_2* and T_1 relaxation times, enabling quantitative differentiation of sodium content in solution and solid phases. Phase-encode imaging methods were employed to selectively image solution and crystalline sodium.

Results and discussion: Initially, brine was displaced due to viscous flow of gas. Fluid displacement was well separated from the subsequent evaporation and salt precipitation stages. A complete conversion of the residual solution sodium into crystalline sodium was observed. 1D and 2D images were acquired showing the spatial distribution of sodium during and after drying.

Conclusions: Crystallization was localized at the drying front near the sample inlet. This salt accumulation was attributed to capillary backflow [2] to transport sodium to the drying front, as evidenced by the contrasting spatial profiles of ^{23}Na and ^{1}H content in solution. The methods presented using ^{23}Na MRI have great potential for salt precipitation studies, paving the way for applications in CO_2 storage and other processes.

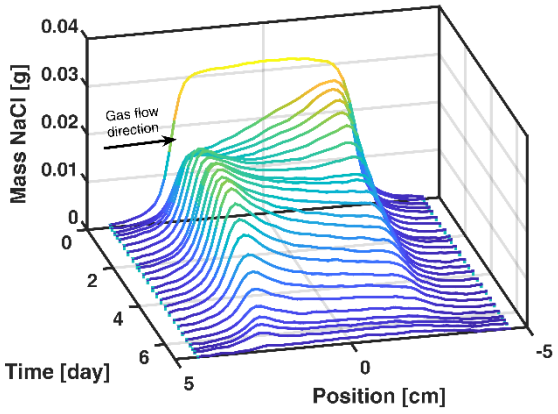

Fig. 1: 1D Hybrid-SESPI images of solution, ^{23}Na converted to NaCl mass for display.

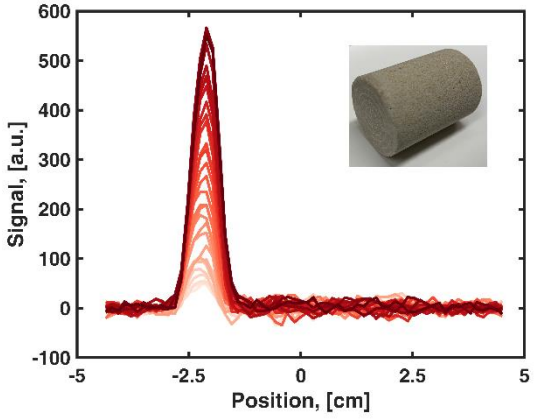

Fig.2: 1D images of crystalline sodium at various times during the process acquired using 1D DHK SPRITE. The images show progressive accumulation of salt crystals at the entrance of the core plug.

References:

[1] Y. Wang, E. Mackie, J. Rohan, T. Luce, R. Knabe, and M. Appel, SCA2009-25 (2009)
[2] H. Ott, S.M. Roels, K. de Kloe, Int. J. Greenh. Gas Con. 43, 247-255 (2015)

Use of MRI to investigate effects of SAP synthesis on swelling distribution

Hannah Tiernan, Diana Bernin**

**Chalmers University of Technology, Gothenburg*

Introduction: The feminine hygiene market encompasses a wide variety of products and is valued at US $4.72bn with a projected increase of 4.37% by 2028. [1] Efficient uptake of specific bodily fluids is integral to the function of a personal hygiene product, and the rate and effectiveness of solution uptake is determined by multiple factors; composition and synthesis of materials, degree of crosslinking of SAP (directly related to swelling capacity), and the distribution of liquid over polymer material, as examples. [2] Understanding these parameters and how they impact the materials is integral to improving their function, which could lead to a reduction in cost and an increase in accessibility. Magnetic Resonance Imaging (MRI) is useful in this study of SAP swelling, as it can accurately determine the distribution of fluid throughout the sample.

Methods: This study uses 1D Profiling and T2 and diffusion maps to investigate the behaviour and properties of SAPs. 1D Profile images are used to provide kinetic information on the initial absorption of water into SAP particles, whilst T2 and diffusion maps give an overview of the behaviour of SAP particles at equilibrium. This setup allows for non-invasive, high-resolution imaging of SAPs as they undergo deformation, absorption, and swelling.

Results and Discussion: Initial results highlight the potential for this methodology to monitor kinetics of SAP particles and surrounding solution. Fig. 1, a 1D Profile space-time plot, shows initial proton distribution throughout the sample, from which we can infer the swelling behaviour of SAP changes over time from initial solution addition.

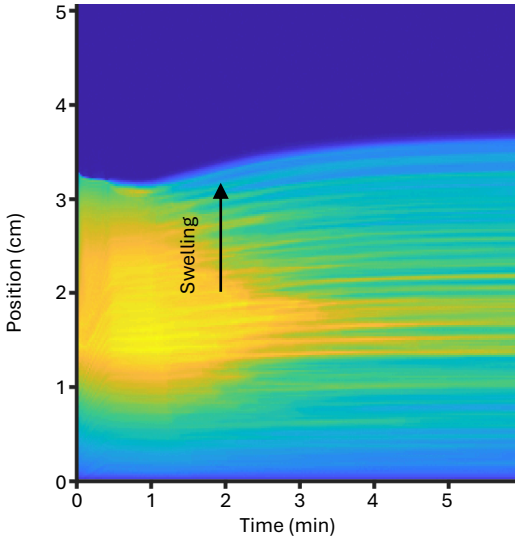

Fig. 1: The swelling process of SAP was monitored using the 1D profiling method. Stacked 1D T2-weighted profiles recorded in a slice as a function of time. Yellow = high intensity, blue = low intensity.

Conclusion and Outlook: These results will offer insight into water distribution and swelling behaviour throughout the polymer matrix. Multiple commercial SAPs produced under varying synthesis conditions will be used for testing. Using this technique and multiple scan protocols, we aim to deepen the understanding of SAP behaviour and optimize their application in real-world scenarios.

References:

1. Statista. Feminine Hygiene - United States 2024 [Available from: https:// www.statista.com/outlook/cmo/tissue-hygiene-paper/feminine-hygiene/united-states.
2. Damiri F, Salave S, Vitore J, Bachra Y, Jadhav R, Kommineni N, et al. Properties and valuable applications of superabsorbent polymers: a comprehensive review. Polymer Bulletin. 2023.

Monitoring magnesia cemented paste backfill using low field ^{1}H NMR relaxometry

C. I. Karunarathne[1], N. Ling[1], A. Fourie[2], M. L. Johns[1], E. O. Fridjonsson[1]

[1]School of Engineering, Department of Chemical Engineering, The University of Western Australia, Crawley, Australia, [2] School of Engineering, Department of Civil, Environmental and Mining Engineering, The University of Western Australia, Crawley, Australia

Abstract

When the mining industry extracts minerals vast volumes of waste material known as tailings are generated, with tailings-to-product volume ratio of 100:1 common and in extreme cases 1,000,000:1 [1]. For safe deposition of solids into underground mine openings cemented paste backfill (CPB) is often used. CPB is a heterogeneous material formulated using mine tailings (typically 70-85 wt% of total solids content), binder (up to 10 wt% of total solids content) and water. In this study, we utilise low-field ^{1}H nuclear magnetic resonance (NMR) relaxometry (T_2) to monitor the curing of magnesia CPB [2] over 28 days. Magnesia cements are of interest due to their rapid strengthening coupled with the capacity for CO_2 capture. Here we study the effect of magnesium oxychloride (MOC), or Sorel cement, formed by the combination of $MgCl_2$ and MgO. The results (see Fig 1) show $T_{2,mean}$ relaxation time of magnesia CPB samples compared with CPB samples prepared using ordinary Portland cement (OPC). The $T_{2,mean}$ evolution over time was compared with mechanical strength using uniaxial compressive strength (UCS) testing, and product formation was assessed using scanning electron microscopy (SEM). The results of the study showed that magnesia CPB exhibits T_2 relaxation evolution consistent with the more rapid curing of MOC. Furthermore, the relative importance of magnesia concentration and solution pH on the formation mechanism of MOC [3] was experimentally evidenced by the change in $T_{2,mean}$ when magnesia CPB was prepared using either 0.5 M or 3M $MgCl_2$.

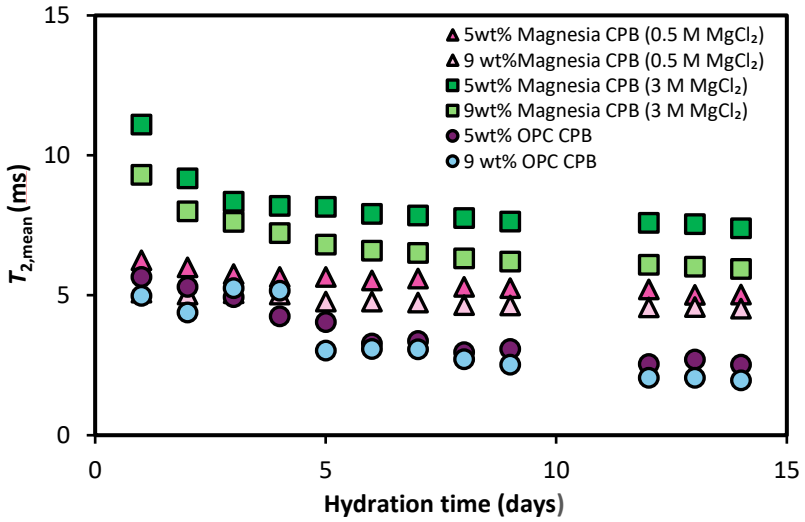

Fig. 1: Comparison of the measured $T_{2,\,mean}$ obtained from the modal peak as a function of hydration time for magnesia CPB samples prepared with 0.5 or 3 M $MgCl_2$, and Ordinary Portland CPB samples. Samples were prepared using either 5wt% or 9wt% binder.

References:

[1] Dudeney et al., Int. J. Min. Reclam. Environ. (2013). [2] Walling and Provis, Chem. Rev. (2016), [3] Deng and Zhang, Cem. Concr. (1999).

A Sequential Methodology for Characterizing short-relaxation Solid Porous Media

Zhenshuo Ma[a], Yan Zhang[b], Lizhi Xiao[c]
[1] National Key Laboratory of Petroleum Resources and Engineering, Beijing, China,
[2] China University of Petroleum, Beijing, China

While nuclear magnetic resonance (NMR) enables fluid characterization in short-relaxation porous media (e.g., shale), it remains limited in detecting ultra-short-relaxation solids such as kerogen. To address this, we developed an innovative pulse sequence (Figure 1) that combine magic sandwich echo (MSE) relaxation detection with ultra-short relaxation imaging. The K-space data acquisition in the sequential Imaging module was partitioned into central and peripheral regions. The outer high-frequency spatial data were acquired using radial sampling, while the central region data were collected through Cartesian trajectory acquisition. T_1-T_2 relaxation spectra can be obtained by spatially resolved experiments, the signal can be expressed as:

$$S(r,t,T_W) = S(0)\iint f(T_1,T_2)(1-2\exp(-\frac{T_W}{T_1}))\exp(-\frac{t}{T_2}) \times \rho(r)\exp(-kr)drdT_1dT_2 \quad \text{Eq. 1}$$

where, $f(T_1, T_2)$ is the kernel function, r is the spatial position, T_W is the recovery time, t is the echo time, $S(r, t, T_W)$ is the signal. The 3D imaging of the dry shale sample in Pengshui block (Figure 2), which reveals macroscopic pore architecture with the color-coded represents signal intensity. Figure 3 shows the global T_1-T_2 spectrum, which provides microscopic-scale insights into the compositional heterogeneity of the sample. Comparative analysis with IR-CPMG-derived spectra confirms superior solid-phase signal can be acquired by our method. Furthermore, regional division of the imaging data enables extraction of localized relaxation spectra from specific areas of interest, thereby facilitating precise evaluation of pore structure heterogeneity within shale formations. This study offers a trustworthy experimental technique to benefit short-relaxation solid porous media exploration on the core scale.

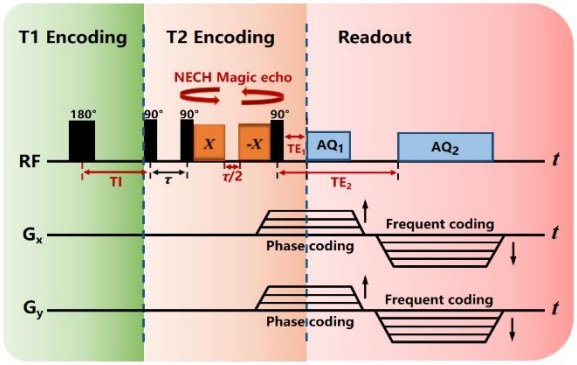

Fig. 1: IR-Magic-PETRA pulse sequence.

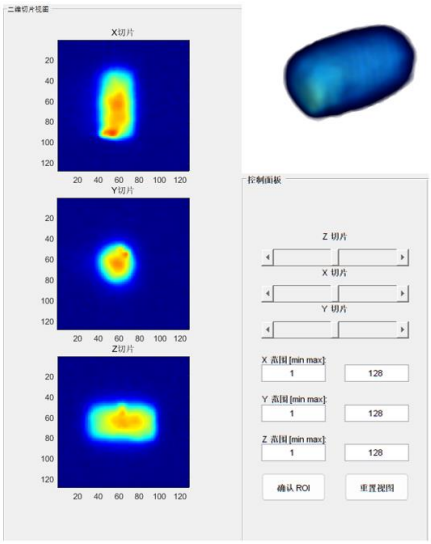

Fig. 2: The 3D imaging of shale in Pengshui block with homemade UI interface for regional division.

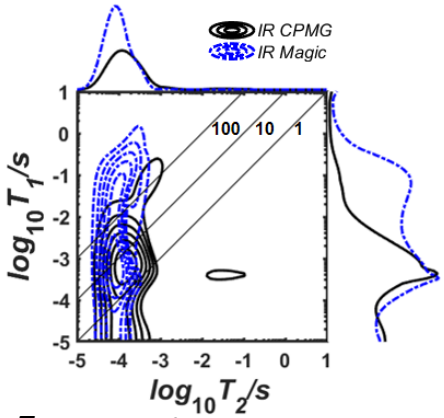

Fig. 3: The T_1-T_2 spectrum of shale in Pengshui block.

References:
[1] Zijian Jia, Energy&Fuels. (2017).
[2] Grodzki, Mag. Res. Med. (2012).
[3] Zhenshuo Ma, Energy&Fuels. (2025).